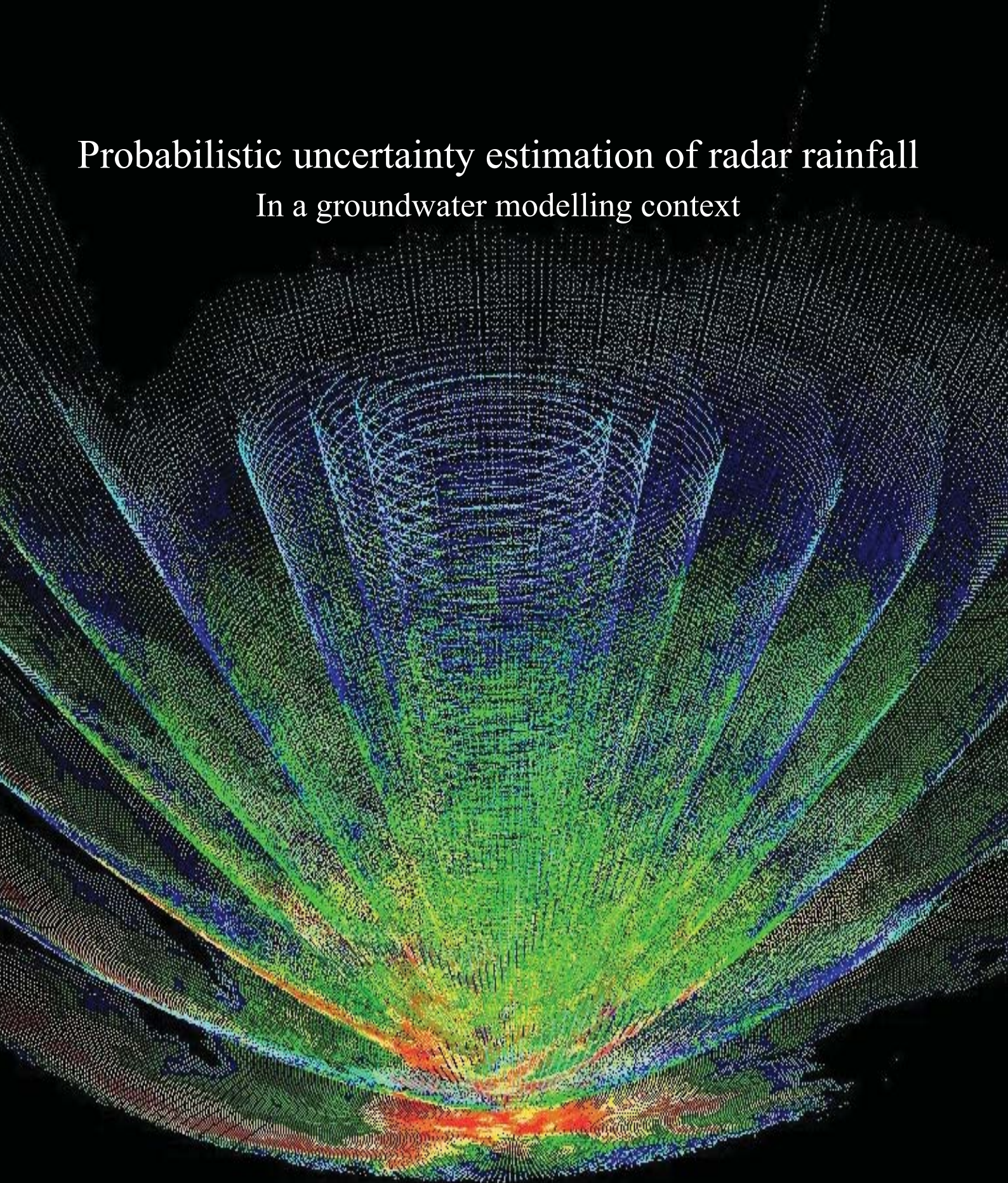


# Probabilistic uncertainty estimation of radar rainfall

## In a groundwater modelling context



Long Master Thesis  
David G. Jensen  
Aalborg University, 2012



**Aalborg University**  
**The Faculty of Engineering and Science**  
**School of Engineering and Science**  
Sohngaardsholmsvej 57  
DK-9000 Aalborg  
Phone number +45 9940 8530  
<http://www.bsn.aau.dk>

**Title:** Probabilistic uncertainty estimation of  
radar rainfall  
- In a groundwater modelling context

**Project period:** Long Master Thesis 9<sup>th</sup> and 10<sup>th</sup>  
semester

**Author:**

---

Jensen, David Getreuer

**Supervisors:**

Rasmussen, Michael R.  
Thorndahl, Søren  
Lockington, David

**Copies: 4**

**Pages: 119**

**Ended on: 08-06-2012**

**Synopsis:**

The field site for this study is Bribie Island north east of Brisbane, Queensland, Australia. The data from Mt. Stapylton radar located south of Bribie Island is used. The uncertainty of Mt. Stapylton's radar quantitative precipitation estimation (QPE) is estimated through a probabilistic approach. The deterministic radar precipitation field are perturbed to produce ensembles from which the variability of the ensembles represents the uncertainty of the radars QPE. The ensembles are generated from the spatial and temporal error structure estimated from rain gauges as ground reference. The algorithm is found capable of removing bias and producing applicable time series for hydrological modelling.

The aim of the project is to investigate the sensitivity of groundwater models to the uncertainty in the radar QPE input. Therefore a groundwater model of Bribie Island have been built. The model is set up in Mike SHE and is a transient model that in cooperates an evapotranspiration model, unsaturated zone model and saturated zone model. The model has been calibrated to fit average observed groundwater levels.

By translating the uncertainties via the variability in the produced ensembles through the groundwater model it is found that the simulated groundwater levels have a modest variability. The amount of work needed to set up the ensemble generator is not in proportion with the variability in the output from the groundwater model.



# Preface

This study is written as a master thesis for the 3<sup>th</sup> and 4<sup>th</sup> semester of the Master of Science in Water and Environment, School of Engineering and Science at Aalborg University. It has been devised in the period from the 1<sup>st</sup> September 2011 to the 7<sup>th</sup> June 2012.

From 1<sup>st</sup> September 2011 to 20<sup>th</sup> January 2012 the working location was Australia at The University of Queensland, School of Civil Engineering under supervision of Professor David Lockington. The project location is Bribie Island north east of Brisbane, Queensland, Australia.

The data from the Mt. Stapylton radar, was purchased from the Bureau of Meteorology (BoM) and kindly paid for by Prof. David Lockington from The University of Queensland. Furthermore Prof. David Lockington also kindly financed the purchase of 16 rain gauges for a field experiment investigating the spatial distribution of precipitation in small scale. The experiment have not been included in the current study but the data will be processed subsequently.

I would also like to thank Kasper Østergaard for helping me with all the practicalities regarding the stay at The University of Queensland and for the many field trips from which I have learned alot.

Another thanks goes to honours student, Joshua Soderholm aswell from The University of Queensland, for helping me getting the contact to BoM and providing access to BoM's conversion tool.

I would also like to thank Jesper Ellerbæk Nielsen for the good talks and his willingness to assist.

Aalborg, 7<sup>th</sup> June 2012



# Danish summary

Emnet for dette projekt er usikkerheds estimerer på radar bestemmelse af nedbør. Der tages udgangspunkt i Bribie Island der ligger nordøst for Brisbane, Queensland, Australien. Radaren der benyttes i denne sammenhæng er Mt. Stapyhton radaren der er lokaliseret syd for Bribie Island.

I Queensland, Australien er det hovedsageligt overflade vand der benyttes til drikkevand. Fra 1997 til 2009 oplevede Queensland århundrets tørkeperiode der medførte at drikkevands reservoirerne faldt til et kritisk lavt niveau. I sommeren 2010/11 fyldt en række kraftige regnhændelser drikkevands reservoirerne igen, men medførte også kraftige oversvømmelser. I frygt for fremtidige oversvømmelser holdes vand niveauet i drikkevands reservoirerne nu nede og ved udsigt til kraftig regn lukkes der vand ud så der er en større buffer kapacitet i systemet. Området omkring Brisbane er derfor mere sårbar overfor tørke perioder end tidligere pga den mindre tilbageholdelse af drikkevand. Dette har affødt en diskussion om hvorvidt grundvand skal udnyttes i højere grad end det bliver idag. Bribie Island er en af de få steder i Queensland hvor grundvandet bliver udnyttet til drikkevand og der er i den forbindelse blevet udviklet flere grundvandsmodeller. I grundvandsmodellering er regnindputtet vigtigt og i et land som Australien hvor det praktisk ikke er muligt at have regnmålere i tilstrækkelig udstrækning kan nedbørsestimerer med radar benyttes pga. dens store rækkevide. Det er i den sammenhæng vigtigt at bestemme usikkerhederne på radar nedbørs estimatet og undersøge hvor sensitiv en opbygget grundvandsmodel af Bribie Island er overfor usikkerhederne i radar regnindputtet.

Baggrunden for usikkerhederne relateret til nedbørs estimerer fra radaren er kategorisk beskrevet opdelt i afsendelse af radar bølge, refleksivitet og behandling af data. Det vurderes at de vigtigste usikkerheder som er sværest at håndtere er dæmpning af radar bølgen, ændringer i det vertikale refleksivitets profil og ændringerne i regndråbestørrelsen. Yderligere er usikkerheder relateret til måling af nedbør med regnmåler beskrevet, hvor den største usikkerhed er vinden der mindsker det effektive areal af regnmåleren der derfor kan underestimere. Yderligere er det diskuteret hvordan en regnmåler og radar estimat kan sammenlignes både i forhold til den spatial fordeling og tidlige opløsning.

En probabilistisk ensemble generator udvikles til at kunne beskrive usikkerhederne for Mt. Stapyhton radaren i et område over Bribie Island. Udfra den spatiale fejlstruktur, i sammenligning med regnmålere, og den temporale fejlkorrelation genereres en række perturbationer til at perturbere det deterministisk nedbørsestimat fra radaren. Denne operation giver tilsvarende antal ensemble, eller realisationer af virkeligheden, som benyttes til at skabe probabilistiske tidsserier af nedbøren over Bribie Island. Der findes at indbygget i denne algoritme også ligger en inddirkete bias correction. Disse probabilistiske tidsserier hvis variabilitet indeholder usikkerheds estimatet på den radar estimerede nedbør bliver herefter benyttet som regnindput i en grundvandsmodel af Bribie Island.

En grundvandsmodel af Bribie Island opbygges i Mike SHE som en transient model der består af en evapotranspirations model, en umættetzone model og en mættetzone model. Der bestemmes et parameter sæt udfra kalibrering til gennemsnitlige målte grundvandsniveauer. Disse fastholdes i den fremadrettede analyse.

Som et sidste step foretages stochastisk simulering med de probabilistiske tidsserier produceret med ensemble generatoren. Udfra en analyse af grundvandsniveauerne bestemmes at variabiliteten af indputtet (probabilistiske tidsserier) er væsentligt større end outputtet (grundvandsniveauerne). Dette

---

leder til konklusionen at det arbejde der ligger i at generere de probabilistiske tidsserier ikke ligger til måls med de resultater der forekommer. Dette tilskrives at grundvandsmodellen er et "dæmpet" system (lang respons tid) der ikke er sensitiv overfor de små variationer i regnen men mere de akkumulerede mængder. I forhold til andre modelområder, såsom urban drainage, er dette dog ikke tilfældet og her ville variabilitet af outputtet være større end ved grundvandsmodellerne. Yderligere kan den probabilistiske usikkerhedsestimering af radar nedbørsestimatet benyttes i andre sammenhænge såsom realtid usikkerheds estimering og nowcasting.

# Table of contents

<b>1</b>	<b>Introduction</b>	<b>13</b>
1.1	Research questions . . . . .	14
1.2	Field site . . . . .	14
1.3	Mt. Stapylton radar . . . . .	16
<b>I</b>	<b>Uncertainties related to measuring precipitation</b>	<b>19</b>
<b>2</b>	<b>Uncertainties related to precipitation estimation</b>	<b>21</b>
2.1	Uncertainties related to radar QPE . . . . .	21
2.2	Radar vs. radar . . . . .	30
2.3	Rain gauge uncertainties . . . . .	32
2.4	Representativeness error . . . . .	34
2.5	Residual error discussion . . . . .	35
<b>II</b>	<b>Probabilistic uncertainty estimation</b>	<b>37</b>
<b>3</b>	<b>Methodology of ensemble generator</b>	<b>39</b>
3.1	Ensemble generator methodology . . . . .	40
<b>4</b>	<b>Practical implementation of ensemble generator</b>	<b>44</b>
4.1	Conversion of radar data from polar to cartesian . . . . .	44
4.2	Computation of residuals between radar and rain gauge . . . . .	50
4.3	Ensemble generator . . . . .	53
<b>5</b>	<b>Testing and results of ensemble generator</b>	<b>60</b>
5.1	Testing the ensemble generator . . . . .	60
5.2	Examples of ensemble members and time series produced by ensemble generator . . . . .	63
<b>III</b>	<b>Groundwater model of Bribie Island</b>	<b>69</b>
<b>6</b>	<b>Groundwater model of Bribie Island</b>	<b>71</b>

6.1	Past model development . . . . .	71
6.2	Conceptual model . . . . .	72
6.3	Numerical groundwater model . . . . .	78
6.4	Validation . . . . .	83
6.5	Discussion - Difficulties making a groundwater model of Bribie Island . . . . .	86
<b>IV</b>	<b>Ensembles as rain input in groundwater model</b>	<b>87</b>
<b>7</b>	<b>Analysis of groundwater model results</b>	<b>89</b>
<b>8</b>	<b>Discussion</b>	<b>93</b>
<b>9</b>	<b>Conclusion</b>	<b>96</b>
<b>V</b>	<b>Appendix</b>	<b>103</b>
<b>A</b>	<b>Background information of meteorological radar use</b>	<b>105</b>
A.1	How a radar sends and receives signals . . . . .	105
A.2	The radar equation in relation to meteorological radar use . . . . .	107
<b>B</b>	<b>Overall flow diagram of radar data</b>	<b>111</b>
<b>C</b>	<b>Flow diagram from polar to cartesian</b>	<b>112</b>
<b>D</b>	<b>Processing rain gauge data</b>	<b>113</b>
<b>E</b>	<b>Flow diagram of residuals between radar and rain gauge</b>	<b>115</b>
<b>F</b>	<b>Flow diagrams of ensemble generator</b>	<b>116</b>
<b>G</b>	<b>Batch script for Mike SHE groundwater model</b>	<b>119</b>

*"As far as the laws of mathematics refer to reality, they are not certain, and as far as they are certain, they do not refer to reality."*

- Albert Einstein



# Introduction 1

Through the last four decades groundwater models have been used to examine water resources, abstraction strategies, spreading of contaminants, and environmental impact assessments. The first models were built in the mid-1970 with limited applications. With increasing computational capabilities the models became more and more comprehensive and with increasing precision [van der Heijde et al., 1988]. Today the groundwater models are fully hydrological modelling frameworks that incorporate all the process in the water cycle and can be used for many purposes as well as predictive purposes. But with the increased complexity of the models it also leads to increased sources of uncertainties.

With future climate changes and as a consequence hereof increased precipitation, increased temperatures, more evaporation, and more extreme weather events in form of heavy precipitation and droughts the need for better and more precise models have never been greater [Pachauri and Reisinger, 2007]. Therefore there is a general need for solving the challenges related to handling the uncertainties of groundwater models.

The uncertainties related to groundwater modelling can be divided into four categories; Process uncertainty, structural uncertainty, parameter uncertainty, and input uncertainties [Jensen, 2009].

- Process uncertainties relates to how the numerical model is set up; boundary conditions, unsaturated zone flow, drain flow, fracture flow, stationary or transient flow, and groundwater-river interactions.
- The structural uncertainties are related to how the conceptual model is perceived; geological layers and lenses, precipitation zones, drainage zones, zones of hydraulic conductivity, and location of boundary conditions.
- The parameter uncertainties includes the geological layers horizontal and vertical hydraulic conductivities, specific yield, effective porosity, and storage coefficients.
- The input uncertainties are related to the model input and are evapotranspiration and precipitation.

The climate changes affects in particularly two parameters; evaporation and precipitation. For this reason it makes these parameters extra important to accurately measure. In the present study the uncertainties related to accurately measuring the precipitation are examined. This means that this study has focus on addressing some of the structural uncertainties and input uncertainties in relation to groundwater modelling.

Precipitation is obviously of importance in groundwater modelling [Einfalt et al., 2000] and self-evident also accurately measuring of the precipitation. In a large continent as for example Australia it is not realistic to have enough rain gauges to cover all areas and therefore for modelling purposes in areas with sparse information other types of rainfall measurements are needed. The meteorological use of radars have recently become more and more popular because of the radars long range and high spatial and temporal resolution compared to point measurements by rain gauges. The long range gives the possibility to measure precipitation in remote areas with little rain fall information and the high spatial and temporal resolution gives a much more complex picture of the precipitation field. There are therefore advantages using the radar for hydrological modelling compared to rain gauges. Despite this rain gauges are most commonly used since it is easy to set up and there are many sources of uncertainties related to the quantitative precipitation estimation (QPE) by the radar. In order to use the radar forward in groundwater modelling and utilize the radars strengths (high

spatial resolution) it is crucial to handle the uncertainties related to the QPE. Therefore this is the problem area of this study.

The many sources of uncertainties are related to the way the radar measures the precipitation. The measurement of precipitation is based on how much energy is reflected from the emitted beam when it hits the rain. The reflected energy is then interpreted into precipitation intensity. This is an indirect way of measuring the precipitation. Many researchers have worked with improving the precision of the radars ability to measure precipitation and minimising the uncertainties; uncertainties could be beam shielding and the vertical profile of reflectivity [Pellarin et al., 2001] [Bellon et al., 2006], attenuation of the radar beam [Germann, 1999] [Delrieu et al., 1999], variability in rain drop size distribution [Marshall and Palmer, 1948] [Lee and Zawadzki, 2004a], wind drift errors [Mittermaier et al., 2006], and remapping from polar to cartesian grid [Zhang et al., 2004] [Wesson and Pegram, 2004] to mention some. The normal procedure to estimate the performance of the radar is to compare it with rain gauges which are then perceived as ground truth. Rain gauges are not perfect and uncertainties are related to their observations as well. Of uncertainties could be mentioned precipitation start time uncertainties, wind drift uncertainties [Vejen et al., 1998], and intensity driven uncertainties [Habib et al., 2001].

There are basically two ways of handling the uncertainties related to radar QPE; deterministic and probabilistic. Those previously mentioned who have worked with the radar QPE uncertainties have tried handling them deterministic. This can be very difficult because of the ever changing conditions and not one optimal set of coefficients can be found to correctly adjust the reflected energy into precipitation in all situations. The other way to handle the uncertainties is a probabilistic approach. This means adapting the idea that it is not possible to determine all the uncertainties and correctly adjust the radar QPE. Instead generating multiple realisations (ensembles) based on a known space error and time error structure each ensemble member is a possible realisation of the true unknown precipitation estimates. These realisations can be directly feed into a hydrological model that yields a distribution of response values, the spread of which represents the output sensitivity to uncertainties in the input radar QPE. [Germann et al., 2009].

Based on the above-mentioned it can be argued that there is a potential using radars QPE as input for groundwater modelling, but there still is a need to handle the uncertainties. This is the basis of the outlined research questions.

## 1.1 Research questions

In areas with no or sparse precipitation information can the radar with its long range be used for measuring precipitation. Before this is applicable in groundwater modelling the uncertainties needs to be accounted for. Therefore is the objective of this study to answer the following questions:

- How can the uncertainties of radar QPE be handled probabilistic?
- Can radar QPE with advantage be used in groundwater modelling?
- How sensitive is the groundwater level to the uncertainties in radar QPE?

To carry out this investigation both a field site and radar are needed. In the following two sections the field site and the radar used in this study are described.

## 1.2 Field site

One of the regions that have experienced the extreme of variations in the climate, inflicted by climate changes, first hand is the area of Brisbane, Australia; Between 1997 and 2009 south-eastern

Australia experienced the millennium drought with the most persistent precipitation deficit in 100 years [SEACI, 2011]. Water resources became sparse and the dam levels critical low. In the summer of 2010/11 a series of events with heavy rainfall filled up the dams but also caused severe flooding throughout Queensland. The total precipitation in December 2010 was recorded to 760 mm which is 150% above the 20th century average and is the highest ever recorded by a considerable margin [SEACI, 2011] [BoM, 2012a]. Large areas of Brisbane was under water with peak water levels in Brisbane CBD of 4.46 m. 35 people was killed and an estimate of the damage is 10 billion AUD [SEACI, 2011].

The now filled up dams are used as reservoirs for drinking water which provides the area of Brisbane. The water level of the dams is kept as high as possible to have a buffer for long lasting draughts and to avoid being in the same critical situation as 2009. On the other hand the dams are controlled to let water pass whenever warnings of heavy precipitation are given so flooding, like the one in December 2010, can be avoided. The problem arises when too much precipitation have been forecasted and the dams needs to be lowered. This gives a higher buffer capacity of the system but also reduces the amount of available drinking water. This therefore makes the Brisbane area more exposed to draughts. For these reasons a discussion whether or not to utilise the groundwater resources for drink water purposes have arised. If groundwater could be utilised to provide drinking water the water levels in the dams could be minimised. Bribie Island, located approximately 65 km north-east of Brisbane see figure 1.1, is one of the few places in Queensland, Australia that already utilises groundwater resources for drinking water purposes. The groundwater provides drinking water for approximately 12000 people during the winter months and up to 40000 people during the summer months. Only very few unavailable rain gauges are situated on Bribie Island which therefore makes the use of radar QPE necessary. For these reasons Bribie Island have been chosen as the field site for the current study.



*Figure 1.1: The location of Bribie Island and Brisbane.*

Bribie Island lies parallel to the coastline of southern Queensland only separated by a narrow tidal estuary, Pumicestone Passage. The area of Bribie Island is approximately 150 km<sup>2</sup> with a length of 30 km and a width of 5 - 7.5 km. Bribie Island is a sand barrier island with a maximum elevation of approximately 14 m Australian Height Datum (AHD).

### 1.3 Mt. Stapylton radar

The radar covering Bribie Island and the surroundings of Brisbane is located at Mt. Stapylton south-east of Brisbane see figure 1.2. The Mt. Stapylton radar is a Meteor 1500 S-band Doppler radar with a range of approximately 150 km which is more than sufficient to cover Bribie Island that is located under 100 km north from Mt. Stapylton. The radar was operational from mid-2006 and built by the Federal Government's commitment to replace older, less powerful radar systems throughout Australia [BoM, 2012b].

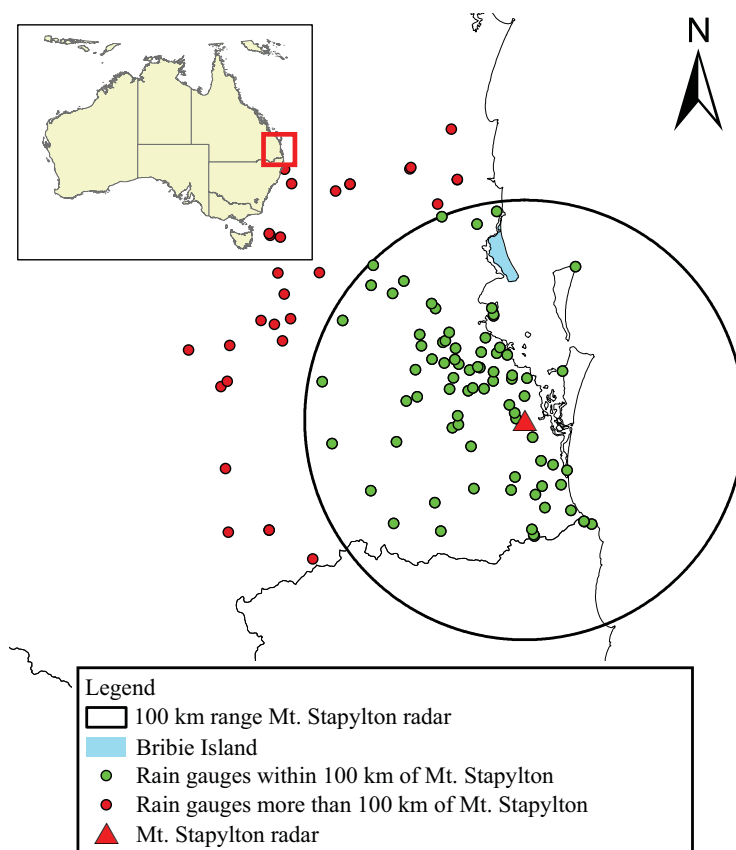


Figure 1.2: The location of Mt. Stapylton radar.

Mt. Stapylton is an isolated hill with a height of approximately 150 m AHD. The site is optimal for both doppler observations and rainfall observations within the greater Brisbane area [BoM, 2012b]. In figure 1.3 a picture of the radar can be seen.



*Figure 1.3: Picture of the Mt. Stapylton radar [BoM, 2006].*

Appendix A consists of a description of how the radar sends and receives signals. As mentioned previously measuring precipitation using radars are not without uncertainties and to be able to handle these uncertainties knowledge are needed. Therefore in the following part the uncertainties are described in more detail.



**PART**  
**I**  
**UNCERTAINTIES RELATED TO MEASURING**  
**PRECIPITATION**



# Uncertainties related to <sup>2</sup>precipitation estimation

In the introduction it was mentioned that there are many sources of uncertainties related to correctly measuring precipitation by radars and rain gauges. Before it is possible to make a probabilistic uncertainty estimation of the radar QPE, the individual uncertainties needs to be addressed of both radar and rain gauge.

## 2.1 Uncertainties related to radar QPE

In the following the main uncertainties of radar QPE are described. The uncertainties have been divided into three categories to give a better overview. In table 2.1 can the categorisation of the uncertainties be seen.

Emitting radar signal	<ul style="list-style-type: none"><li>- Orientation of radar</li><li>- Timing of radar</li><li>- Beam propagation</li><li>- Overshooting</li></ul>
Reflectivity	<ul style="list-style-type: none"><li>- Beam shielding</li><li>- Non-meteorological targets and clutter</li><li>- Attenuation of radar beam</li><li>- Vertical profile of reflectivity</li><li>- Variability in rain drop size distribution</li><li>- Wind drift errors</li><li>- Interference</li></ul>
Processing of reflectivity data	<ul style="list-style-type: none"><li>- Remapping from polar to cartesian coordinate system</li><li>- Projection of rain gauge locations</li></ul>

*Table 2.1: Grouping of uncertainties related to radar QPE.*

In figure 2.1 a graphical presentation of the uncertainties can be seen.

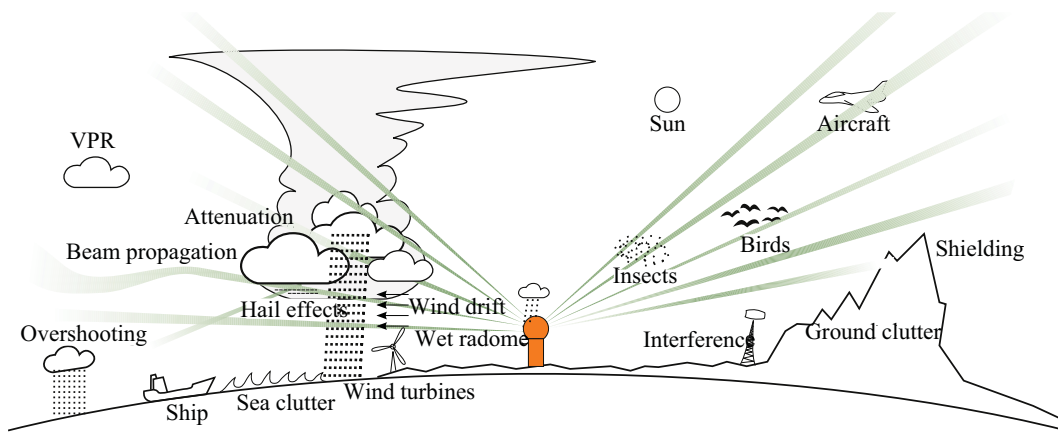


**Figure 2.1:** Graphical presentation of the uncertainties related to QPE [Peura et al., 2006, modified].

In the following a short presentation of each of the listed uncertainties are described. This is done to give the reader a understanding of the nature of uncertainties. For background information on how a radar works in general and how reflectivity is normally converted into precipitation intensities can be found in appendix A.

### 2.1.1 Orientation of radar

The orientation of the radar is very important for correctly projecting the measurements onto the earth's surface. By orientation means the radars orientation to the north see figure 2.2. If the radar is off by  $1^\circ$  it induces a displacement of 1.3 km in the x-direction in a range of 75 km.

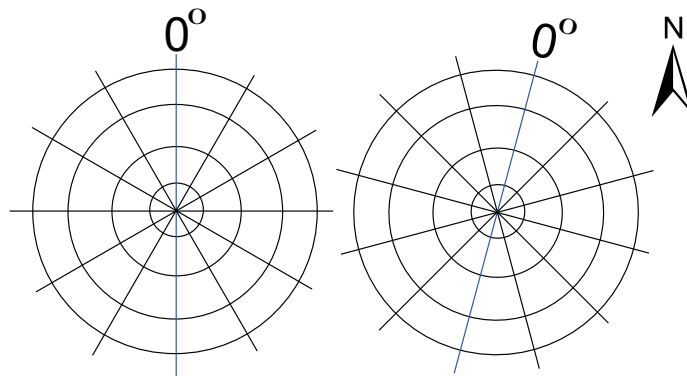


**Figure 2.2:** Example of the radars orientation in a polar coordinate system. To the left orientation is straight north and to the right it is off.

One way to investigate if the orientation is off is to compare the ground clutter map of the radar with the physical location of the static obstacles that induces the ground clutter. If the ground clutter is displaced either clockwise or counter clockwise from the physical projection of the obstacle it indicates that the orientation could be wrong. Other factors that can influence on this are e.g. the remapping method from polar to cartesian coordinate system. Another way to orient the radar is according to the sun. The position of the sun can be calculated very precise and the solar interference can then be used to orient the radar (both vertically and horizontal for volumetric radars) [Holleman and Beekhuis, 2004].

### 2.1.2 Timing of radar

The timing of the radar is important when predicting the distances to the radar echo. The emitted beam of the radar is an electromagnetic wave which propagates at the speed of light. So the distance from the radar echo can easily be calculated as the speed of light multiplied with the travel time divided by two (to and from the radar echo) see equation 2.1.

$$R = \frac{c \Delta t}{2} \quad (2.1)$$

Where:

Symbol	Unit	Description
$R$	$m$	Distance to radar echo
$c$	$\frac{m}{s}$	Speed of light
$\Delta t$	$s$	Time to and from radar echo

With such big propagations velocities even small errors in the timing of the radar can give big displacements errors. As with the orientation of the radar this can also be investigated from the radars ground clutter map. If the ground clutter is displaced on a straight line from the radar it could be an indication of wrong timing. If this is a general tendency for the entire radar precipitation field the displacement can easily be accounted for by multiplying with a constant factor.

### 2.1.3 Beam propagation

The emitted beams of the radar are not linear but propagation along curved lines. The reason for this is that the refractive index of the atmosphere is not one. Furthermore is the refractive index a function of temperature, pressure, and water vapour content and therefore changes both vertically and horizontally in the atmosphere. Depending on the atmospheric conditions the radar beam can propagate along three different paths see figure 2.3.

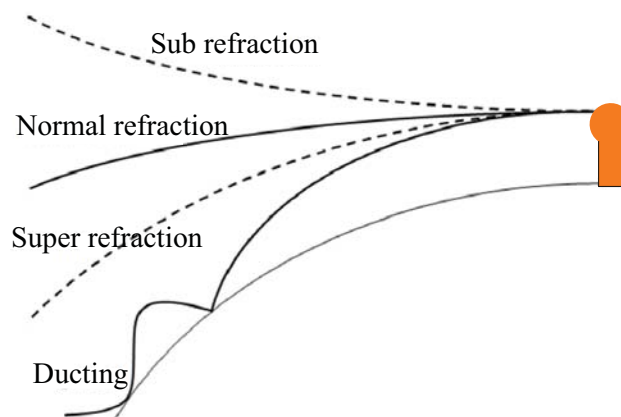


**Figure 2.3:** Different types of radar beam refractions in the atmosphere [Doviak and Zrnica, 1993, Modified].

The three normal refraction paths for the radar beam is sub refraction, normal refraction, and super refraction. Ducting happens rarely and is an extreme case of super refraction where the beam is being refracted down to the earths surface and reflected back up again just to be refracted back down [Rinehart, 1997].

Sub refraction occurs when the temperature rapidly drops as a function of altitude and makes the radar beam refract less than under normal conditions. Super refraction occurs with increasing temperatures as a function of height and therefore makes the beam refract more than under normal conditions. Refraction of radar beams are normally assumed described by simple relations. In section 4.1: *Conversion of radar data from polar to cartesian* is the subject described in more details.

### 2.1.4 Overshooting

Because of a combination of the curvature of the earth, radar beam refraction (especially sub refraction), and low laying precipitation can the radar beam overshoot the target. This normally happens in the outskirts of the radars range. In the outskirts of the radars range the echoes are not reliable due to the VPR and the height of the radar beam. Therefore is this uncertainty not something that will be described any further.

### 2.1.5 Beam shielding

Beam shielding is when an object are blocking the emitted radar beam and therefore limits the observations in that direction, see figure 2.1. In mountainous regions it is a big challenge to manage the shielding which have been examined by e.g. Andrieu et al. [1996] and Germann et al. [2006]. Beam shielding is normally easily observed with accumulated plots of the radars precipitation field over a longer period of time for example yearly accumulated plots. The shielding can be seen as areas with no accumulated precipitation.

### 2.1.6 Non-meteorological targets and clutter

Objects like swarms of insects and birds, aircrafts, wind turbines, tall ships and high waves etc. will also reflect the radar beam. In relation to weather radars it is important to be able to identify these echoes otherwise it will be perceived as precipitation. Non-meteorological targets, depending on which kind, can induce falsely high precipitation rates and therefore needs to be accounted for. Several automated schemes have been developed for detection and removal of the non-meteorological target. These schemes are often part of the radar software. For removal of non-meteorological targets Steiner and Smith [2001] and Sugier et al. [2002], to mention some, have developed automated schemes from volumetric radar scans that can detect and remove these echoes.

### 2.1.7 Attenuation of radar beam

Attenuation of the radar beam occurs because the emitted radar beam loses energy when being reflected from an object. How much depends on the density of the object causing the reflection. This is illustrated through an example shown in figure 2.4 where precipitation 1 reflects some of the emitted energy and therefore less energy reaches precipitation 2 this of course also occurs on the returning path from precipitation 2. The result is that precipitation 2 is estimated to have a lower precipitation intensity than it actually have. This can be very difficult to handle since it changes with the weather conditions. Many have tried to find a correction or adjustment method that incorporates the attenuation of the radar such as Battan [1973], Bringi et al. [2001] and Aydin et al. [1989].

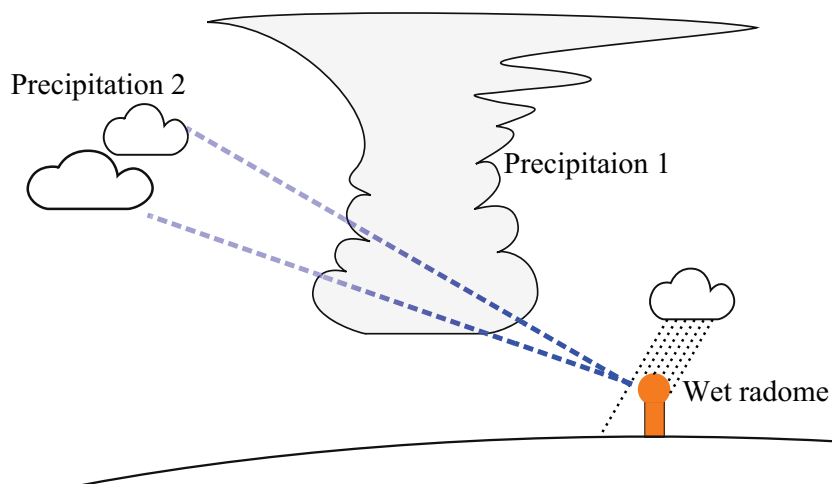


*Figure 2.4: Principle sketch of attenuation of the emitted radar beam.*

Attenuation of the radar beam can also be caused by water on the radome both when the energy is emitted and received. This is a constant attenuation of the entire precipitation field and are therefore easier to handle than the attenuation by precipitation events away from the radome.

The attenuation also depends on the wave length of the radars. In appendix A table A.1 on page 108 can a list of the different wavelengths and their usage be seen. With small wavelengths such as X-band weather radars the attenuation is the highest and the lowest with S-band weather radars. L and K band are not used for weather radars. Mt. Stapylton radar is a S-band radar.

There are several ways to check how the radar is being affected by attenuation. One way is to have a fixed point such as a high building, wind turbines etc. from which the reflectivity can be observed. The factor of attenuation is then the difference between the reflectivity from non-precipitation and precipitation in that specific direction. Another way is to have rain gauges or even better disdrometers along a transect in line from the radar. If the radar measures increasingly higher discrepancies between radar and disdrometer as function of distance from the radar this is also a measurement of the attenuation factor.

### **2.1.8 Verticale profile of reflectivity (VPR)**

To overcome ground clutter and beam shielding the elevation angle of the radar is above zero meaning that it emits its radar beam in a upwards angle from the ground (volume scans consists of several elevation angles). This, refraction and the curvature of the earth's surface does that the radar beam measures precipitation in different altitudes as a function of range. When the radar QPE is used as the precipitation intensity at ground level this can give rise to big differences in what is measured at the two different altitudes.

Within the vertical profile of the precipitation (depending on which type of rain and intensity) three layers can be observed; a layer with precipitation in form of snow, a melting layer also called bright band, and a layer with precipitation in form of water see figure 2.5. The energy reflected from the three layers are different with snow reflecting the least, the bright band layer the most and the precipitation in between the two which is also illustrated in figure 2.5.

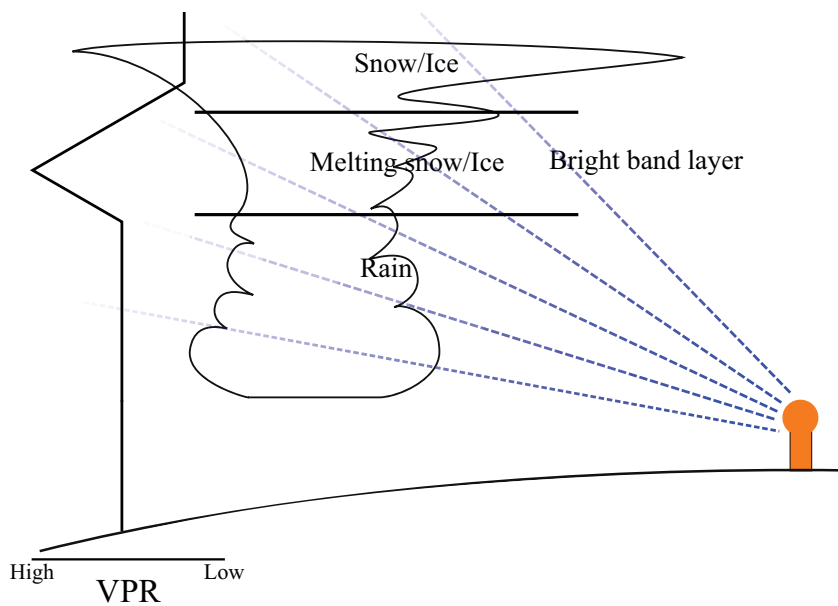


Figure 2.5: Vertical profile of reflectivity [RMI, 2012, modified].

The vertical structure of radar echoes in the radar beam is considered by Joss and Waldvogel [1990] as one of the dominant sources of errors in the measurement of precipitation by radar.

In order to account for this uncertainty identifying the VPR is important. Vignal et al. [1998] and Andrieu and Creutin [1994] have worked with identifying VPR from volume scans and from deterministic methods. Gray et al. [2001] and Seo et al. [2000] have tried to adjust the radar QPE based on the VPR. This has proved to be difficult due to the constantly changing conditions but as long as you can operate under the bright band layer the estimation is acceptable.

### 2.1.9 Variability in rain drop size distribution

The variability of rain drops size distributions is one of the fundamental problems of measuring precipitation with a radar. The problem is that the same precipitation intensity can consist of many small drops or few larger drops which again can vary in vertical speed depending on wind drifting. This difference in rain drop size distribution gives different surface areas from which the radar beam can reflect. Self-evident this induce that the reflected energy is not the same in the two situations even though the precipitation intensity is the same at ground level. Many people have worked with this problem from the first time a radar tracked a shower. The first to establish a conversion from reflectivity,  $R$ , into precipitation intensity,  $Z$ , a so called  $Z$ - $R$  relationship, was Marshall and Palmer [1948] see equation 2.2 and appendix A where the relationship have been derived.

$$Z = aR^b \quad (2.2)$$

Where:

Symbol	Unit	Description
a,b	–	Rain type and location dependent coefficients

Since 1948 much effort have been put into determining a correct and universal  $Z$ - $R$  relationship but it has been shown among others by Lee and Zawadzki [2004b] and Doelling et al. [1997] that this relationship is not static and can change several times within a single event. Lee and Zawadzki

[2004b] finds that a averaged  $Z$ - $R$  relationship based on five years of data gives a standard deviation of 41 % in instantaneous rain-rate estimation and 28 % with daily accumulated values. Even though this is the case the standard Marshall-Palmer equation is still widely used, see equation 2.3. Standard Marshall-Palmer equations meaning standard coefficients of  $a = 200$  and  $b = 1.6$  [Uijlenhoet, 2001].

$$R = \left( \frac{10^{Z/10}}{a} \right)^{1/b} \quad (2.3)$$

Systematic variations in  $Z$ - $R$  relationship was investigated by Doelling et al. [1997] which indicates a strong geographical dependence of drop size distributions. Clemens et al. [2006] and Peters et al. [2005] have used vertical doppler radars to investigate how the  $Z$ - $R$  relationship changes in vertical direction. Peters et al. [2005] finds that there is a significant height dependence for high rain rates  $R > 20 \frac{\text{mm}}{\text{hr}}$  within heights of only some 100 meters. If the rain rate is  $R < 20 \frac{\text{mm}}{\text{hr}}$  the dependency is more stable up to 1500 meters. For high rain rates the  $Z$ - $R$  relationship underestimate the actual rain intensity increasing with altitude. Furthermore Clemens et al. [2006] found during a longer strati form rain event that the  $Z$ - $R$  relationship changed four times. One way to handle this constant change in  $Z$ - $R$  relationship is to classify the type of precipitation and adjust the  $Z$ - $R$  relationship. This have been done among others by Straka et al. [1999], Rosenfeld et al. [1995], and Anagnostou [2004].

The above-mentioned indicates that this relation needs further investigation in order to find a correct conversion if the uncertainties has to be handled deterministic otherwise is a mean field bias adjustment needed.

### 2.1.10 Wind drift errors

When using radar QPE it is assumed that the precipitation observation measured aloft impacts the surface directly underneath the volume sample by the radar. As shown among others by Lack and Fox [2004], Mittermaier et al. [2004] and Collier [1999] this is not the case. They have shown that the wind can transport the precipitation distances of over 2 km and up to 10-20 km for snow [Mittermaier et al., 2004]. In figure 2.6 the wind drift effect of the rain can be seen.

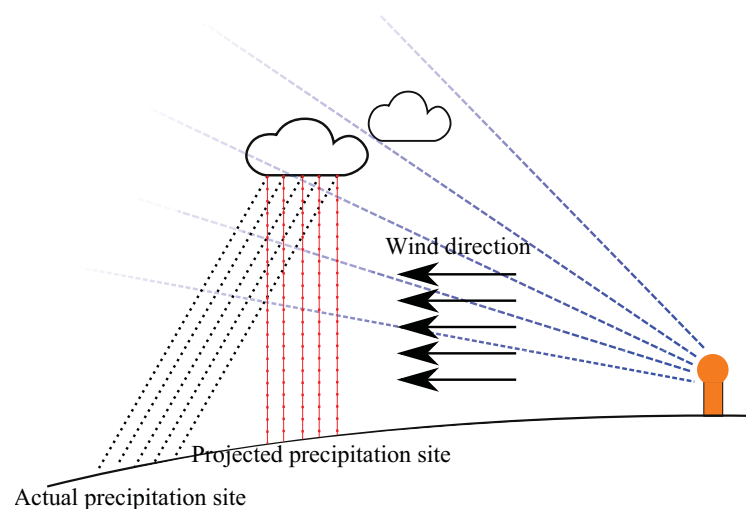


Figure 2.6: Wind drift of precipitation.

The higher the spatial resolution the higher uncertainty of the projected precipitation site. So with small catchments and high resolution radar this is major factor in the spatial distribution of the precipitation. Correction schemes for wind drifting using mesoscale model for wind is proposed by Mittermaier et al. [2004] and using doppler observations by Lack and Fox [2004]. Mostly this is not applied in radar QPE and therefore it is assumed that the precipitation measured aloft the surface falls in a straight line to the earth surface.

### 2.1.11 Interference

Interference of the radar signal can occur from different sources. Signals within the same range as the radar can be picked up by the radar and give false echoes. Besides interfering signals also background noise is present (cosmic noise etc.). Therefore does the radar needs to separate the desired signal from the ever-present noise and other interfering signals within the radar receiver, see appendix A for a description of how the radar works. Since the returning energy, reflected from precipitation, is relatively small the receiver also has to amplify the desired signal. This makes the radar vulnerable to interfering signals and hostile jamming (military use). Even though this is the case the receivers nowadays can filter most noise and produce almost interference free precipitation fields.

### 2.1.12 Remapping from polar to cartesian coordinate system

Besides orientation, timing, and wind drift another factor when projection the precipitation is how the remapping from a polar coordinate system to a cartesian coordinate system is performed see figure 2.7.

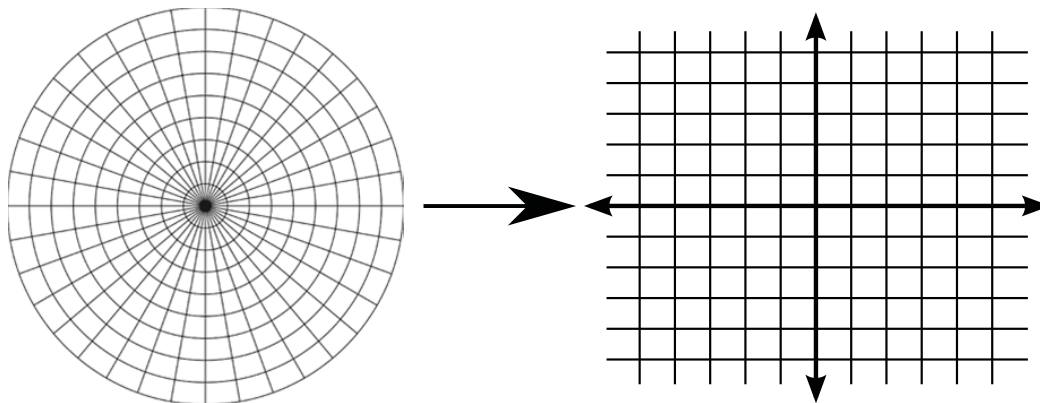


*Figure 2.7: Conversion of polar coordinate system into cartesian coordinate system.*

In a polar coordinate system is the density of observations heavy near the centre (radar location) with decreasing density moving away from the centre. The remapping needs to either relocate observations, interpolate to fill out the gaps in the cartesian coordinate system, or a combination of both. The uncertainty lies within filling in data in the areas with no observations to give a complete radar precipitation fields.

Different techniques have been developed to perform this operation. The most common techniques are nearest neighbour [Jorgensen et al., 1983], linear interpolation [Fulton, 1998], the Cressman weighting scheme [Weygandt et al., 2001], and exponential weighting scheme [Shapiro et al., 2003]. In chapter 4.1: *Conversion of radar data from polar to cartesian* is a more thorough description

found of this procedure performed on the data from Mt. Stapylton radar and also a discussion of the uncertainties.

### 2.1.13 Disussion of radar QPE uncertainties

As described in the preceding section there are many uncertainties related to radar QPE. Some of these uncertainties induces lower precipitation rates and others higher precipitation rates. The complex interaction of all the uncertainties is difficult to describe.

The uncertainties related to the catagory *Emitting radar signal*, see table 2.1, containing the uncertainties such as the orientation and timing of the radar, the beam propagation, and overshooting, is relatively easy handled and under normal conditions does not give problems. The reason for this is that, under normal conditions, these can be adjusted. The catagory of *Reflectivity* on the other hand is much more complicated to handle due to the constantly changing conditions. The uncertainties related to attenuation, VPR, and variability in rain drop size distribution are especially difficult and can have a big influence on the radar QPE. The three also interacts together and therefore makes it difficult to handle one at a time. The last category of *processing the reflectivity data* can have a big influence on the results but it depends on the methods used for post processing the data. This category is different than the preceding two because it not related to the actual measurement. The uncertainties related to remapping and projection of rain gauges, are therefore not assessed to be as important than the ones in the *Reflectivity* category.

The performance of a radar is normally evaluated by comparing radar QPE with rain gauge observations. A number of factors makes the comparison itself uncertain, which are described later on, so to investigate how uncertain the radar QPE are it has been evaluated against itself in the following section.

## 2.2 Radar vs. radar

The idea of evaluating the radar against itself is to leave out some of the uncertainties in comparison between radar QPE and rain gauge observations and to investigate how much the uncertainty related to radar QPE influences the measured precipitation field. For this comparison a Danish C-band radar owned by DMI is used. The two lowest laying elevation angles of the volumetric radar scan are used to compare against each other. This is possible because, the radar performs 10 scans in different elevation angles. Each scan is 360 degrees and is a snapshot of the precipitation field for the given elevation angle. The radar starts with the lowest elevation angle and performs a 360 degrees scan, adjusts the elevation angle on the fly and proceeds with the next. This gives two snapshots of the precipitation taken within a short period of time with almost the same elevation angles. For the DMI C-band radar the two lowest laying elevation angles are 0.5 degrees and 0.7 degrees respectively. In figure 2.8 can the precipitation field for the two be seen.

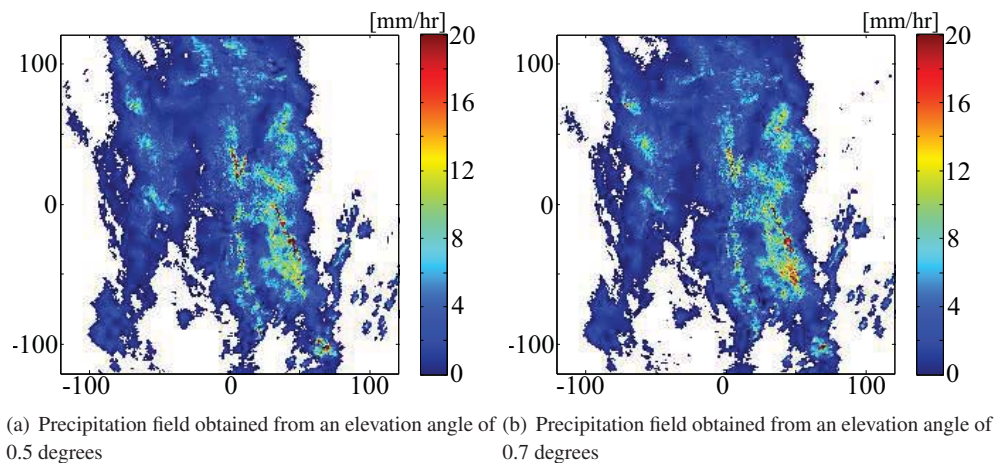


**Figure 2.8:** Radar QPE from DMI C-band radar May 22 2011 12:50 in two elevation angles; (a) 0.5 degrees and (b) 0.7 degrees.

Offhand the precipitation fields look very similar. They have the same structure and to some extent same intervals of precipitation intensity. Subtracting (a) from (b) shows another picture which can be seen in figure 2.9.

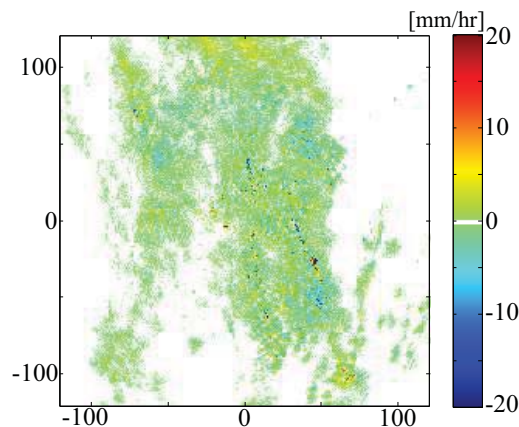


**Figure 2.9:** Difference between radar precipitation field (a) and (b).

Subtracting the two reveals some areas of discrepancies, especially in areas with high intensities. This could be due to horizontal movement of the precipitation from one pixel to the next. But from the doppler observations the horizontal movement of the precipitation is estimated to approximately 125 m over a time period of 6 min which therefore makes it unlikely since the two scans have been performed within approximately 30 sek. The most likely reason for the discrepancies is the changes in VPR and variability in rain drop size distribution.

Another thing that can be observed from figure 2.9 is a lot of smaller discrepancies in the low intensity areas. The reason for this is more difficult to give an estimate of since the sum of many, of the above described uncertainties, can be influencing. To investigate how the difference between the two are distributed a histogram and quantile-quantile plot have been produced, see figure 2.10.

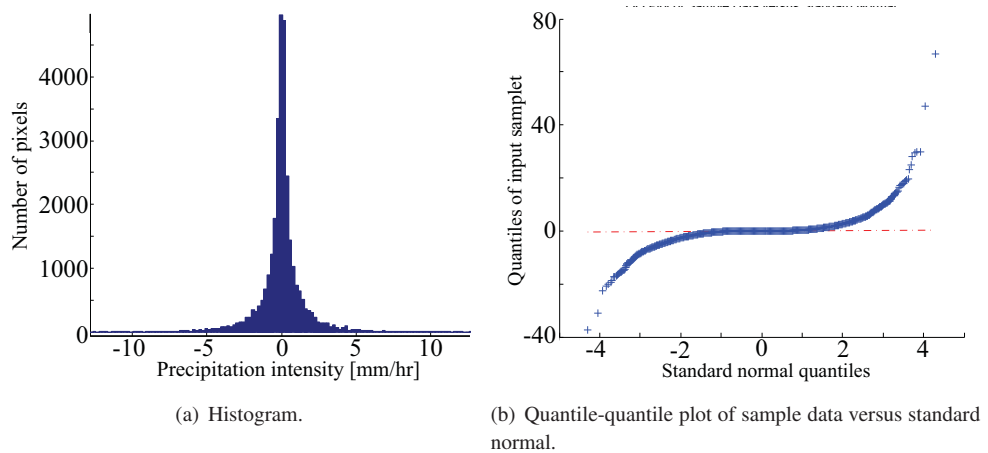


**Figure 2.10:** Histogram and Quantile-quantile plot of difference between precipitation field (a) and (b). The areas with no precipitation have been excluded from the histogram.

The histogram looks like a standard normal distribution. This has been investigated though the quantile-quantile plot. If the distribution, of the difference between the two precipitation fields, are standard normal distributed the blue data will be linearly along the red striped line. This is the case for the middle of the distribution but in the tails it is not normal standard distributed. This is interesting since the values in each end are relatively high compared to the actual precipitation fields (a) and (b). A reason for this could be either a change in altitude of bright band or moving clutter. The middle of the distribution, which correspond to minor differences, could be from cosmic background radiation or interference in general, which is presumable normal standard distributed.

What can be drawn out of this comparison is that even a scan of the almost the same precipitation field can give differences in results. These differences are overall small but noticeable especially in the tails of the distribution. It also indicates that the constantly changing conditions have an influence on the result which is very difficult to account for by deterministic approaches.

Since the probabilistic approach to describe the uncertainties in radar QPE, in this study, is based on a spatial error structure found by the residual error between radar QPE and rain gauges also the uncertainties of the rain gauges are important. Therefore in the following are the uncertainties related to measuring precipitation with rain gauges described.

## 2.3 Rain gauge uncertainties

This section describes the uncertainties of using rain gauges to measure precipitation. The rain gauges are important for this study because they are used as ground references for the probabilistic uncertainty estimation of radar QPE.

Queensland, Australia has a quite large network of automatic weather stations (AWS). The AWS measures air pressure and temperature, relative humidity, wind speed and direction, and precipitation. The rain gauge used to measure the precipitation is a RIMCO R/TBR-8 tipping bucket system. A picture of the rain gauge can be seen in figure 2.11.



*Figure 2.11: Rain gauge RIMCO R/TBR-8 tipping bucket system [McVan, 2012].*

A tipping bucket rain gauge is a simple construction that consists of a cylinder with an orifice in the top end. The rain falls into the orifice and travels down a funnel and drips into one of two buckets balanced on a pivot. The bucket is balanced such that it tips over with a given amount of water and a new empty bucket is ready to be filled up see figure 2.12.

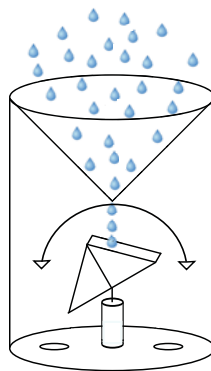


*Figure 2.12: The principle of a tipping bucket rain gauge.*

A logging device records every tip along with a time stamp. For the RIMCO R/TBR-8 tipping bucket every tip corresponds to 0.2 mm of rain. With the known time interval between each tip and the amount of rain the intensity is easily calculated.

When it starts to rain the first bucket fills up and the first tip of the rain event is recorded. In this initial phase it is unknown how much water that already was in the bucket from the last rain event and it is not possible to know over how long time the first tip have accumulated.

The uncertainty of the precipitation measurements is highest with very low and very high intensities. With a low intensity the tipping bucket system is vulnerable to evaporation and the precision because of its fixed precipitation depth of every tip. In high intensity precipitation the uncertainty also increases because of the time it takes for the bucket to tip from one side to the other. The constant tipping time induces that with high flow rates more is spilled in between tips.

Another factor that influences the accuracy of the rain gauges is wind. Depending on the wind direction and speed it is possibly the single largest uncertainty [Vejen et al., 1998]. The wind moves the precipitation horizontally and therefore changes the surface area of the rain gauge orifice. The effect of the wind is drop size depend which therefore also makes it very difficult to correct for in all situations. Precipitation with large drop sizes is less influenced than precipitation with small drop sizes. The worst case scenerio is therefore small drop sizes and strong wind. The effective oriface area changes therefore as a function of wind and rain drop size. With a decreased orifice area every tip does not correspond to 0.2 mm but a higher rain fall depth that induce that the rain gauge underestimates. The problem is depicted in figure 2.13.

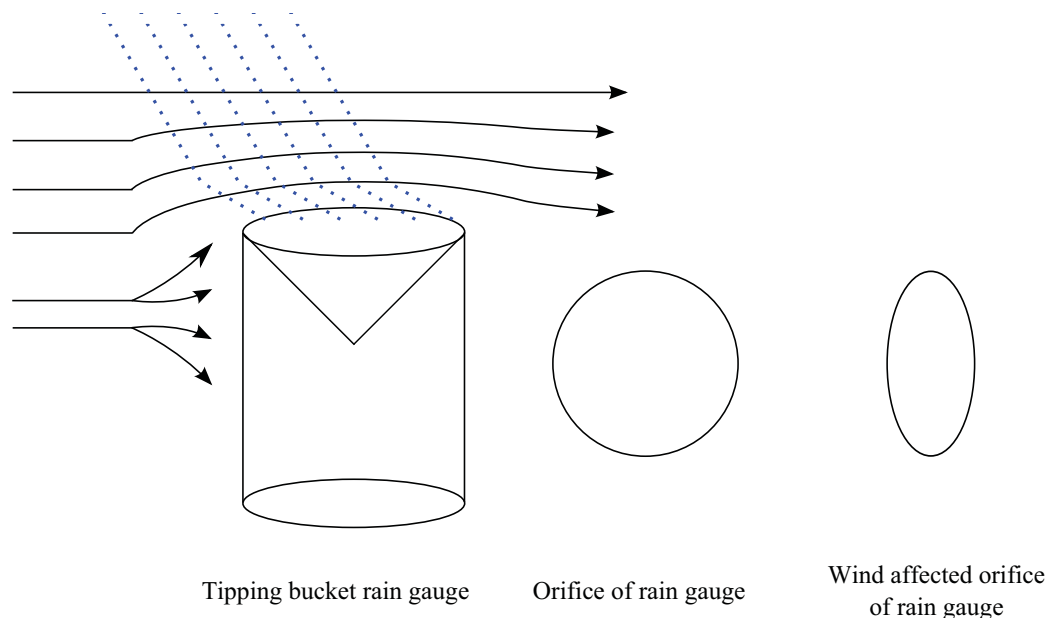


**Figure 2.13:** Wind affected rain gauge [Vejen et al., 1998, modified].

Many have worked with the uncertainties related to rain gauge measurements of precipitation. In Denmark mainly DMI (Danish Meteorological Institute) have worked with a correction scheme for wind [Vejen et al., 1998] and [Vejen, 2005]. Others that have worked with adjustment of tipping bucket precipitation measurement can be mentioned Habib et al. [2001], Ciach [2002], and Sevruck [1995]. Furthermore rain gauge uncertainties in relation to weather radar and numerical modelling have been investigated by Shahrban et al. [2011] and for forecasting Bowler et al. [2006].

Vejen [2005] concludes that a correction of 12-14 % is needed with accumulated rain events based on data from a time period of 10 summers. This indicates that there is a high degree of uncertainty related to rain gauge precipitation measurements. Furthermore if 12-14 % is needed for accumulated rain events even higher corrections can be expected when measuring on intensity level. Despite these uncertainties rain gauges are the most common used gauges for precipitation and considered reliable.

## 2.4 Representativeness error

Another fundamental problem is that the performance of weather radars is judged on how well it corresponds to a point measurement, rain gauges. In comparison between radar and rain gauge measurements a part of the scatter is a representativeness error (the differences between the sample volumes). Depending on how the radar data is resampled a typical spatial resolution is 2000x2000 m and a rain gauge is a point measurement, which makes them difficult to compare.

During the stay at The University of Queensland an experiment with 16 HOBO self-logging rain gauges was conducted. The gauges was set in a quadratic spaced grid of 15x15 m at Bribie Island with a measuring period during the wet season from November 2011 to March 2012 see figure 2.14.

The initial results shows a 23 % difference in averaged accumulated volumes between corner rain gauges (within 45 m) of convective events. This gives an indication that the spatial distribution varies even within small ranges. Furthermore this also tells something about trying to compare 2000x2000 m with a single point measurements. Ciach [2002] shows that with extensive post processing of the data that an average reduction in the root-mean-square difference between gauge and radar data of 30% can be achieved. If the representativeness areas is as large as a factor of three found by Kitchen and Blackall [1991] then what is the real precipitation measurement? Habib et al. [2004] tries

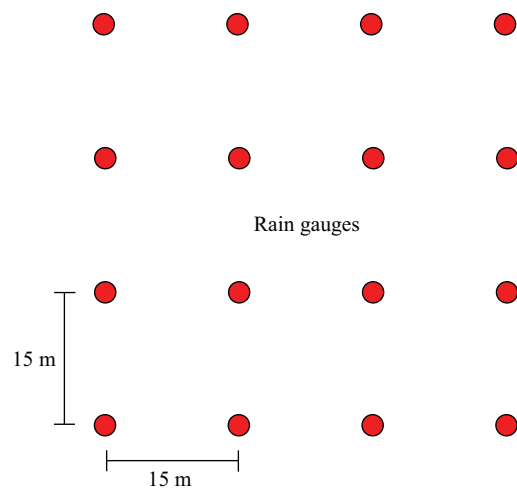


**Figure 2.14:** 16 rain gauges in a quadratic spaced grid.

to answer this question by proposing to filter out the representativeness error using a conditional distribution transformation method to find the "true verification distribution" to evaluate the radar precipitation field.

Today most radar derived QPE products are adjusted to fit the "ground truth" in form of rain gauges as described among others by Harrison et al. [2000] and Thorndahl and Rasmussen [2009]. The idea is that the radar has a good estimate of the spatial distribution of the precipitation and the rain gauge has a good estimate of intensities at ground level and combining these gives an overall good estimate. A problem is that the uncertainties related to the representativeness error is generally not taken into account and therefore makes the adjustment uncertain. Besides the representativeness error other factors also makes the radar QPE and rain gauge observations less comparable which are described in the following section.

## 2.5 Residual error discussion

The probabilistic approach for finding the uncertainties in this study are based on the error structure, expressed as the residual error, between the radar QPE and rain gauges. The residual error is defined as the discrepancy between the two types of measurements. This is illustrated in figure 2.15.

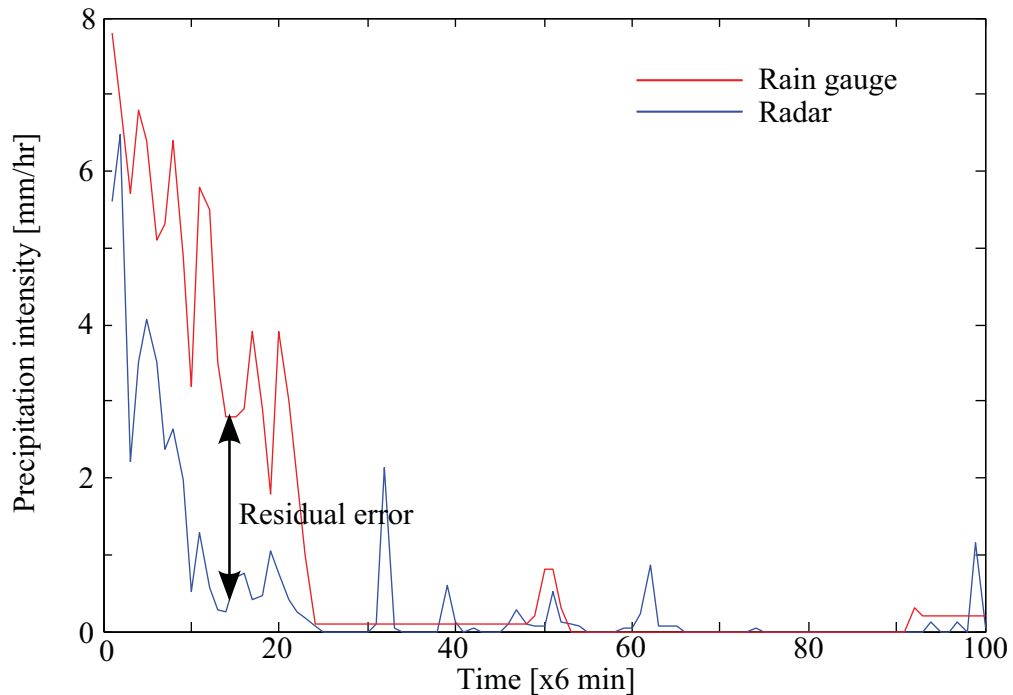


*Figure 2.15: Time series of precipitation intensity from radar and rain gauge.*

Besides the representativeness error of the rain gauges being point measurements and the radar covering 2000x2000 m and the rest of the described uncertainties, also the intervals of measurements makes the two less comparable. The Mt. Staplton radar scans 360 degrees in 14 elevation angles, more about this in section 4.1: *Conversion of radar data from polar to cartesian*. It is unknown how long time it takes for the radar to complete one scanning round but when completed 14 rounds (14 elevation angles) it goes on and performs its doppler observations. The total time for this is approximately 6 mins hence the 6 min intervals of the radar data. Every scan round is therefore a snapshot of the reflectivity somewhere within the 6 min intervals. This produces 14 snapshots in different elevation angles. When the radar data are processed into a constant altitude plan position indicator (CAPPI) image it consists of several snapshots in different elevation angles and therefore are time inconsistent. So comparing with rain gauges is difficult since the actual time of measurement is not certain. To make things worse are the rain gauge data from a tipping bucket system, which temporal resolution is a function of precipitation intensity, interpolation have therefore been conducted into intervals of 6 min. Therefore the residual error found between radar QPE and rain gauges are not time consistent. In figure 2.16 an illustration of the interpolation and residual error can be seen.

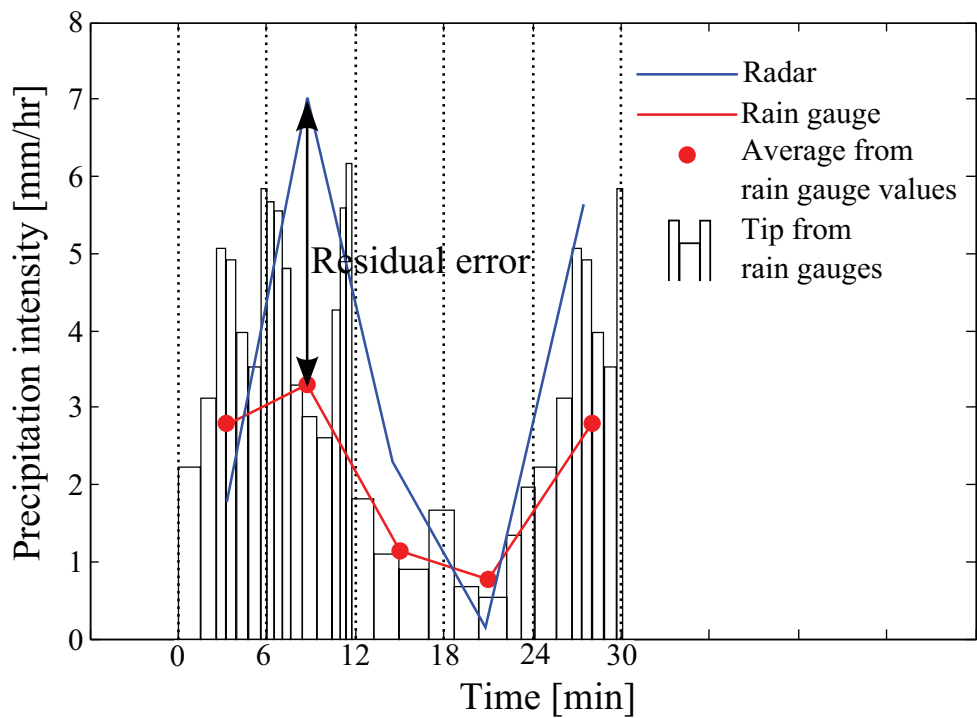


**Figure 2.16:** Interpolation of rain gauge values to 6 min temporal resolution.

Since it is a direct and easy way to describe the residual error and not many other choices are available this is the normal way to assess the performance of the radar. But talking about a residual error is not very precise, since the two methods measure different things to different times. Despite this in the following the residual error is defined as in figure 2.15.

In this study a probabilistic approach for finding the true precipitation field is set up for Bribie Island that incorporates radar uncertainties, rain gauge uncertainties and to some extent also the representativeness error. The advantage of this probabilistic approach is that several "true" precipitation fields are generated from the measured residual error between radar and rain gauges which therefore contain the uncertainties. In the following part the method and implementation of this probabilistic approach are described.

**PART**  
**II**  
**PROBABILISTIC UNCERTAINTY**  
**ESTIMATION**



# Methodology of ensemble generator

Despite of significant progress in the precision of radar QPE, the idea of using radar ensembles originates from the uncertainties as described in the previous part. A detailed estimate of error sources can be very complex and specific for the hardware, location, and weather. Since many of the errors are related to the constantly changing conditions it is difficult to post process the reflectivity data to give good estimates in all conditions and estimate the uncertainty. By adopting the fact that we cannot deterministically describe all the uncertainties, a pragmatic way to handle them is to generate realisations of the precipitation field based on a known error structure. Adding a stochastic element to the deterministic precipitation field gives multiple realisations which can be feed directly into hydrological models. We hereby get an ensemble of possible hydrological outputs, the spread of which represents the sensitivity of the hydrological system to the uncertainty in the radar precipitation fields on input [Germann et al., 2009]. This chapter describes the generation of ensembles used to feed the groundwater model of Bribie Island.

In generating synthetic precipitation fields several methods have previously been proposed. In 1985 Krajewski and Gerorgakakos [1985] generated synthetic precipitation fields by imposing random noise onto a radar field with known statistics. Such a procedure was made necessary by the lack of knowledge of the radar-noise field statistics. Later, in 2009, Germann et al. [2009] presented an ensemble generator based on the work by Krajewski and Gerorgakakos [1985] of imposing noise onto the deterministic radar image. The difference between the method proposed by Krajewski and Gerorgakakos [1985] and Germann et al. [2009] is that Germann et al. [2009] uses the knowledge of the spatial and temporal error structure in form of the residual error covariance matrix and an auto regressive model to give meaningful ensembles. Another method to generate ensembles is proposed by Pegram et al. [2011] which separates signal and noise by identifying a wavelength in the power spectrum which defines the variance threshold. The perturbations is hereafter generated as new noise terms.

Expressing the uncertainties by adding a stochastic element has been examined among others by Seed [2002] for nowcasting purposes and evaluated in a hydrological context by Berenguer et al. [2005].

The ensemble generator in this study is based on the work of Germann et al. [2009] since the produced ensembles can generate directly applicable time series for hydrological modelling.

### 3.1 Ensemble generator methodology

The overall idea of the ensemble generator is to perturb the deterministic radar precipitation field based on space-time structure of errors to produce realistic ensembles, see equation 3.1.

$$\Phi_{t,i} = R_t + \delta_{int,t,i} \quad (3.1)$$

Where:

Symbol	Unit	Description
$\Phi$	$mm\ hr^{-1}$	Resulting precipitation field (probabilistic)
$R$	$mm\ hr^{-1}$	Orginal unperturbed radar precipitation field (deterministic)
$\delta_{int}$	$mm\ hr^{-1}$	Perturbation field (stochastic)

By assuming that all radar errors are multiplicative the residuals can be described in dB (10-logarithmic space) where the residuals is describe by equation 3.2.

$$\varepsilon_t = 10 \log_{10} \left( \frac{S_t}{R_t} \right) \quad (3.2)$$

Where:

Symbol	Unit	Description
$\varepsilon$	$dB$	Residual error in 10-log space
$S_t$	$mm\ hr^{-1}$	True (unknown) precipitation field (rain gauges)
$R_t$	$mm\ hr^{-1}$	Radar precipitation field

Which hereby entails that equation 3.1 also should be described in dB, see equation 3.3.

$$10 \log_{10} [\Phi_{t,i}] = 10 \log_{10} [R_t] + \delta_{t,i} \quad (3.3)$$

Where:

Symbol	Unit	Description
$\delta$	$dB$	Perturbation field (stochastic)

The LU decomposition (Lower Upper decomposition) algorithm [Goovaerts, 1997] is used to generate the perturbations,  $\delta$ . The LU decomposition algorithm is based on multiplying Gaussian white noise with zero mean and unit variance with "the square root" of the Symmetric Positive Definite residual error covariance matrix and adding the mean error.  $\delta$  is hence modelled using multivariate statistical simulation. The residual error covariance matrix contains the spatial error structure and the temporal lag is modelled using a autoregressive AR(2) model see equation 3.4.

$$\begin{aligned} \delta'_{t,i} &= L y_{t,i} - a_1 \delta_{t-1,i} - a_2 \delta_{t-2,i} \\ \delta_{t,i} &= \mu + v \delta'_{t,i} \end{aligned} \quad (3.4)$$

Where:

Symbol	Unit	Description
$L$	–	The lower-triangular matrix
$a_1$	–	AR(2) model parameters (Yule-Walker equations)
$a_2$	–	AR(2) model parameters (Yule-Walker equations)
$v$	–	AR(2) model parameters (Yule-Walker equations)

### 3.1.1 Computation of spatial error structure

The spatial error structure is found comparing with a ground reference in this case rain gauges. By doing so any uncertainties from the rain gauges are incorporated into the computation of the mean error and the residual error covariance matrix (which hereby could be overestimated). Another way to find the error structure is to do a systematic analysis of the error sources, as described in section 2.1: *Uncertainties related to radar QPE*, but this is not obvious and having actual rain gauges with the same temporal measuring frequency as the radars time step the first solution is opted for.

The overall procedure goes as following:

1. Estimation of the residual error with equation 3.2.
2. Using the the residual error to find the mean error vector with equation 3.5:

$$\mu_k = \frac{1}{\sum_{t=1}^Q \omega_{t,x_k}} \sum_{t=1}^Q \omega_{t,x_k} \varepsilon_{t,x_k} \quad (3.5)$$

Where:

Symbol	Unit	Description
$\mu_k$	–	The mean error for rain gauge k
$\omega_{t,x_k}$	–	Weight set to the observed precipitation by the radar at timestep t and location $x_k$
$\varepsilon_{t,x_k}$	<i>dB</i>	Residual error in 10-log space
$Q$	–	Number of time steps

The mean error vector has dimension M which corresponds to number of locations x in the study area (number of pixels). By setting the weight to the observed precipitation it is avoided that irrelevant samples erroneously having large influence. In practice this means that the residual errors found from small precipitation intensities will be weighted less than the residual errors found from large intensities.

3. Estimate the variance which is later used in estimating the temporal error structure. This can be done in two ways either by estimating the residual error covariance matrix by equation 3.7 where the diagonal entries is the variance or simply by equation 3.6, which is a special case of equation 3.7.

$$C_{kk} = \frac{1}{\sum_{t=1}^Q \omega_{t,x_k}^2} \sum_{t=1}^Q \omega_{t,x_k}^2 (\varepsilon_{t,x_k} - \mu_k)^2 \quad (3.6)$$

Where:

Symbol	Unit	Description
$C_{kk}$	–	The variance for rain gauge k

The dimensions of the variance is the number of rain gauges used for determining the temporal lag.

4. Estimate the residual error covariance matrix by equation 3.7.

$$C_{kl} = \frac{1}{\sum_{t=1}^Q \omega_{t,x_k} \omega_{t,x_l}} \sum_{t=1}^Q \omega_{t,x_k} \omega_{t,x_l} (\epsilon_{t,x_k} - \mu_k) (\epsilon_{t,x_l} - \mu_l) \quad (3.7)$$

Where:

Symbol	Unit	Description
$C_{kl}$	–	The residual error covariance matrix between rain gauge x and l

Equations 3.5, 3.6, and 3.7 gives estimates at rain gauge locations only. Depending on the rain gauge location compared to the study area either extrapolation or interpolation is needed to estimate the mean error vector,  $\mu$ , with dimensions M and the residual error covariance matrix,  $C_{kl}$  with dimensions MxM. These estimators can be found once from historical data, assuming that the spatial error structure doesn't change in time. This represents the error characteristics averaged over the selected calibration dataset.

### 3.1.2 Computation of temporal error structure

The temporal lag is used for the second-order autoregressive model AR(2) filtering and is found at rain gauge locations and then averaged to obtain domain-average estimates, see equation 3.9.

$$r_{1,x_k} = \frac{1}{C_{kk}(x_k) \sum_{t=1}^{Q-1} \omega_{t,x_k} \omega_{t+1,x_k}} \sum_{t=1}^{Q-1} \omega_{t,x_k} \omega_{t+1,x_k} (\epsilon_{t,x_k} - \mu_k) (\epsilon_{t+1,x_k} - \mu_l) \quad (3.8)$$

$$r_{2,x_k} = \frac{1}{C_{kk}(x_k) \sum_{t=1}^{Q-2} \omega_{t,x_k} \omega_{t+2,x_k}} \sum_{t=1}^{Q-2} \omega_{t,x_k} \omega_{t+2,x_k} (\epsilon_{t,x_k} - \mu_k) (\epsilon_{t+2,x_k} - \mu_l) \quad (3.9)$$

Where:

Symbol	Unit	Description
$r_{1,x_k}$	–	Temporal lag 1 at rain gauge location $x_k$
$r_{2,x_k}$	–	Temporal lag 2 at rain gauge location $x_k$

### 3.1.3 Generation of perturbation fields

As mentioned briefly the generator of perturbations fields is based on the LU decomposition algorithm. The LU decomposition algorithm is enumerated in the following.

1. The symmetric positive definite (SPD) general covariance matrix is decomposed by Cholesky factorization into a lower-triangular.

$$C_{General} = L L^T \quad (3.10)$$

Where:

Symbol	Unit	Description
$C_{General}$	–	The general residual error covariance matrix
$L$	–	The lower-triangular matrix
$L^T$	–	The transpose lower-triangular matrix

2. A Gaussian random noise vector is generated with zero-mean and unit variance. The dimension should be  $M$ .

$$y_{t,i} = N_m(O, I)$$

Where:

Symbol	Unit	Description
$y_{t,i}$	–	Gaussian random noise vector
$N_m(O, I)$	–	$M$ successive calls to univariate normal generator

3. For the first two time steps the perturbation is calculated as equation 3.11

$$\delta_{t,i} = \mu + L y_{t,i} \quad (3.11)$$

4. For the remaining time steps the parameters for the AR(2) filtering are estimated by means of Yule Walker equations 3.12 [Priestly, 1981].

$$\begin{aligned}
 a_1 &= r_1 \frac{r_2 - 1}{1 - r_1^2} \\
 a_2 &= \frac{r_1^2 - r_2}{1 - r_1^2} \\
 \mathbf{v} &= \left[ \frac{1 + a_2}{(1 - a_2)(1 - a_1 + a_2)(1 + a_1 + a_2)} \right]^{-0.5}
 \end{aligned} \quad (3.12)$$

5. Hereafter are the perturbations found using equation 3.4 on page 40 which includes the AR(2) filtering.

The methodology now needs to be applied onto Bribie Island with one year radar data from Mt. Stapylton.

# Practical implementation<sup>4</sup> of ensemble generator

Before the methodology can be applied onto Bribie Island and the uncertainties of the Mt. Stapylton radar data can be estimated some processing of the data is necessary. It was chosen to acquire the radar data as completely raw reflectivity data in its native format. Australian Bureau of Meteorology (BoM) also has a radar derived product that is adjusted to fit rain gauges by a stochastic procedure (unknown to the author) which could be received in a range of formats. If the adjusted product was chosen much less processing would have been needed but for this study it is not an option since the probabilistic approach would not make much sense on already adjusted data. In the following section the first step in processing the raw reflectivity data from polar to cartesian coordinate system is described. In appendix B a flow diagram of the overall flow from extracting raw radar data to producing ensembles can be seen.

## 4.1 Conversion of radar data from polar to cartesian

The acquired data from Mt. Stapylton radar is in RAPIC format (the name comes from the Raptic Transmitter which was developed in 1984 by BoM). The RAPIC format is not native to Matlab which is the programming language used in this study, and therefore a conversion is needed. By permission from BoM a conversion tool is used to convert the data into HDF5 (Hierarchical Data Format 5) file structure.

The output from the conversion is a HDF5 file for each time step of 6 minutes. The data structure is divided in 14 datasets containing data1 and data2 which is the dBZ data and VRAD data (doppler) respectively. The 14 datasets correspondence to 14 different scan elevation angles. The different angles can be seen in table 4.1. In this study only the dBZ data is of interest since doppler velocities are irrelevant.

	Elevation angle [degrees]		Elevation angle [degrees]
Dataset 1	0.50	Dataset 8	5.60
Dataset 2	0.90	Dataset 9	7.40
Dataset 3	1.30	Dataset 10	10.00
Dataset 4	1.80	Dataset 11	13.30
Dataset 5	2.40	Dataset 12	17.90
Dataset 6	3.10	Dataset 13	23.90
Dataset 7	4.20	Dataset 14	32.00

*Table 4.1: The 14 scan elevations angles of Mt. Stapylton radar.*

The dBZ data is structured in a matrix with the azimuth angle in the row entries and bins along the column entries. The size of the data is [360 600] which corresponds to 360 degrees starting with zero pointing straight north and 600 bins. Every bin is 250 meters which gives a total slant range of 150 km.

The volume scans is reflectivity (dBZ) of water droplet density from 6 min intervals. This gives 3+ millions data points returned in a complex curvilinear coordinate system. Since the analysis of

the uncertainties of radar QPE is inconvenient in a polar coordinate system gridding into a cartesian coordinate system is needed.

Numerous approaches and techniques have been developed for remapping the observations. The most common techniques are; nearest neighbour mapping, linear interpolation, and the Cressman weighting scheme [Zhang et al., 2004]. In the current study the nearest neighbour mapping (NNM) and a derived version of NNM vertical horizontal interpolation method (VHI) are used for creating CAPPI images. The reason for trying both methods is to see which method fits the requirements of this study the best. The two methods are described in more detail later. In appendix C is the flow diagram of the program performing the conversion from polar to cartesian coordinate system illustrated.

#### 4.1.1 Ray propagation

Before being able to perform the actual remapping the rays need to be projected from slant range to arc distance (projected onto the earth's surface). This is illustrated in figure 4.1.

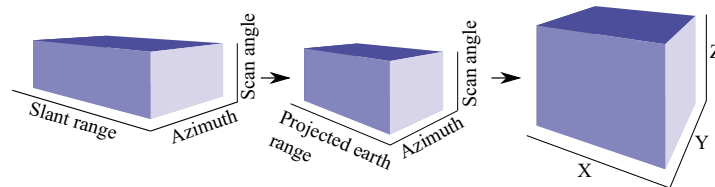


**Figure 4.1:** The original raw data corrected from slant range to earth projection range and finally regridded into a 3d cartesian grid.

This operation is necessary because the propagation paths of the radar rays are not linear but propagating along curved lines. They propagate along curved lines because of the permittivity in the atmosphere is larger than the dielectric permittivity (in free space). An illustration of how the rays propagate can be seen in figure 4.2 where Mt. Stapylton radar, with its 14 aforementioned elevations angles, is used as an example.

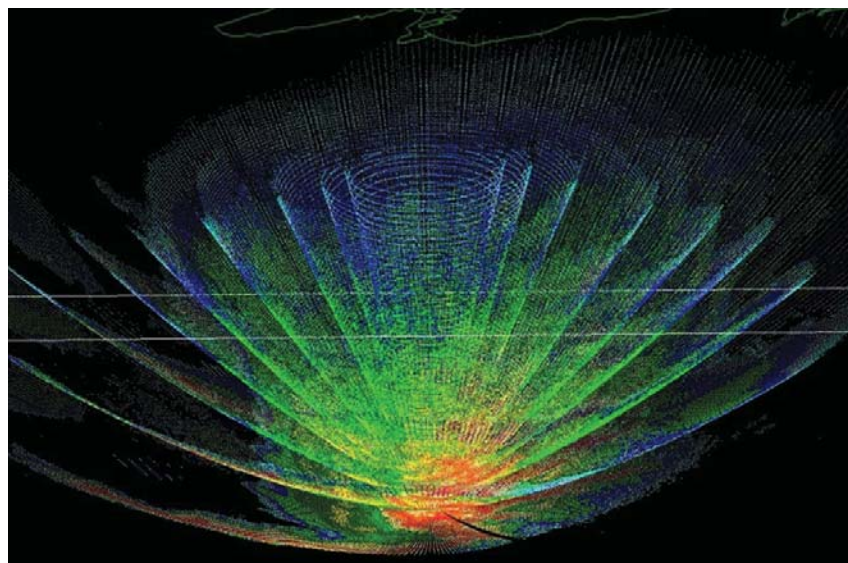


**Figure 4.2:** Principle of volumetric radar scan [Soderholm, 2011].

The atmospheric relative permittivity or the refractive index is related to temperature, pressure, and water vapour content and hereby changing both vertically and horizontally in the atmosphere. All the computations in this study assumes that the propagation of rays can be described by the  $\frac{4}{3}$ -earth model radius model [Doviak and Zrnicek, 1993].

$$a_e = \frac{4}{3}a \quad (4.1)$$

$$h(r) = (r^2 + a_e^2 + 2ra_e \sin(\theta_e))^{\frac{1}{2}} - a_e + h_0 \quad (4.2)$$

$$s = a_e \arcsin\left(\frac{r \cos(\theta_e)}{a_e + h}\right) \quad (4.3)$$

Where:

Symbol	Unit	Description
$a_e$	$m$	$\frac{4}{3}$ -effective earth radius
$a$	$m$	Earth's radius
$h$	$m$	Height of the center of the radar ray
$r$	$m$	Slant range
$\theta_e$	<i>Degrees</i>	Elevation angle
$h_0$	$m$	Transmit height of the ray
$s$	$m$	Distance between the radar and the projection of the bin along the earth surface

The propagation using the  $\frac{4}{3}$ -earth model radius model can be seen in figure 4.3. It shows the height of the rays due to refraction as a function of the distance between the radar and the projection of the bin along the earth surface (Arc distance).

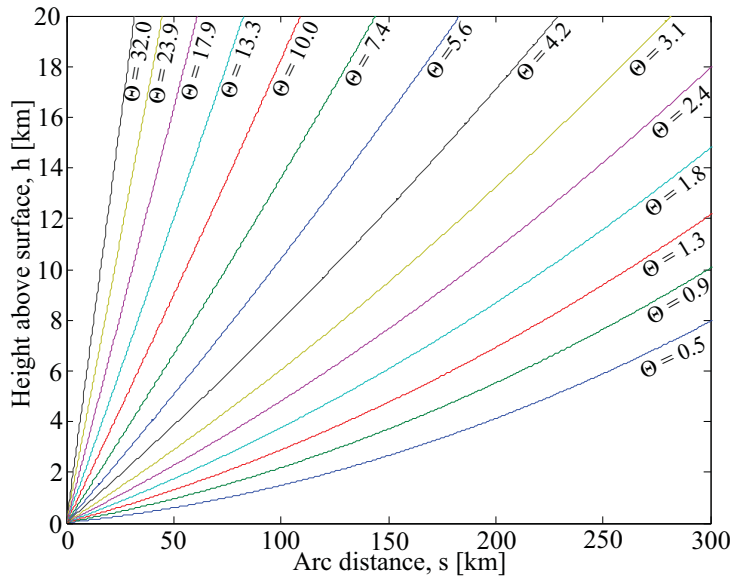


**Figure 4.3:** Height of the radar beam above the earth surface as a function of arc distance (projection on earth surface). The 14 scan lines corresponding to each elevation angle as seen in table 4.1.

Performing this operation prior to the actual remapping gives a better performance of the conversion. The next step is to do the actual remapping of the observations.

### 4.1.2 Remapping methods

As mentioned the two methods tried in this study are the NNM method and a derived version hereof, VHI method.

NNM assigns the value of the closest radar bin to grid cell, where distance is evaluated from using the location of centres of grid cells see figure 4.4.

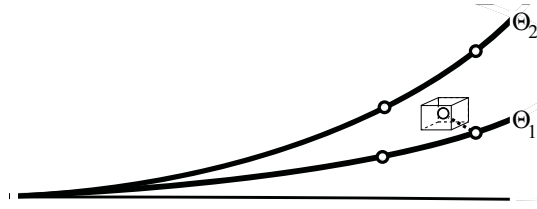


Figure 4.4: NNM method of remapping from polar to cartesian coordinate system.

The VHI method describes more the trend of the data within the same azimuth angle since it interpolates both vertically and horizontally. The vertical interpolation makes an interpolation between the two closest scan lines in the vertical direction. The horizontal interpolation makes an interpolation from the two closest bins along the closest scan line. In figure 4.5 and 4.6 this is illustrated. The average from the two interpolations is assigned to the given grid cell.

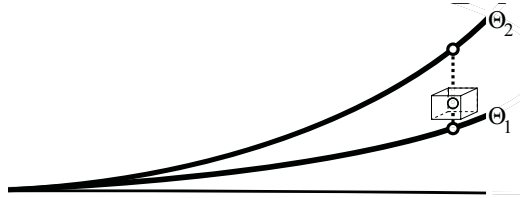


Figure 4.5: Outline of the vertical interpolation method.



Figure 4.6: Outline of the horizontal interpolation method.

The output from the remapping is a 3D matrix with the size of initially decided grid where the vertical layers consists of CAPPI images.

### 4.1.3 Conversion of reflectivity into rain rate

The methodology of the ensemble generator is based on radar data in rain rates and not reflectivity. Therefore is it needed to convert the reflectivity data  $[dBZ]$  into rain rate  $[\frac{mm}{hr}]$ . The formula used is based on the theory described in appendix A and is with standard Marshall Pallmer coefficients, see equation 4.4 [Rinehart, 1997].

$$R = \left( \frac{10^{Z/10}}{200} \right)^{0.625} \quad (4.4)$$

The output is the same size 3D matrix as the input but all values are in  $[\frac{mm}{hr}]$ .

#### 4.1.4 Choice and discussion of NNM method vs. VHI method

The difference between the two methods is not that distinct for lower CAPPI images of 1 km and 2 km, a comparison from 2 km altitude can be seen in figure 4.7. With increasing altitude in heights of 3 km and 4 km are the distinction more obvious see figure 4.8.

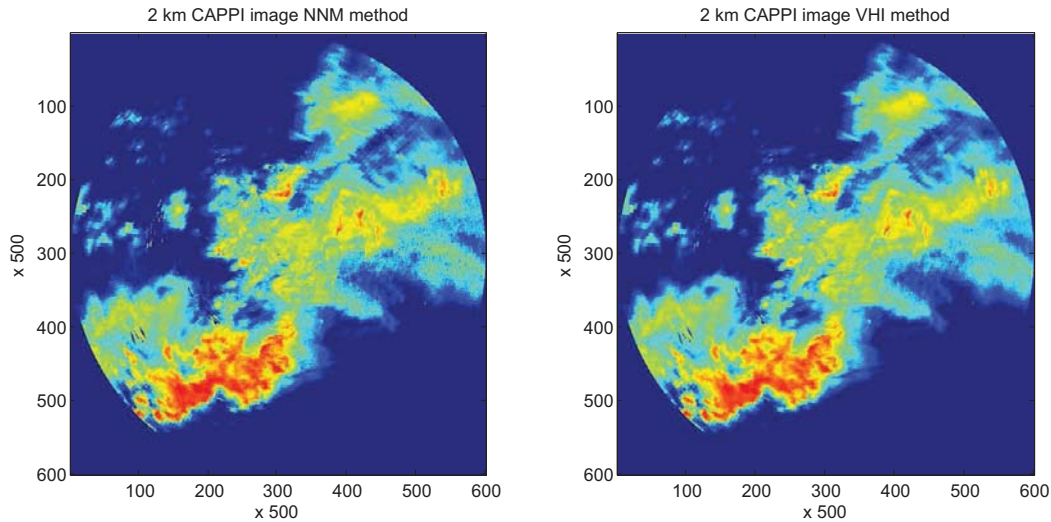


**Figure 4.7:** Mt. Stapylton radar 2 km CAPPI images created with nearest neighbour mapping from 2008 11 16 0754 YYYY MM DD hhmm.

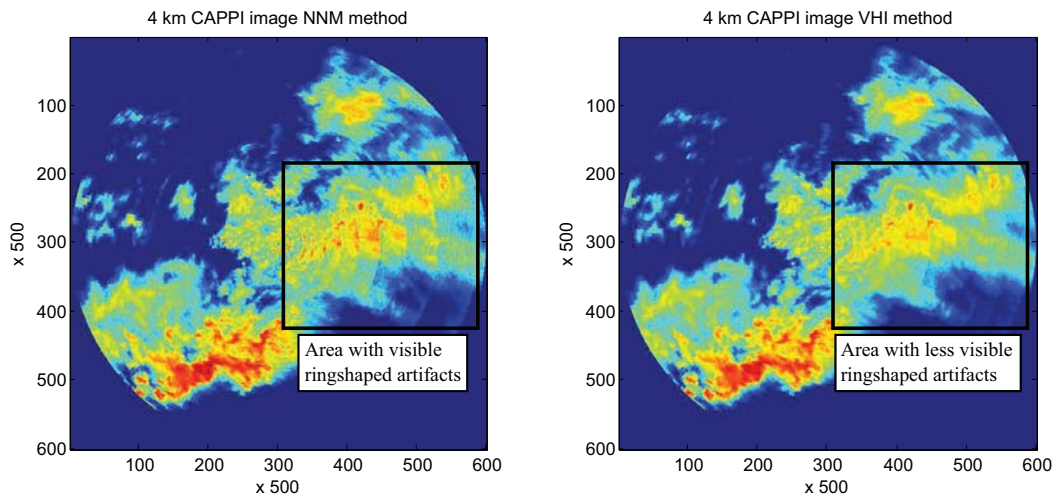


**Figure 4.8:** Mt. Stapylton radar 4 km CAPPI images created with vertical and horizontal interpolation from 2008 11 16 0754 YYYY MM DD hhmm.

The ring-shaped artefacts seen in the 4 km CAPPI image using NNM method is due to the way radar rays is refracted in the atmosphere and the not even distribution of elevations scanning angles. The NNM method cannot describe the tendency in between the rays but simply move the observations. The similar 4 km CAPPI image produced with VHI method do also have some tendency of creating ring-shaped artefacts but it is not as distinct as with NNM. The reason why the ring shaped artefacts increases with altitude is because the density of observations is larger at 2 km than at 4 km which can be seen in figure 4.9.

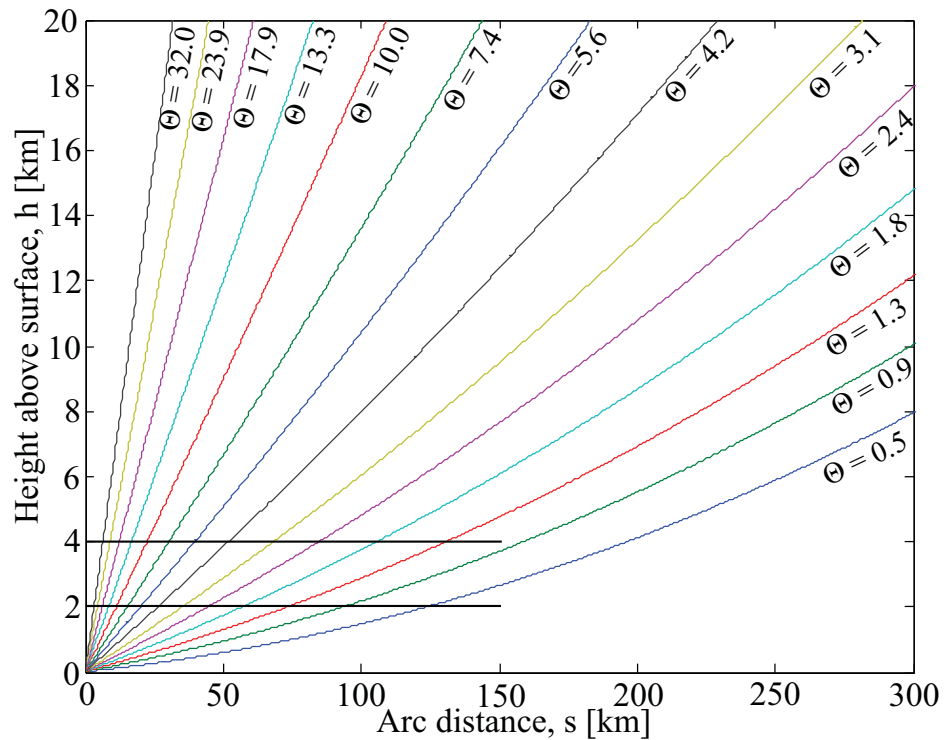


**Figure 4.9:** The vertical location of CAPPI images projected on the path of the radar ray. The CAPPI line ends at 150 km which is the slant range of Mt. Stapylton.

Another factor that needs to be considered is that the observations can be remapped over large distances with both NNM method and VHI method. The longer away from the radar the less observations per area and hereby a bigger probability of observations being relocated over larger distances. This can make the radar QPE in the outer edge of the radar displaced. If a third dimension interpolation was added to the remapping method so eight observations, on two concurrent azimuth angles, where used this could be minimized. This would help describe the tendency in between the azimuth angles and therefore not only relocated observations.

An advantage with the NNM method compared to the VHI method is that the high peaks and variability is not being smoothened. So a high gradient from grid cell to grid cell is obtained. To improve the VHI method a distance weighted interpolation would help to keep this variability within the precipitation field.

Which gridding method should be used depends on the purpose and available computation time. NNM is less computational than the VHI method. Processing time for 6 min data with the NNM method is approximately 30 % quicker than the VHI method with a remapping grid of [1000x1000x4]. When processing large amount of data or running real time applications the computational time is of great importance. It also depends on which CAPPI elevation is needed. If CAPPI images of 2 km and lower is needed and computational time is critical a NNM would be preferred. If higher CAPPI elevations are needed the VHI method should be applied but with the cost of extra computational time.

This study is based on historical data so the computation time is not critical. Furthermore can the ring-shaped artefacts add more uncertainty to the probabilistic approach and therefore is the VHI method opted for. The CAPPI height has been chosen to 2 km and the spatial resolution to 2000x2000 m since it is sufficient for the needs of this investigation.

With the data remapped into CAPPI layers and converted to rain rates is it possible to compare the

radar QPE with the rain gauges. This is the subject of the next section.

## 4.2 Computation of residuals between radar and rain gauge

As described in chapter 3: *Methodology of ensemble generator* are the perturbations based on the error structure between the radar observations and rain gauge observations. The following describes how the residuals between the two are found. In appendix D and appendix E can the work of preparing the rain gauge data for this comparison and the flow diagram of the program performing the computation of the residuals be seen.

As a request from BoM all the available rain gauge data within the range of Mt. Stapylton was acquired this meant data from a total of 109 rain gauges. When processing the data most of the rain gauges was discarded either because of missing data from the time period as the radar data or because of predominant faulty data. Only a total of 9 usable rain gauges remained after processing of the data.

Before it is possible to find the residuals the projection of the rain gauges and radar precipitation field needs to be the same. The radar is projected onto the earth surface during the remapping with the radar as centre and the range of the radar along its axis. It is therefore not projected into UTM GDA94 which is the projection of the rain gauges. It has been chosen to project the rain gauges from UTM GDA94 into the radars grid because it is more convenient, programming wise, than the other way around. The function that calculates the projection of the rain gauges into the radar grid is based on haversine functions that incorporate the curvature of the earth's surface, see equation 4.5 and 4.6.

$$\text{haversin}\left(\frac{d}{r}\right) = \text{haversin}(\phi_2 - \phi_1) + \cos(\phi_1) \cos(\phi_2) \text{haversin}(\varphi_2 - \varphi_1) \quad (4.5)$$

When expressed with sin and cos knowing that  $\text{haversin}(\theta) = \sin\left(\frac{\theta}{2}\right)^2 = \frac{1 - \cos(\theta)}{2}$  equation 4.5 becomes equation 4.6.

$$d = 2r \arcsin\left(\sqrt{\sin\left(\frac{\phi_2 - \phi_1}{2}\right)^2 + \cos(\phi_1) \cos(\phi_2) \sin\left(\frac{\varphi_2 - \varphi_1}{2}\right)^2}\right) \quad (4.6)$$

Where:

Symbol	Unit	Description
$d$	$m$	Distance between the two points (along a great circle of the sphere)
$r$	$m$	Radius of the sphere
$\phi_2$	$m$	Latitude of point 2 (radian)
$\phi_1$	$m$	Latitude of point 1 (radian)
$\varphi_2$	$m$	Longitude of point 2 (radian)
$\varphi_1$	$m$	Longitude of point 1 (radian)

To find the actual grid coordinate of the rain gauge in the radar image the spherical distance between the radar and rain gauge were found for x and y separately. The distance is found in meters which are easily converted into the radar image when the grid size and the radar location are known.

With the rain gauges projected into the radar grid a direct comparison is made for every time step and the residual is computed with equation 3.2 on page 40. In figure 4.10 examples of observations between radar and rain gauges can be seen.

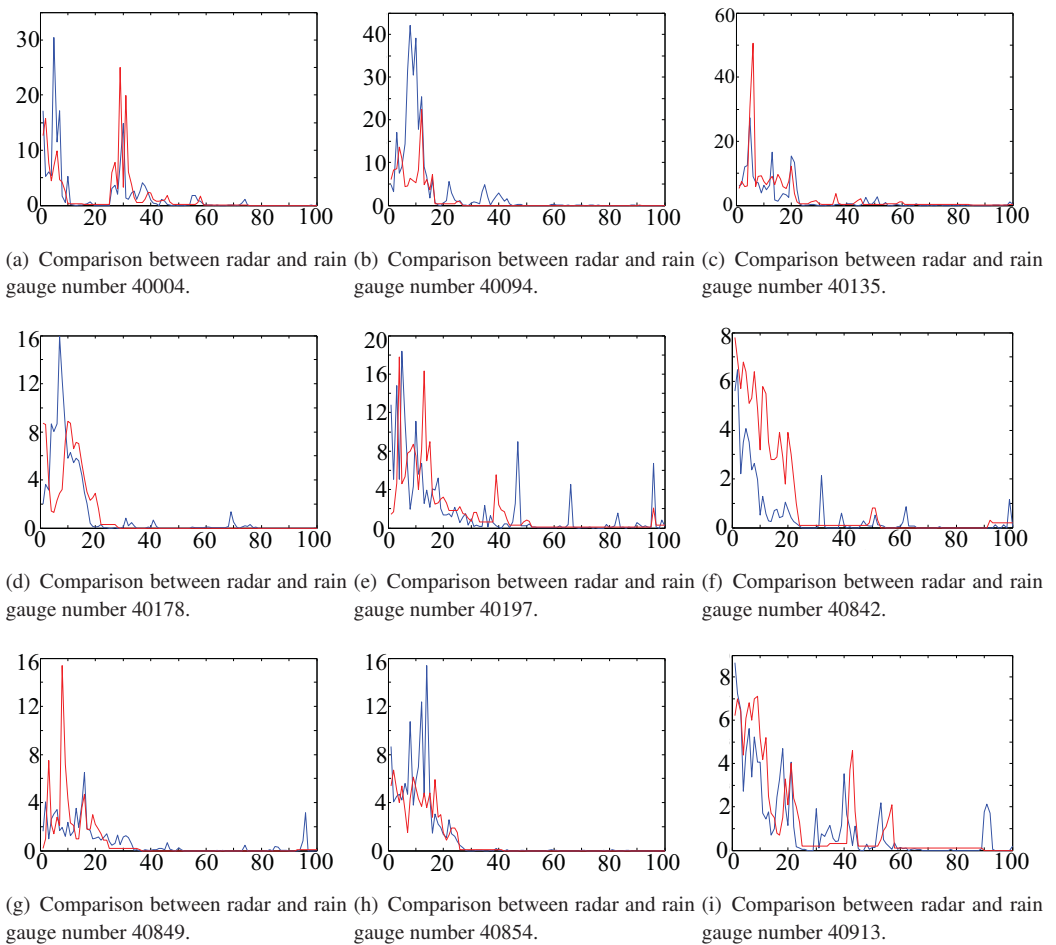


**Figure 4.10:** Examples of radar and rain gauge values from 2011 01 11 14:00 to 2011 01 11 23:54. Red line is rain gauge values and blue line is radar values. On the x-axis is time (x 6 min) and the y-axis is rain rate  $\left[\frac{mm}{hr}\right]$ .

The radar QPE used in the comparisons plots shown in figure 4.10 are based on standard Marshall Palmer coefficients in the conversion from reflectivity to rain rates. Since the standard coefficients are used, bias is most likely present between rain gauge and radar data. The normal procedure hereafter is to bias correct the radar data. A bias correction can be done by plotting the observed radar values vs. the rain gauge values and determine the best fit regression line from the scatter points with origin in origo. If no bias is observed then the slope of the regression line is approximately 1. If the slope is not 1 then a factor is multiplied onto the radar data to achieve a slope of 1, assuming that the rain gauges are the ground truth.

It has been chosen not to do the bias correction of the radar data used to produce perturbations with since the ensemble generator should be able to remove the bias via the mean error and therefore generate bias free ensembles. Still the bias is being investigated to have an idea of how well the ensemble generator removes the bias and to see how well the radar performs. The bias, for the individual rain gauges, can be seen from the following scatter plots, in figure 4.11.

## 4.2 Computation of residuals between radar and rain gauge

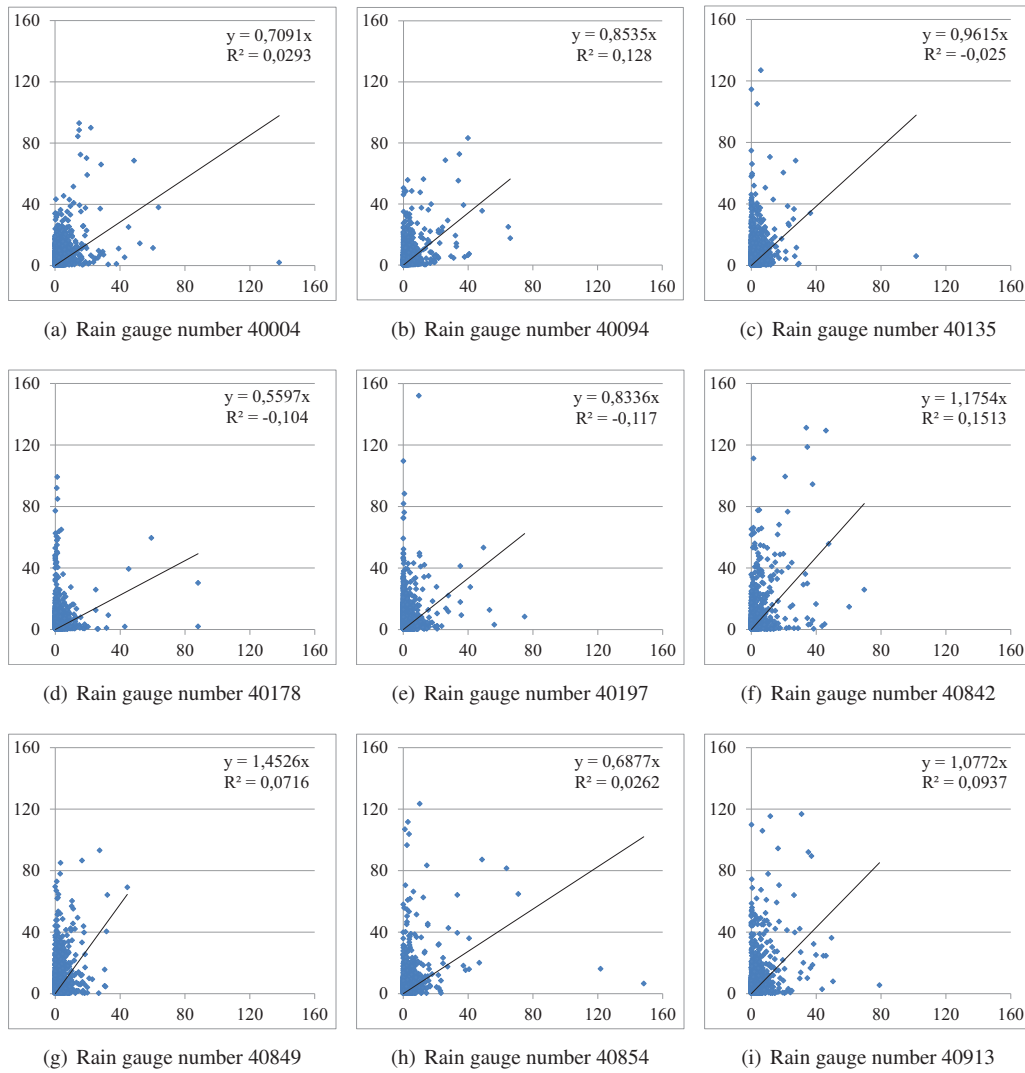


**Figure 4.11:** Scatter plots of radar and rain gauge values. X-axis radar values  $\left[\frac{mm}{hr}\right]$  and Y-axis rain gauge values  $\left[\frac{mm}{hr}\right]$ .

In comparison with the individual rain gauges the radar both overestimates and underestimates. For six of the rain gauges the radar underestimates and for three it overestimates. The spread ranges from 0.5597 to 1.4526. The reason for this spread can be a bias within the rain gauges itself but could also be range dependent according to the propagation of the radar rays and the VPR to mention some, see chapter 2. In order to determine how much the radar data has to be bias corrected all rain gauge data and radar data are plotted in the same scatter plot, see figure 4.12.

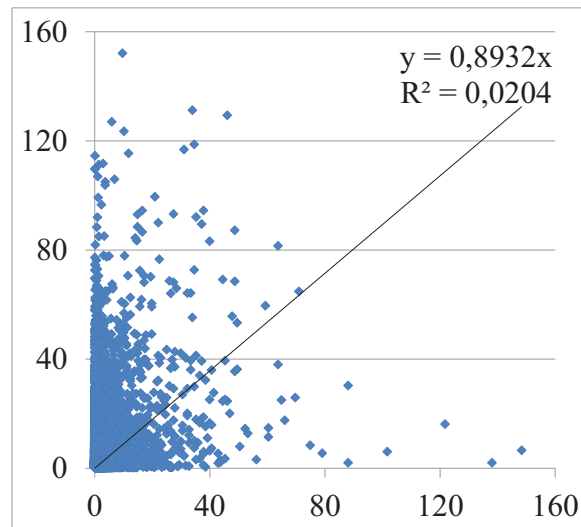


**Figure 4.12:** Scatter plots of radar and rain gauge values. X-axis radar values  $\left[\frac{mm}{hr}\right]$  and Y-axis rain gauge values  $\left[\frac{mm}{hr}\right]$ . The dataset contains all rain gauge values in one plot.

To remove the bias from the radar data a factor of 0.8932 has to be multiplied. The performance of the radar is acceptable having in mind that this is the smallest timescale possible (6 min intervals), even though the  $R^2$  is only 0.0204. The bias correction is as already mentioned not performed on the radar data used in the ensemble generator but only on a comparison dataset used to compare with the bias correction from the ensemble generator.

Having computed the residuals between radar and rain gauges from which the spatial error structure is based on, the next step is to go on with the actual ensemble generator.

## 4.3 Ensemble generator

With the computed residuals between radar and rain gauges the base for going on and implementing the ensemble generator is present. The implementation is done in three steps starting with the space and time structure of errors. In appendix F can flow diagrams of the program producing the ensembles and the time series be seen.

### 4.3.1 Estimation of space-time structure of errors

Before executing the LU (lower upper) decomposition some preliminary computations are needed. Firstly estimating the spatial error structure that consists of the mean error matrix, the variance, and the covariance matrix from equation 3.5, 3.6, and 3.7 on page 42. Secondly the temporal error structure which consists of the temporal lag parameters for the AR(2) filtering estimated from equation 3.9 on page 42.

The mean error is estimated at rain gauge locations only. Therefore interpolation into the area of Bribie Island is needed. From an interpolation of the full radar precipitation field the mean error matrix covering Bribie Island is extracted. The mean error matrix over Bribie Island based on one year of historical data and can be seen in figure 4.13.

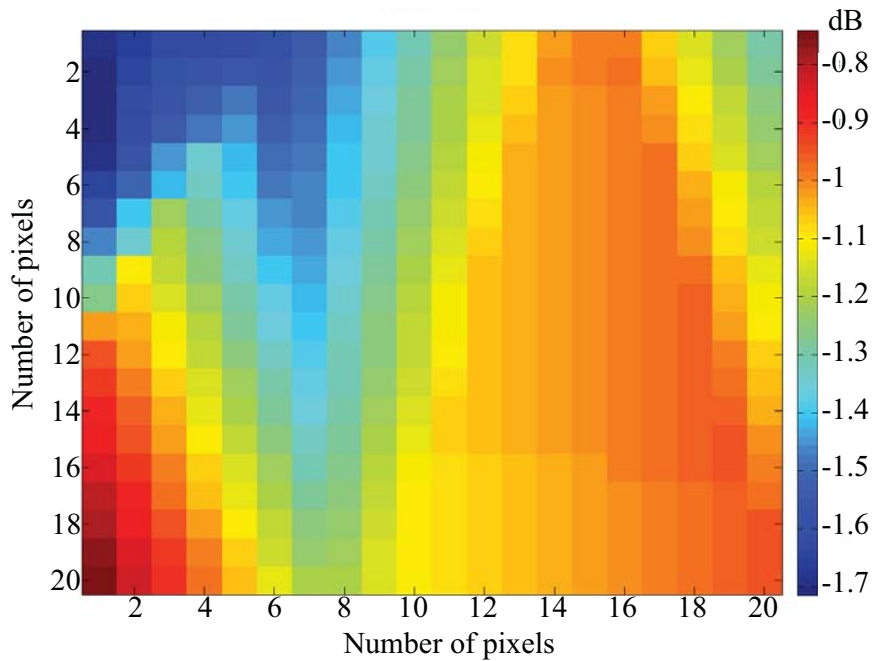


**Figure 4.13:** Mean error matrix interpolated from mean error values based on data from May 2010 to May 2011.

Since the mean error matrix is below zero it indicates that the radar in general measures higher intensities than the rain gauges. This was also concluded from scatter plots between radar and rain gauges see figure 4.12. As described earlier the bias is corrected with the mean error matrix and since it is below zero the ensembles will be lower than what is deterministic observed by the radar.

The covariance matrix is computed from covariance values that describes how coherent the residual error between two rain gauges varies. So the number of possible combinations to compute the covariance values are  $(\text{number of rain gauges})^2$  and therefore is the dimensions  $M \times M$ . The variance values are the diagonal in the covariance matrix and will therefore not be described further.

Because of the large dimensions of the covariance matrix interpolation was conducted in a smaller area of  $50^2 \times 50^2$  instead of  $150^2 \times 150^2$ . This was done to make interpolation quicker and in general less computational. Furthermore this made it possible to exclude areas with no usable rain gauge data. The chosen interpolation method is kriging with a spherical variogram model. From the full  $50^2 \times 50^2$  interpolated covariance matrix a smaller one of  $20^2 \times 20^2$  are extracted as the general covariance matrix used for perturbations. Why an area of  $20^2 \times 20^2$  are extracted is because it is sufficient to produce perturbations overlaying Bribie Island and therefore makes the computation less heavy. Which part that is extracted is subjective since the interpolation area does not cover Bribie Island. The extracted covariance matrix is then assumed to be general and applicable to produce ensembles all over the precipitation field. It was chosen to extract from (800,800) as the lower left corner of the full covariance matrix. This choice could have been avoided if rain gauge data was available on Bribie Island (or surrounding Bribie Island). In figure 4.14 can the kriging interpolation area of  $50^2 \times 50^2$  and the extracted area of  $20^2 \times 20^2$  used for creating perturbations be seen.

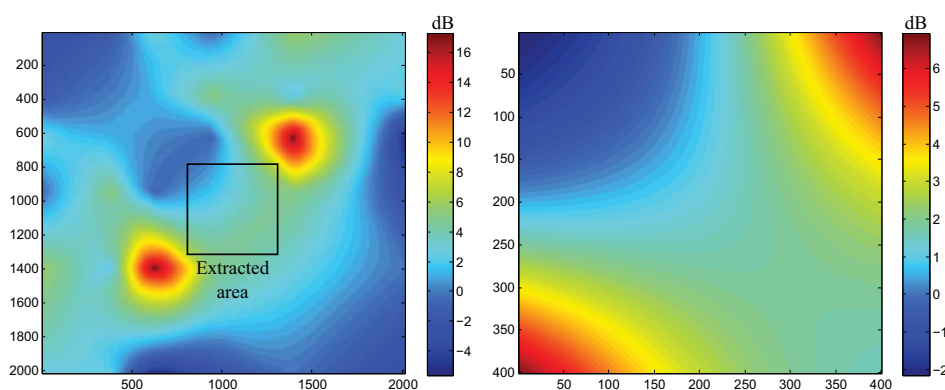


Figure 4.14: Left kriging predictions and right extracted general covariance matrix.

The spatial error structure here expressed as the covariance matrix indicates that the residual error is mostly co-varying except for the lower left corner. The range of the matrix from approximately -2 to 6 also indicates that the perturbation can be positive, because they are higher than the mean error matrix, and therefore produce ensembles larger than the radar QPE.

### Manipulation of covariance matrix into SPD

Covariance matrices generated from sample data, as in this case, are generally not positive definite (PD) [Velasco-Forero et al., 2008]. A real  $n \times n$  matrix,  $M$ , is positive definite if and only if  $z^T M z > 0$  for all non-zero vectors  $z$  with real entries  $z \in \mathfrak{R}^n$ . In other words this means that the eigenvalues should all be positive. There exists several ways to manipulate a non PD matrix into a PD matrix. An advanced method is proposed by [Tao and Journel, 1997]. The method involves weighting the covariance method by a radial moving scheme, using FFT to convert into the spectral domain, smooth the data under constraints following Bochner's theorem, and then inverse transform by FFT. Another method programmed by [Strauss, 2003] is called the Alternating-projections method. In this method the nearest covariance matrix that obeys the PD criteria is found from the non PD matrix. This is done by scaling the matrix to an indefinite correlation matrix using the alternating-projections method and rescaling to a covariance matrix. In cases where the covariance matrix is very close being PD (numerical roundoff errors) the negative eigenvalues can be manipulated into  $0 + eps$ . Another method of manipulating the negative eigenvalues is proposed by [Scheffer, 2010] where the negative eigenvalues are summed,  $S$ , and the most negative value are found,  $P$ . Then the new non negative eigenvalues are computed by equation 4.7.

$$D_{new} = P \left( \frac{(S - D_{old})(S - D_{old})}{(S^2 \cdot 100) + 1} \right) \quad (4.7)$$

Where:

Symbol	Unit	Description
$D_{new}$	—	The new non-negative eigenvalue
$D_{old}$	—	The old negative eigenvalue

Not only one method can in all cases make a non-PD matrix PD. For example can the alternating-projections method only converge if the original non-PD matrix is already close to being PD and simple manipulation where negative eigenvalues are set equal to  $0 + eps$  gives a completely different and unusable matrix than the original. Therefore in this study a combination of methods have been applied to ensure a versatile approach. The approach is enumerated in the following five steps.

1. Ensure symmetry by mirroring at the diagonal of the matrix.
2. Two times smoothing of the matrix by a running mean with a window of 50x50.
3. Cutting off the high frequencies using a low pass filter.
4. Manipulation of negative eigenvalues with the method proposed by Scheffer [2010].
5. Ensure symmetry by mirroring at the diagonal of the matrix.

In figure 4.15 the covariance matrix shown is generated from one year of historical data (from May 2010 to May 2011) and is the one used for generating perturbations. The figure shows before and after the manipulation of the matrix along with the low and high pass filter.

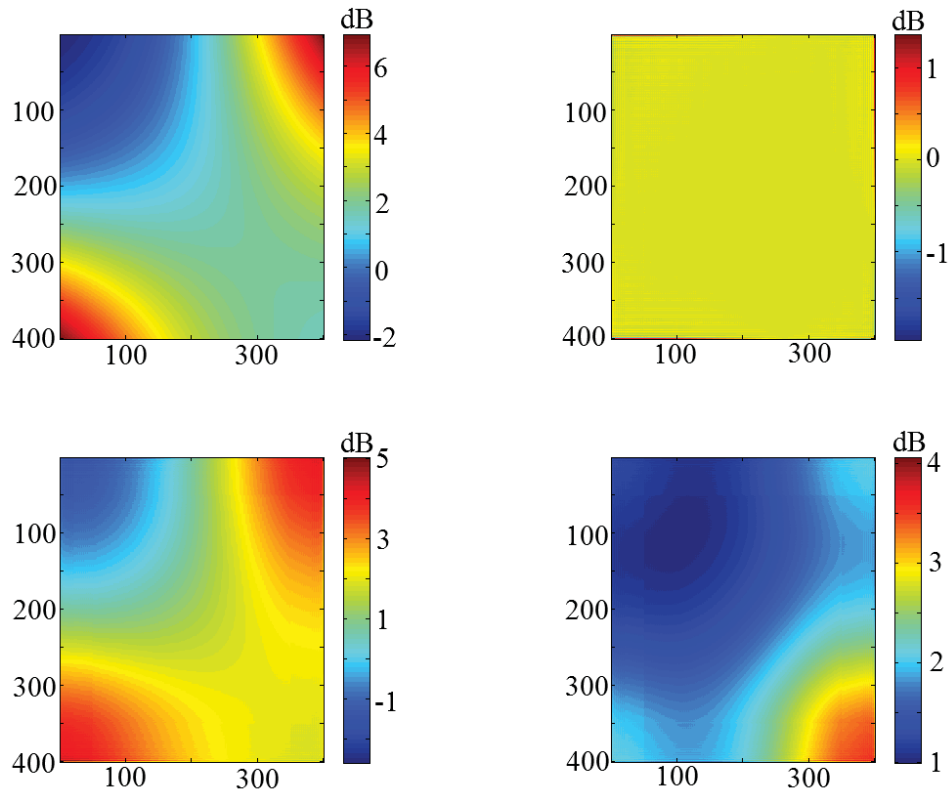


**Figure 4.15:** The matrices are based one year of data. Upper left is the covariance matrix before any manipulation, upper right is high pass filter, lower left is the low pass filter, and lower right is the manipulated covariance matrix.

Even though the low pass filter only filters a small amount, which can be seen in the upper right figure, it is in most cases necessary to make the matrix PD.

The stronger non-PD the original matrix is the higher degree of manipulation is needed. More manipulation also induces bigger changes between the original non-PD matrix and the manipulated PD matrix. In this specific case the original matrix is strong non-PD which can be observed as the difference in the overall structure of the matrix before and after manipulation.

The perturbations are generated from the shown covariance matrix and the changes have been found acceptable. It is found acceptable because of the high degree of interpolation and the subjective choice of where to extract the covariance matrix. These factors could have bigger influences on the covariance matrices than the manipulation.

When ensured that the matrix is SPD the Cholesky factorization finds the lower triangulation matrix see equation 3.10 on page 42.

### 4.3.2 Generation of perturbations fields

The generation of the perturbations fields is conducted according to the methodology of the ensemble generator as described in chapter 3: *Methodology of ensemble generator* since it could be more or less directly implementation on Bribie Island. The only modification of the methodology was that if the radar QPE precipitation intensity was under  $0.5 \frac{\text{mm}}{\text{hr}}$  the perturbations were set to zero. Examples of the perturbations can be seen in chapter 5: *Testing and results of ensemble generator*.

### 4.3.3 Difficulties producing SPD error covariance matrix.

Producing the covariance matrix proved to be the most difficult part of the ensemble generator. The location of Bribie Island was the biggest challenge since naturally no rain gauges are located to the east of the Island and no actual rain gauge data from Bribie Island are available for the given time periode.

Another difficulty in producing the covariance matrix was that the size of the matrix which can be very large depending on the size of the study area. For instance if perturbations was to be created on the entire precipitation field the covariance matrix would be of dimensions  $150^2 \times 150^2 = 22500 \times 22500$  with resampled data from Mt. Stapylton radar in  $2000 \times 2000 \text{m}$ .

Because of the challenges producing a usable covariance matrix, that was not too computational, several ideas was tried before obtaining the one described earlier.

The first idea to overcome the problems was to extrapolate the covariance values into the area of Bribie Island and take out a  $400 \times 400$  covariance matrix (since only a  $20 \times 20$  area are needed to be perturbed). There were two problems with this method. One that the rain gauges containing data usable for computing residuals (and hereby covariance values) were located far from Bribie Island and two that extrapolation in  $150^2 \times 150^2$  dimensions are too demanding for normal pc's.

Then the second idea was to make several smaller sub areas of  $400 \times 400$  containing covariance values and extrapolate. Then average these sub areas to produce one general covariance matrix applicable to produce perturbations over Bribie Island. The idea is illustrated in figure 4.16.

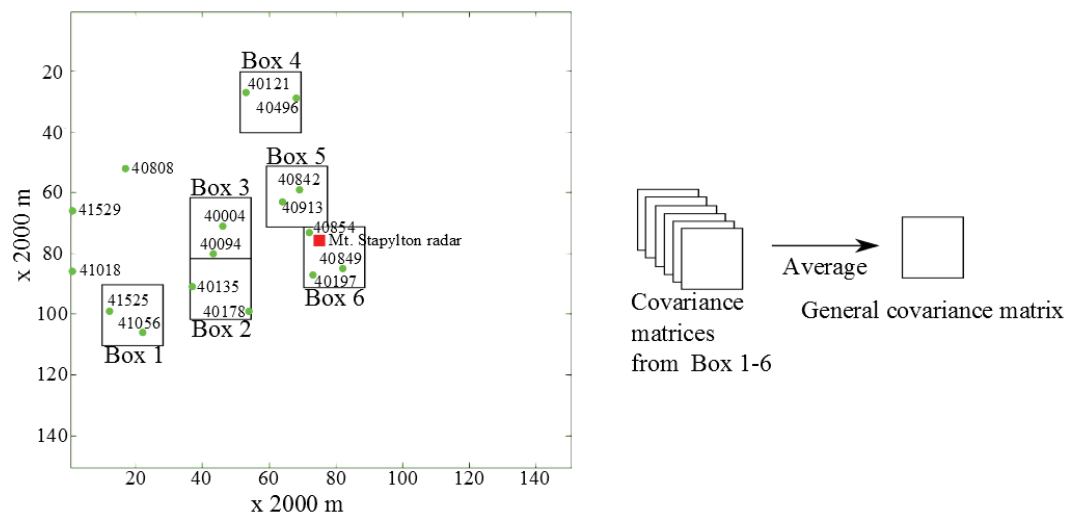
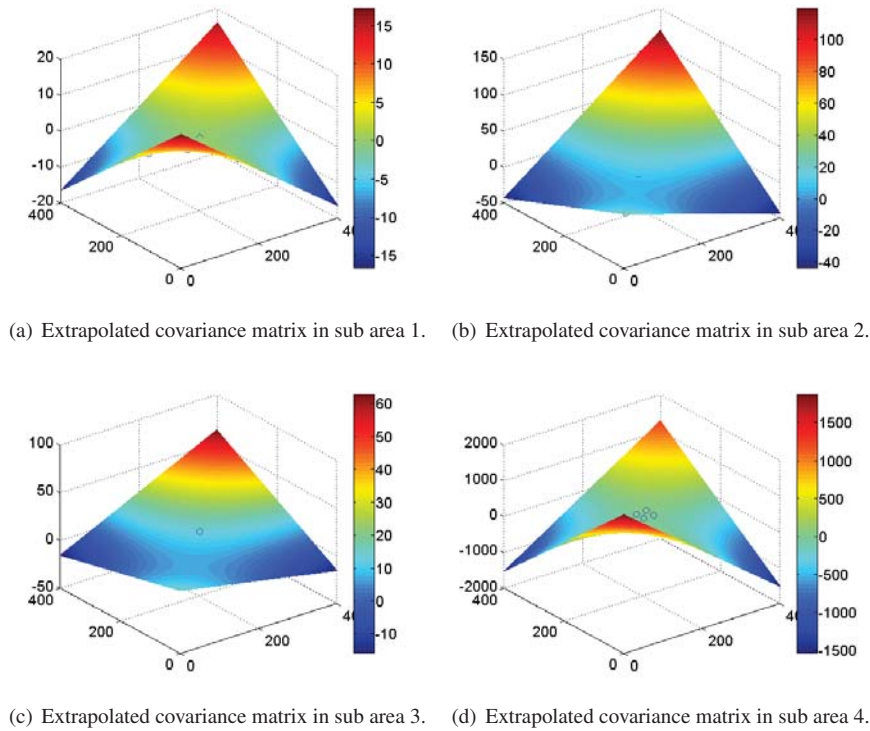


Figure 4.16: Conceptual idea of creating a general covariance matrix.

This approach deviates from the method proposed by [Germann et al., 2009] but has the advantage that the general covariance matrix can be used to produce perturbations in the entire radar precipitation field since the covariance matrix is general. Furthermore it is less computational with large study

areas. By using this approach it was needed to assume that the correlation length of the rain gauges is small enough not to have an influence among the subdivided covariance matrices. The method had two fundamental problems, one that all the spatial error structure was not preserved and two that extrapolation from few values can give extreme values the further away from the extrapolation points it is. In figure 4.17 these problems can be observed.



**Figure 4.17:** Examples of extrapolated sub areas produced from January 2011 residuals.

If the averaged general covariance matrix was to be used to produce perturbation these would have been unrealistic large. For these reasons this approach was discarded.

The third approach tried was opted for. This method was, as already described, interpolating the area containing rain gauges and then extract a covariance matrix as the general covariance matrix. The advantage of this method is that it is quick and applicable in all situations. The disadvantage with this method is that it is subjective which part of the full covariance matrix is extracted. Another issue is the assumption that the extracted covariance matrix can be used to describe the error structure of the entire radar image. If this was to be investigated rain gauges should be available all over the radar image. Which is not the case. Another way to investigate if the general covariance matrix is applicable to the entire precipitation field is to look at the orographic difference within the radars range. If the orographic changes are small the variability in the residuals error could be expected to be similar in the precipitation field. If this is the case the covariance matrix would have differences in structure from location to location but would be within the same range. Furthermore having small orographic changes also induces a limited range in dB of the covariance matrix compared to e.g. mountainous areas where higher ranges within the covariance matrix would be expected. Having covariance matrices within the same range but different structures would not produce that different ensembles in the end. The orographic difference have been investigated by looking at the accumulate rain from the period of May 2010 to May 2011 from the Mt. Stapylton radar. The more homogeneous the precipitation is less orographic differences are observed. As an argument of using a general covariance matrix the bigger differences in rain fall could induce a more complex error

structure. It should be mentioned that this is not directly linked since it is the covariance of the residual error between rain gauge locations. The accumulated rain fall can be seen in figure 4.18.

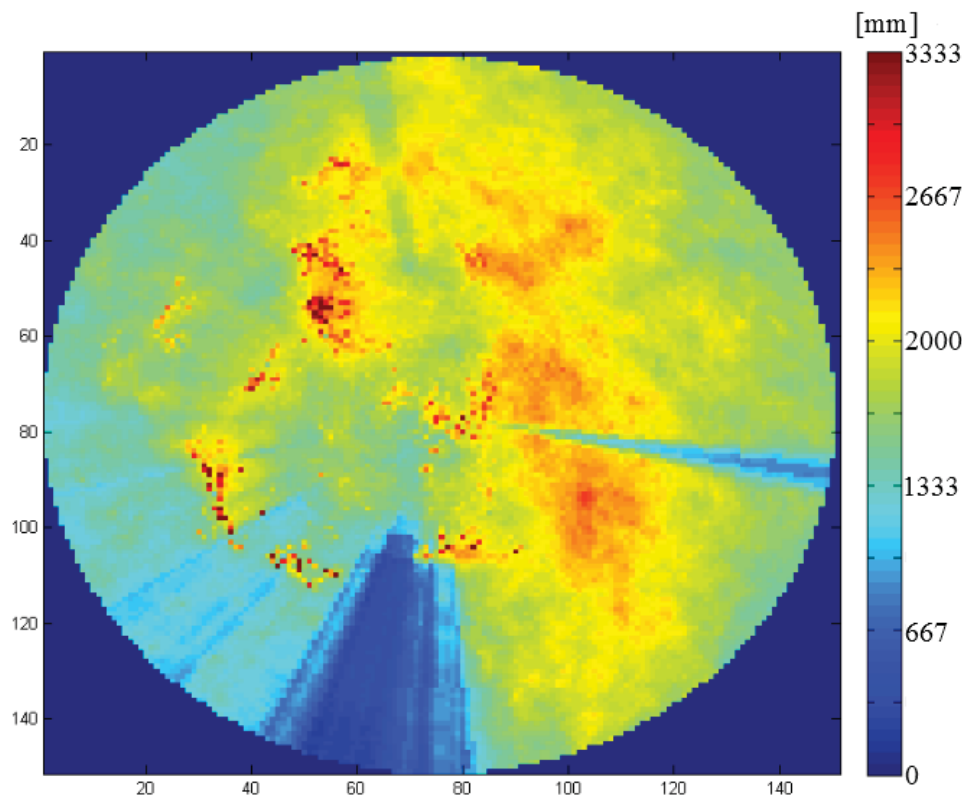


*Figure 4.18: Accumulated rain fall from May 2010 to May 2011 [mm/hr].*

From the figure partly shielding can be observed to the south and east. Along the coast slightly more accumulated rain fall are observed and since Bribe Island are located along the coast a slightly different error covariance pattern could be expected than the one over land. When that's said the covariance matrix describes how well the residual errors co-vary with each other and therefore these are not directly coupled to the accumulated precipitation.

# Testing and results of ensemble generator

To ensure that the ensemble generator behaves as expected it needs to be tested. During the programming of the ensemble generator tests have been conducted and in the following section the most important tests are described.

## 5.1 Testing the ensemble generator

The first two tests are to verify that the mean error matrix and the covariance matrix are produced correctly. These tests are based on synthetic data and consist of constant residual errors and residuals generated from Gaussian white noise.

With a constant residual of 1.5 dB the mean error matrix should be constant of 1.5 dB and the covariance matrix zero. In figure 5.1 the mean error matrix and the covariance matrix produced from constant residual error can be seen.

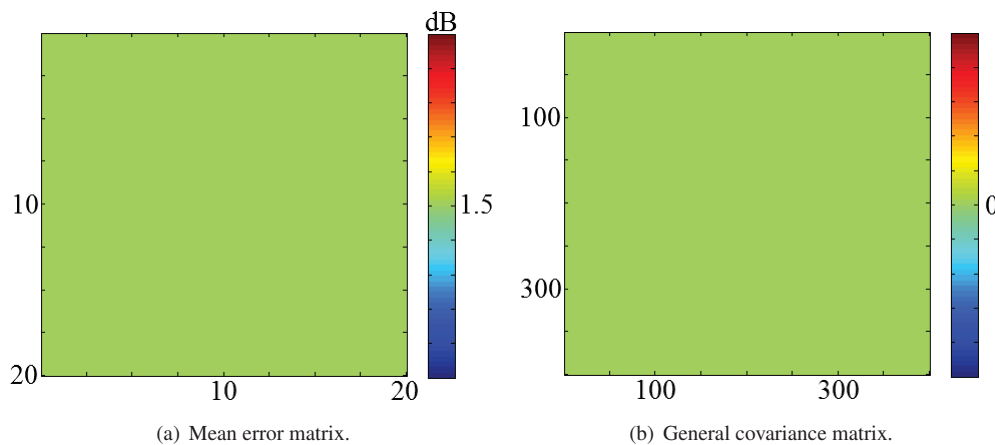


**Figure 5.1:** Covariance matrix and mean error matrix generated from constant synthetic data with a residual of 1.5.

Both behave as expected.

The second test is with Gaussian white noise as residual error. With this test it is expected that the mean error matrix and the covariance matrix is close to zero. The mean error matrix should be close to zero since the Gaussian white noise has a mean of zero. There are three reasons why it is not zero but only close to and they are because of interpolation, the stochastic element of Gaussian white noise, and using rain intensities as weights. In figure 5.2 the mean error matrix and the covariance matrix produced from Gaussian white noise as residual error can be seen.

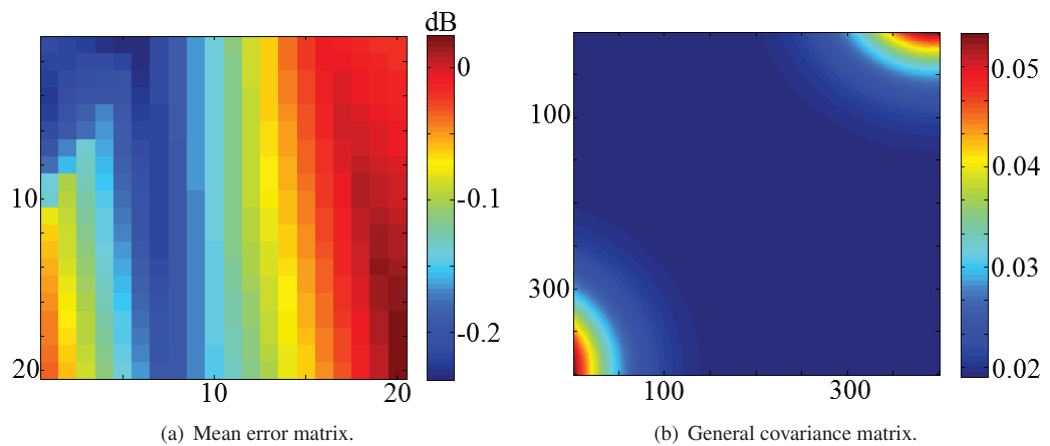


**Figure 5.2:** Covariance matrix and mean error matrix generated from synthetic Gaussian white noise residual data.

Both behave as expected.

The decomposition of the general covariance matrix is done by Cholesky factorization. To test if the Cholesky factorization is performed successfully the general covariance matrix can be reproduced by  $C_{general} = L L^T$ . In figure 5.3(b) the reproduction of the general covariance matrix can be seen compared with the general covariance matrix 5.3(a).

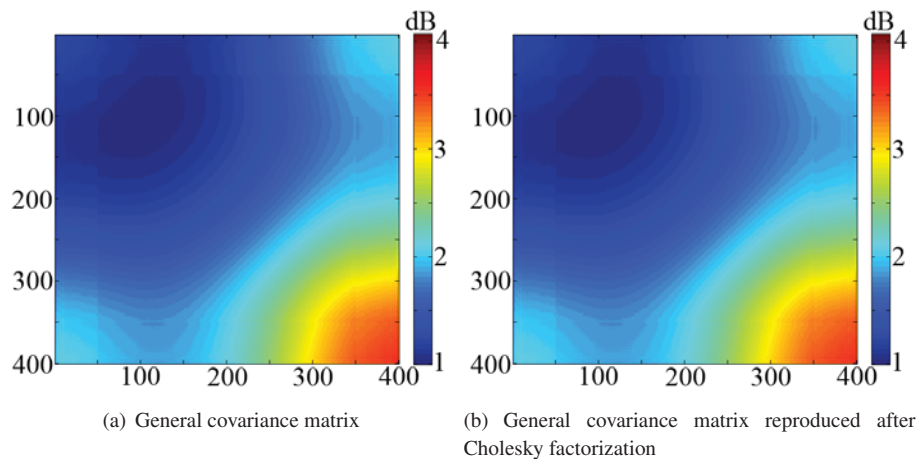


**Figure 5.3:** Visual comparison of general covariance matrix before and after Cholesky factorization.

From the visualisation it can be seen that the reproduction of the general covariance matrix after Cholesky factorization is correct.

The crucial test for the ensemble generator function is if the covariance of the perturbation gives the same general covariance matrix from which they were generated. Because of the stochastic element (Gaussian white noise) the more perturbations the more accurate is the general covariance matrix reproduced. In figure 5.4(b) the general covariance matrix is reproduced from 1000 simulated realisations and compared with the general covariance matrix in figure 5.4(a).

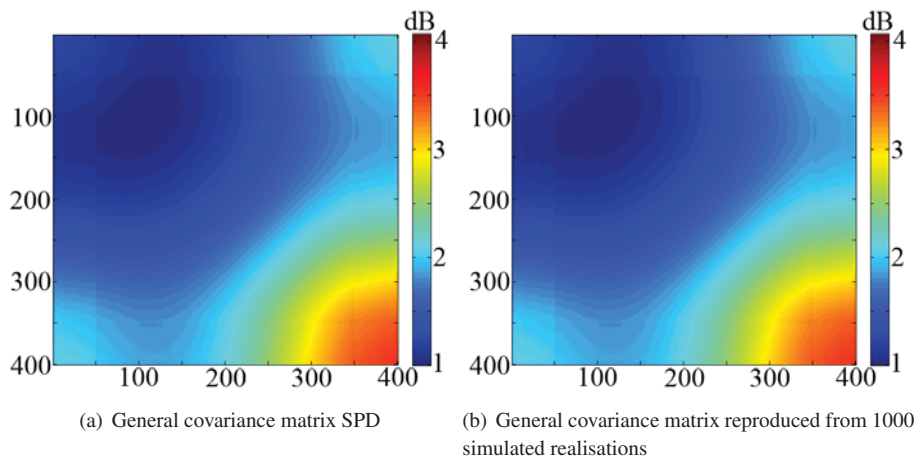


**Figure 5.4:** Visual comparison of general covariance matrix and the reproduced general covariance matrix from 1000 simulated realisations.

As it can be seen the ensemble generator are capable of reproducing the covariance matrix and hereby are the perturbation layers a correct representation of the spatial error structure expressed by the covariance matrix.

## 5.2 Examples of ensemble members and time series produced by ensemble generator

After having tested that the ensemble generator behaves as expected the next step is to actually produce the perturbations and perturb the original radar precipitation field. It has been chosen to generate 100 perturbations for each time step since the covariance matrix could be satisfactorily reproduced from 100 realisations. On that basis the error structure was accessed to be represented in the variability of the ensembles.

In figure 5.5 four different ensemble members can be seen from two different time steps. For each time step a large and small perturbation have been chosen to show. The white pixels are pixels that has an intensity less than  $0.5 \frac{\text{mm}}{\text{hr}}$  and are therefore not perturbed.

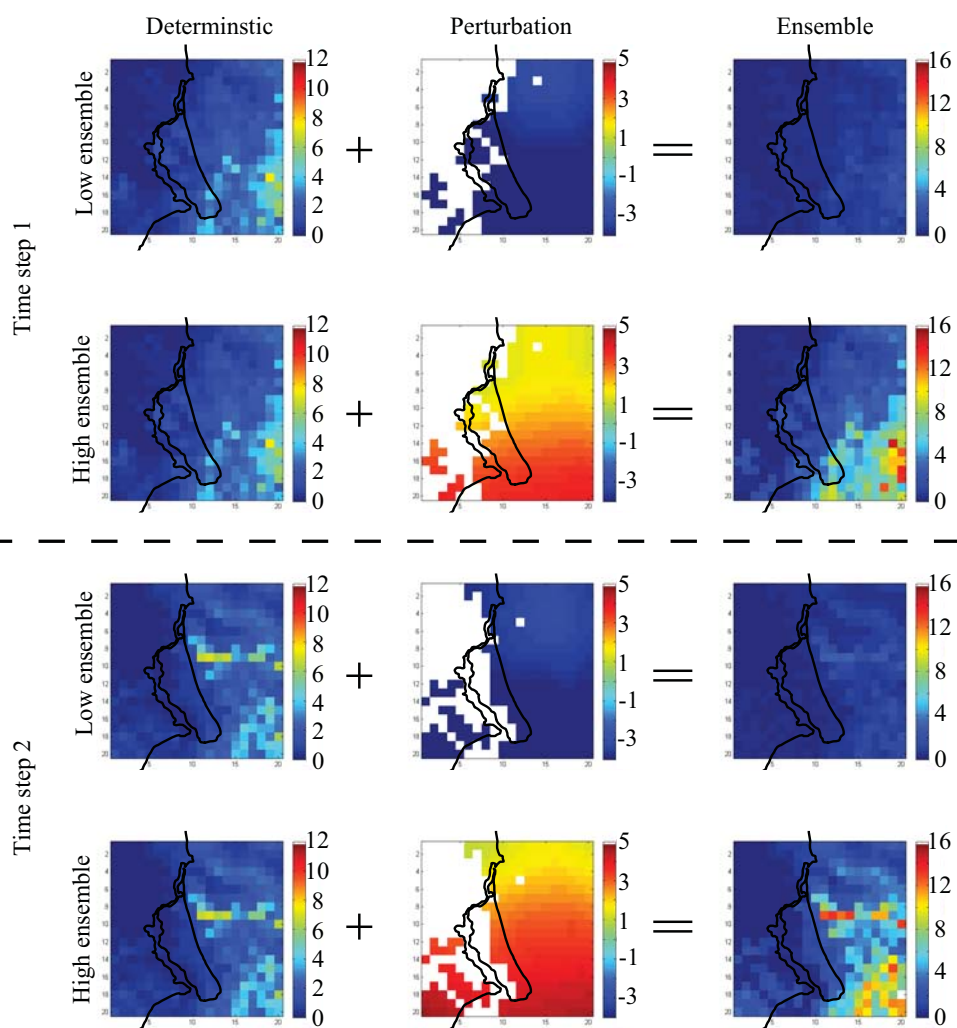


**Figure 5.5:** Example of ensemble members from two time steps. All images are in dB. White areas are pixels not perturbed.

In order to use the ensembles in the groundwater model yearly rain fall time series are needed. For each time step there have been generated 100 ensembles which means that 100 probabilistic time series is to be generated at each pixel overlaying Bribie Island.

In figure 5.6 a plot of ensembles along with non-bias corrected radar QPE (red) and bias corrected

radar QPE (black) are shown.

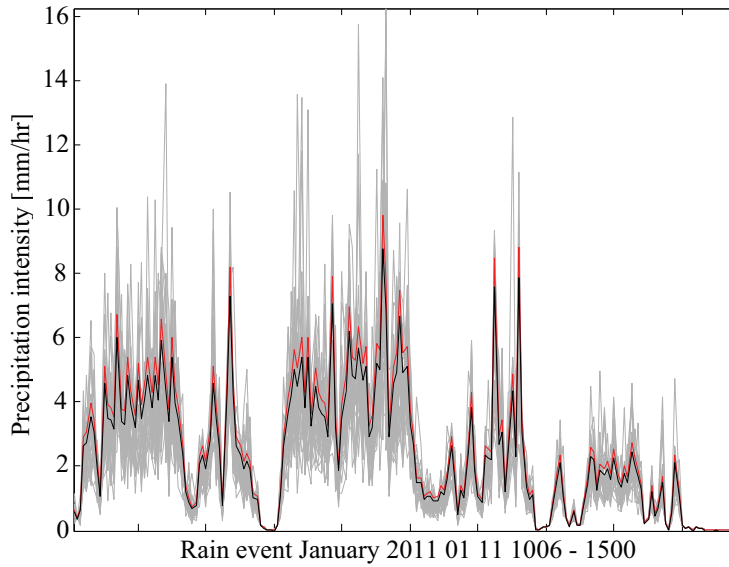


**Figure 5.6:** Non-bias corrected radar QPE (red), bias corrected radar QPE (black), and ensembles (gray) from rain event in January 2011.

The example shows that the bias corrected radar QPE has intensities lower than the non-bias corrected radar QPE. With a closer inspection it also seems that the ensembles have a tendency towards lower intensities than the bias and non-bias corrected radar QPE. To examine this a plot with the deterministic radar QPE and the mean of the ensembles can be seen in figure 5.7.

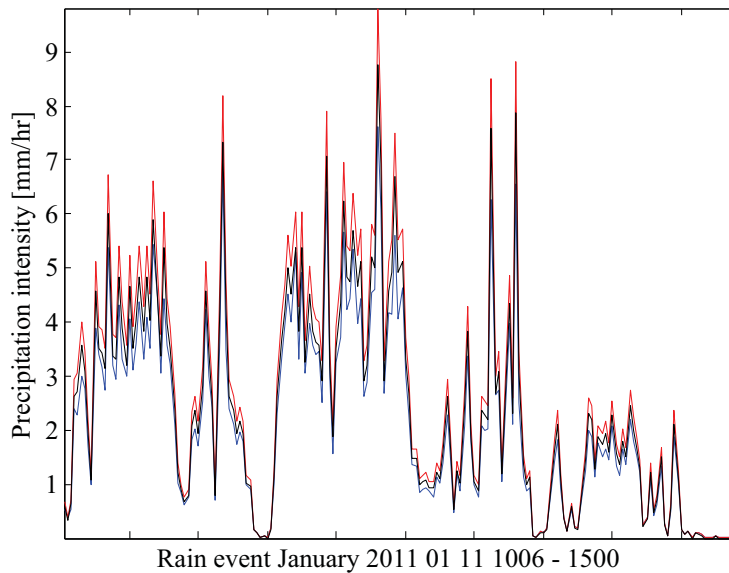


**Figure 5.7:** Non-bias corrected radar QPE (red), bias corrected radar QPE (black), and ensemble mean (blue) from rain event in January 2011.

Notice when the intensity is below  $0.5 \frac{\text{mm}}{\text{hr}}$  no perturbations have been generated which means that the ensembles is equal to the determined radar QPE. From the figure it can be seen that in average the ensembles are below both the bias and non-bias radar QPE. It was expected that the average

of the ensembles would have lower intensities than the non-bias corrected radar QPE but the bias corrected radar QPE was expected to be approximately the same. The in-built bias correction of the ensemble generator gives a slightly higher degree of correction than the normal bias correction method. The differences between the two methods are very small and the bias correction of the ensemble generator is assessed to be working. Reasons for the discrepancy can be the way that the mean error matrix has been estimated through interpolation, number of realisations, and the very different nature of the two methods.

To examine the variability of the ensembles the standard deviation are found and can be seen as the grey filled area in figure 5.8.

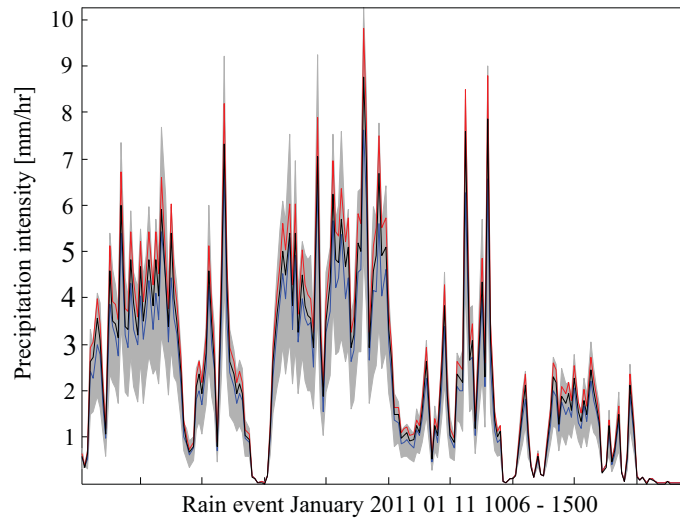


**Figure 5.8:** Standard deviation interval of 1 time spread corresponds to approximately 68% confidence interval (filled grey area), non-bias corrected radar QPE (red), bias corrected radar QPE (black), and ensemble mean (blue) from rain event in January 2011.

From the figure it can be seen that the standard deviation increases with intensity. This is a good property of the ensemble generator since the uncertainty also increases with increasing intensities.

For a groundwater model the amount of rain is more important than rapid changes in intensity because of the slow response time in groundwater levels. Therefore in figure 5.9 are the ensembles and the radar QPE, from both bias corrected and non-bias corrected, accumulated from May 2010 to May 2011.

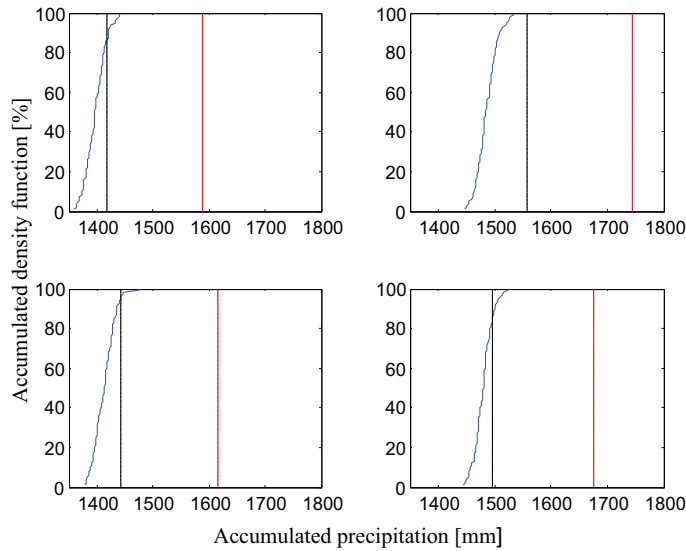


**Figure 5.9:** Sorted accumulated rain fall intensities for ensembles (blue), accumulated non-bias corrected radar QPE (red), and accumulated bias corrected (black) in four random pixel overlaying Bribie Island.

The accumulated plots shows again that in term of water amounts the ensembles in general are lower than the accumulated non-bias corrected radar QPE. The accumulated bias corrected radar QPE on the other hand shows more similar results than the ensembles. If the two methods of bias corrections was consistent the bias corrected radar QPE should be directly in the middle of the sorted accumulated ensembles. As seen this is not completely the case since it lies in the upper end of the accumulated ensembles.

To investigate the difference in water amounts of the ensembles a histogram depicting the standard deviation of the ensembles can be seen in figure 5.10.

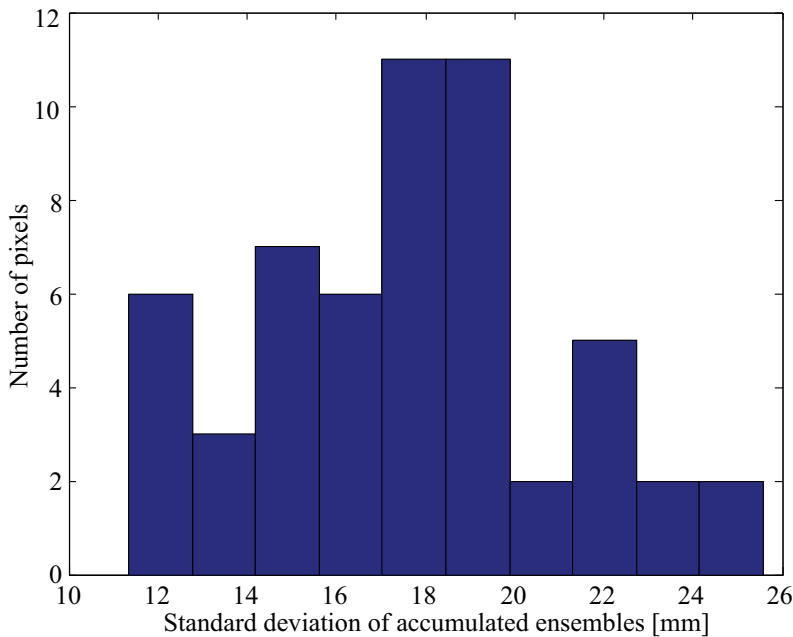


**Figure 5.10:** The standard deviation of the accumulated ensembles in each of the 55 pixels overlaying Bribie Island.

From the histogram it can be seen that the variability of the accumulated ensembles is small (between 0.78% and 1.67% of the total accumulated amount). This could be surprising since the variability at each time step seems to induce a larger variability but over a period of time the average variability is small due to the controlled stochastic nature of the ensemble generator. If not only 55 pixels was evaluated but the entire radar precipitation field (22500 pixels) the histogram would be expected to show a normal distribution.

By evaluating all the time series in a given application the many possible combinations of the ensembles represent the uncertainties of the radar QPE. Increasing with the number of perturbations, the chances of finding the true rain fall is increasing. In order to examine the sensitivity of groundwater levels from the uncertainty in radar QPE, the next step is build a groundwater model of Bribie Island.



**PART**  
**III**

**GROUNDWATER MODEL OF BRIBIE ISLAND**



# Groundwater model of Bribie Island

In the following the construction of a groundwater model for Bribie Island is described. The purpose of the model is to investigate the models sensitivity to the uncertainties in the radar QPE. The aim of the groundwater model is therefore not to make a precise representation of the hydrological system, but to be sufficiently precise to translate the uncertainties of the rain input. Bribie Island is quiet interesting in a groundwater context since it is one of the few places where groundwater is used for drinking water purposes in Queensland. Because of this other groundwater models have previously been built of Bribie Island. The previously constructed groundwater models of Bribie Island are described in the following since some of the constructional ideas have been used in this present development and to show that a big effort have gone into mapping the water resources on Bribie Island.

## 6.1 Past model development

Isaacs and Walker [1983] (model 1), constructed a finite difference model with the purpose of estimating the drawdown due to water abstraction from the main trench and the groundwater migration from sewage disposal beds. The model was a one layer model with a constant hydraulic conductivity of 25 m/day corresponding to coarse sand. As a result of the model the sewage effluent was directed to outlets south of the golf club to limit groundwater discharge into the sea.

Werner [1998] (model 2), also developed a one layer model. Both a steady state and transient MODFLOW model were constructed. The objective of the model was to assess which effect removing the commercial pine plantations would have on Bribie Island's groundwater resources. The flow of the groundwater was conceptualised as predominantly controlled by the sea around the island. The boundary was modelled as a fixed head of 0.3 m above ADH to account for density differences between seawater and groundwater. By calibration the hydraulic conductivity was found in the range of 1-150 m/day (from fine sand to gravel). Also by calibration recharge was found to 20% and 22% for the steady state and transient model respectively. Specific yield was found to 0.128. Subsequently the model was used to assess the effect of a proposed groundwater extraction bore field in the central part of the island.

Spring [2006] (model 3), developed a 2 layer MODFLOW model. The model was constructed with an upper aquifer and a lower aquifer system. The intermediate indurated sand between the two aquifers was modelled as a vertical conductance between the two aquifers. The upper aquifer was found to 18 m/day, the lower aquifer to 0.8 m/day, and the vertical conductance was estimated to 2.5e-6 m/day. It was found that the central swale was a significant groundwater discharge feature.

EHA PTY LTD [2007] (model 4), developed a MODFLOW groundwater model with 3 layers which was based on the existing model developed by Werner 1998. The purpose of the model was to estimate the drawdown of the new bore field in the middle of the island (Banksia Beach bore field). The 3 layers were simulated as an unconfined sandy aquifer, an indurated leaky aquitard, and a confined sand aquifer. The model domain contained the middle of the island with no-flow boundaries at north and south of the bore field and with fixed head boundaries at east and west.

Jackson [2007] (model 5), produced a 4 layer MODFLOW groundwater model. The objective of this model was to incorporate the central swale and the Pacific Harbour development and therefore only the central part of the island was included in the domain. Layer 1 and 4 were modelled as the unconfined and semi-confined aquifer respectively. Layer 2 and 3 represented the indurated sand units. The delineation of the model domain was from fixed head boundaries at the ocean, tidal creeks, and lagoons.

To give a better overview and to summarize the most important aspects of the models these are gathered in table 6.1.

Experiment	Model 1	Model 2	Model 3	Model 4	Model 5
Model Type	Finite difference	MODFLOW; steady state and transient	MODFLOW; transient	MODFLOW; transient	MODFLOW; transient
Number of Layers	1	1	2	3	4
Hydraulic conductivity [ $\frac{m}{day}$ ]	25	1-150	18, 0.8	-	-
Delineation and boundaries	The whole island	The whole island (fixed head 0.3 m AHD)	The whole island	Central part of the island	Central part of the island
Other parameters	-	Recharge: 20-22%. Specific yield: 0.128	Vertical leakage coefficient of $2.5e-6$ m/day	-	-

*Table 6.1: Different aspects of the five past developed groundwater models.*

Furthermore a visualisation of the geological layers has been developed at Queensland University of Technology. Four conceptualised geological layers was visualised: an upper sandy layer, an intermediate indurated sand layer, a lower sands unit (semi-confined aquifer system), and a layer of sandy silts sitting on top of Landsborough Sandstone bedrock.

The following groundwater model is developed using the conceptualised layers of the visualisation and with the same conceptual boundaries of model 2 by Werner [1998].

## 6.2 Conceptual model

### 6.2.1 Objective of the model set-up

The aim of the groundwater model is to investigate the importance of uncertainties related to radar QPE as input in hydrological modelling. The aim of the model is therefore not to be a complete representation of Bribie Island used to quantify e.g. groundwater resources, long term influence of water abstraction, transport and spreading of pollutants etc., but to work as a test model for the ensemble time series.

### 6.2.2 Conceptual idea

The following two figures conceptualises Bribie Island Groundwater system shown as a transect, in figure 6.1 and from above, in figure 6.2.

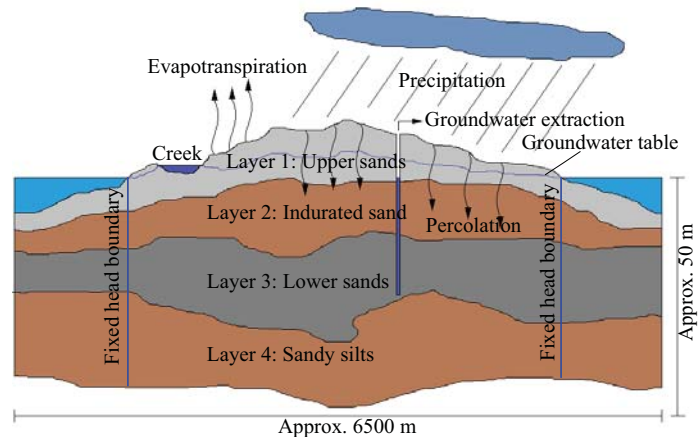


**Figure 6.1:** Transect of the conceptual model.

As it can be seen from the conceptualised transect there are four geological layers. The upper layer is the unconfined aquifer which consists of sand, underneath this layer is a layer of indurated sand which again is found in the deepest layer of the model. The main semi-confined aquifer are found inbetween the two indurated sand layer.

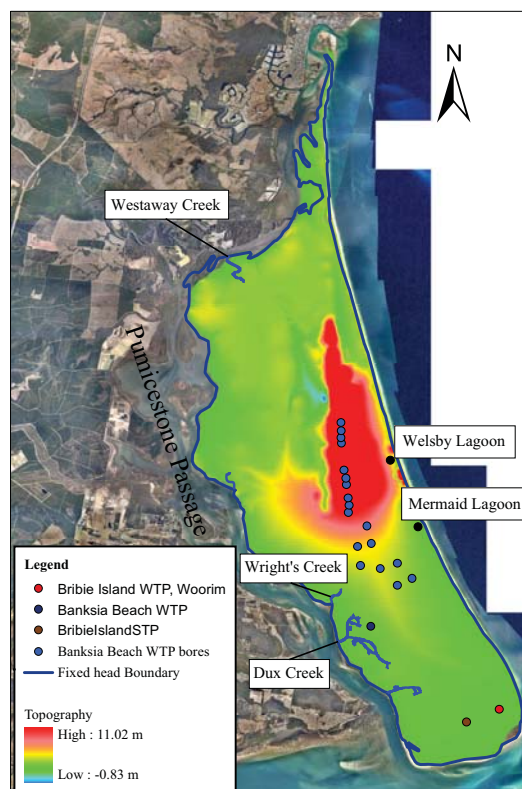


**Figure 6.2:** Conceptual model seen from above.

In general is the topography of Bribie Island flat. The maximum height is in the middle of the island with approximately 11 m AHD. The lowest point is found west of the hill in the middle of the island with approximately  $-0.80$  m AHD. The runoff happens in four main creeks and there are two lagoons in the western part of the island. In the following the different aspects of the conceptualised model are described.

### 6.2.3 Delineation of the model area

Since Bribie Island is surrounded by sea along the entire shore line, the pressure is known. The boundary condition is therefore modelled as a Dirichlet boundary. The groundwater flow is predominantly controlled by the sea which is modelled constant with a constant head of 0.2 m to account for saltwater density effects [Werner, 1998]. In figure 6.2 the boundary can be seen.

A more correct description of the boundary would be both time and spatial dependent, since tidal influences (of approximately 1 m [BoM, 2012c]), wind setup, and waves would affect the pressure at the boundary. Furthermore differences between the eastern and western side must be expected. This could be implanted if water level measurements were conducted at the eastern and western side of the Island. More about this in section 6.5: *Discussion - Difficulties making a groundwater model of Bribie Island*.

### 6.2.4 Hydrological processes

#### Water supply and sewage treatment

The water supply on Bribie Island is extracted from the groundwater. There are two water treatment plants (WTP); Banksia Beach WTP with a northern bore field (pine forest) and Bribie Island WTP (Woorim) extracting from the main trench. Banksia Beach WTP was built in 2008 and can process up to  $7.2 \cdot 10^6 \frac{\text{L}}{\text{day}}$  while the WTP in Woorim has been operational since 1962 and only treats approximately  $2.2 \cdot 10^6 \frac{\text{L}}{\text{day}}$  [Tibbetts et al., 1998].

Banksia Beach Golf Club has its own bores, which tap the same aquifer as Banksia Beach WTP. The extracted water is used for irrigation. Furthermore it has been estimated that around 1417 private spears could be extracting up to  $1.0 \cdot 10^6 \frac{\text{L}}{\text{day}}$  for irrigation on private property. There is no data for the shallow spear pumps installed on residential properties since bores under a specific depth are not required to be registered with council [Harbison, 1998].

In the south of Bribie Island sewage is directed to four infiltration ponds. Approximately  $3.9 \cdot 10^6 \frac{\text{L}}{\text{day}}$  of secondary treatment sewage infiltrates from these ponds. The idea of the infiltration is to prevent saltwater intrusion in order to work as a buffer between fresh groundwater and the saltwater interface [Tibbetts et al., 1998]. In figure 6.2 the mentioned locations can be seen.

#### Precipitation

In the period from 1977-1996 the annually average precipitation on Bribie Island is measured to 1400 mm/yr. In Beerwah Forest to the north-east and Caloundra to the north, measurements of approximately 1600 mm/year have been recorded while in the southern part of the island at Redcliffe Airport and other Redcliffe Peninsula; weather stations approximately 1250 mm/year have been recorded. This gives a difference between the northern and southern part of approximately 20 %. The wettest months are in summer and autumn. In winter long spells of dry periods are observed. In autumn the discrepancy is the largest between the northern and southern part of the Island and coincides with the period of south-easterly winds. The higher islands south-east from Bribie Island

(Moreton Island and Stradbroke Island), are likely to reduce the precipitation of the southern part of Bribie Island [Tibbetts et al., 1998]. The location of Moreton Island and Stradbroke Island can be seen in figure 6.3.

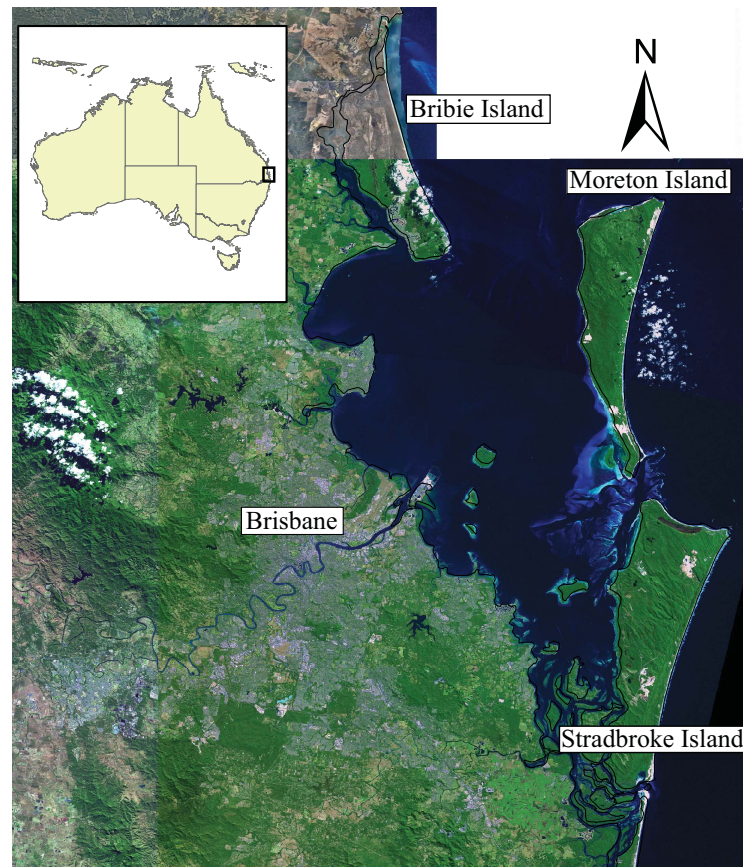


*Figure 6.3: Overview of Moreton Bay area.*

As already described the purpose of the model is to translate uncertainties from the radar QPE and the spatial variability of the rainfall, therefore the precipitation input in the groundwater model will vary. The calibration will be conducted with a constant precipitation rate divided in a northern and southern polygon with 1600 mm/year and 1250 mm/year respectively.

### **Evapotranspiration**

The annual pan evaporation in the period from 1992-1995 was 1795 mm/year with a daily variation of 1-12 mm/day. There is a definite seasonal trend with mean monthly maxima in the summer months up to 225 mm in January and minimum in July of 83 mm. [Tibbetts et al., 1998]. The potential evapotranspiration ranges from 1000 mm/year to 1300 mm/year [Jackson, 2007]. It has to be noted that measuring the evapotranspiration is highly uncertain.

### **Recharge**

The upper layer of Bribie Island is mainly unconsolidated sands and recharge is therefore a direct and quick consequence of precipitation. The response time is generally within 48 hours. The correlation between recharge and precipitation is varying and four general situations occur:

1. Recharge is well correlated with rainfall. This is typical in the southern part of the Island.
2. Recharge is poorly correlated with rainfall where the water table "under-response". This situation is found in the deeper boreholes where the sand is overlain by indurated sands.
3. Recharge is moderately correlated with rainfall where the water table "over-response". This situation is found where runoff from higher grounds is directed to lower laying grounds.
4. Recharge and rainfall are poorly correlated, but there are large hydrograph fluctuations. This occurs in areas strongly influenced by strong tidal action (near the shoreline).

Attempts to determine recharge have varied strongly from 7 % to 45 %. Most of the attempts are based on indirect calculations and measurements; water balance approaches, calibration of models, sodium mass balance calculations, and Chloride accretion measurements. The newest estimates are in the range of 7 % to 30 %. [Tibbetts et al., 1998].

### **Groundwater discharge**

Groundwater discharge happens mainly at the eastern lagoons through seepage faces and along its shoreline, especially at low tide. Furthermore there are some water holes in the southern part of Bribie Island which are mainly due to groundwater discharge. [Harbison, 1998].

### **Runoff and surface waters**

Because the top layer on Bribie Island is mainly sand the drainage system is poorly developed. The surface ponded water occurs in some drains and fire fighting ponds mainly in the pine forest. From figure 6.2 on page 73 the creeks can be seen. All the creeks draining into Pumicestone passage (see figure 6.2) reduces into a trickle during the winter months. Dux creek and the unnamed creek (in the middle of the island to the west) are the two most significant drains. On the western shoreline three brackish tannin and tidal influenced lagoons are located. These are separated from the ocean with small sand bars and can be breached by storm surges. [Tibbetts et al., 1998].

### **6.2.5 Geological model**

The geology of Bribie Island is complex and will not be discussed in detail. On Bribie Island there are two main aquifers. A shallow, perched unconfined aquifer and a deeper, basal semi-confined aquifer. A layer of less impermeable indurated sand separates these layers. Under the semi-confined aquifer a layer of undifferentiated sand and clay is present.

The geological model constructed for the present groundwater model is a four layer model. It has been created from 48 SEQwater bores which can be seen in figure 6.4.



*Figure 6.4: Location of bores used to produce geological model.*

As seen from the figure the bores are mainly located in the central part of the island. The model is therefore more accurate in the middle of the island and uncertain in the north and south. Since the purpose of the groundwater model is not to make a comprehensive representation of the groundwater system on Bribie Island the geological model reflects this. In figure 6.5. a visualisation of the geological layers can be seen. Here visualised with a offset between layers so they do not overlap.

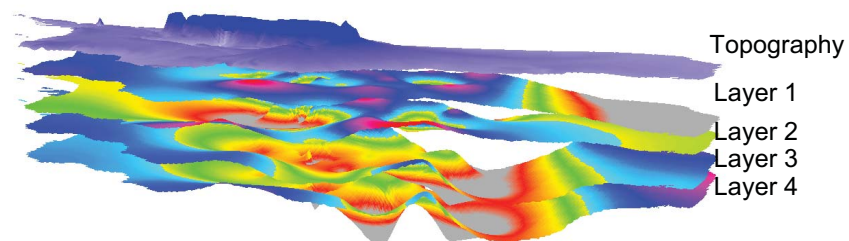


*Figure 6.5: Visualisation of the geological layers*

It can clearly be seen from figure 6.5 that the middle of the island is well represented with geological data but both north and south of the island almost no data is available hence the flat layers.

### 6.2.6 Simulation period

To investigate the spatial and temporal differences of rainfall input, the groundwater model needs to be transient. Therefore is the model simulated as a transient model of one year.

### 6.2.7 Available data for calibration and validation

The Department of Environment and Resource Management (DERM), has logged the groundwater level over a period of up to 10 years in 50 observation wells. The amount of observations per well is between 6 - 474 and an average groundwater level of each observations have been used as the reference head. The model will therefore be calibrated as if it was a steady state model since the reference for calibration is constant. In figure 6.6 the location of each observation can be seen. The observations have been clustered in four groups; A, B, C, and D.

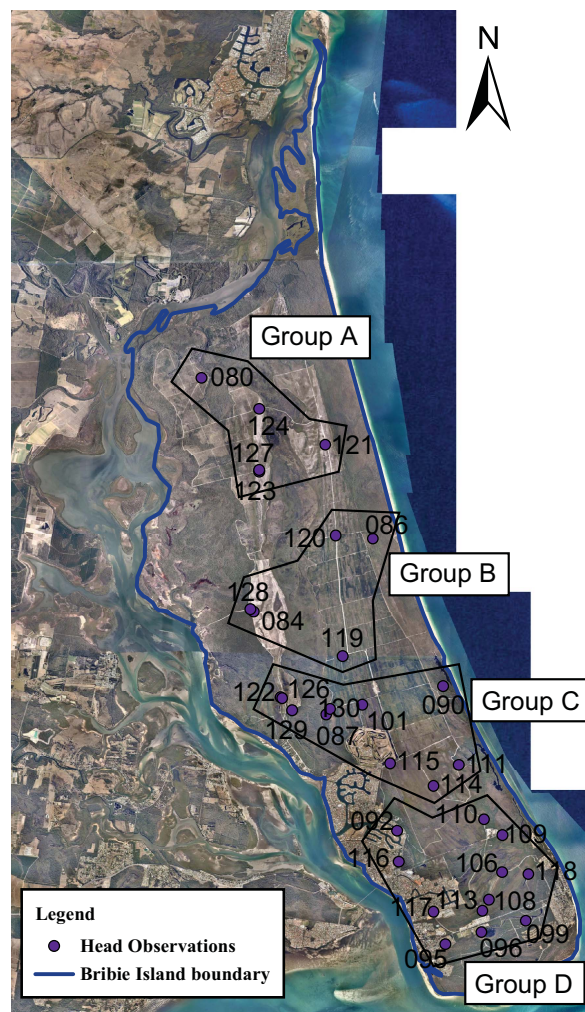


Figure 6.6: Monitoring bores used for calibration and validation of the groundwater level.

## 6.3 Numerical groundwater model

The groundwater model is constructed in Mike SHE included in the Mike Zero package developed by DHI Water & Environment. The simulation tool is based on Système Hydrologique Européen

(SHE) develop from 1977 on the blueprint of Freeze and Harlan [Abott et al., 1986]. Mike SHE is a hydrological modelling framework, including all the processes in the water cycle. See the Mike SHE user manual for details [DHI, 2011].

The numerical model is divided in sub models; evapotranspiration model, unsaturated zone model, and saturated zone model that share some overall input parameters such as simulations specifications (simulation period, time step etc.), topography, the model domain, and grid. The solution is approximated with a finite difference approach.

The model simulates one year (1980) as a transient model with a time step of 24 hours. The model domain is Bribie Island with a grid size of quadratic 250 meter cells. The topography is bilinear interpolated from a 25 meter digital elevation model (DEM).

The evapotranspiration (ET) model, estimates the sum of evaporation and plant transpiration from land surface to the atmosphere. The ET processes is being calculated in the following order:

1. Evaporation of the proportion intercepted by the vegetation canopy.
2. The rest of the water not being intercepted produces either surface water runoff or percolation to the unsaturated zone.
3. Part of the infiltrating water is evaporated from the upper part of the root zone or transpired by the plant roots.
4. The remainder of the infiltrating water recharges the groundwater in the saturated zone.

The ET model chosen is based on empirically derived equations that follow the work of Kristensen and Jensen which was carried out at the Royal Veterinary and Agriculture University of Denmark. [Kristensen and Jensen, 1975]. Since the method is based on measurements from a Danish climate which is very different from the subtropical climate of Bribie Island discrepancies can occur. Nevertheless because of the fact that the method is based on a reference evapotranspiration it is accepted. In order to apply the calculation method mentioned above the maximum root depth (RD) and leaf area index (LAI) for the plants must be known. An estimate of RD and LAI within all the polygons (area codes), seen in figure 6.7, was given by the type of land (vegetation type etc.).

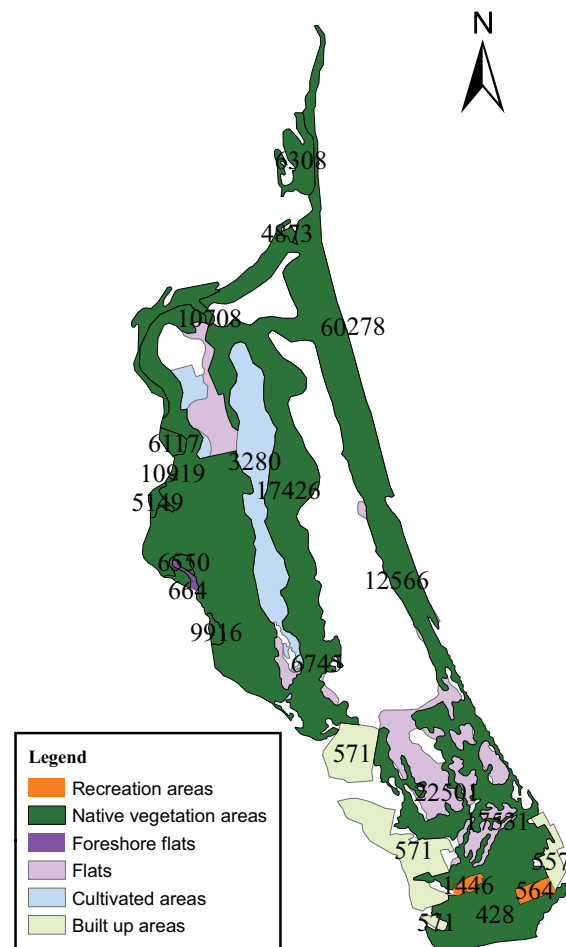


**Figure 6.7:** Type of vegetation and area code of Bribie Island.

In table 6.2 the values can be seen.

	Area code
LAI = 0.2 RD = 100 mm	557, 571
LAI = 1 RD = 500 mm	3280
LAI = 2 RD = 1000 mm	4873, 5149, 6117, 6308, 6550, 9916, 10708, 10919
LAI = 3 RD = 1000 mm	60278

**Table 6.2:** The root depth and leaf area index within the area codes.

The actual ET and the actual soil moisture status in the root zone are calculated from the reference evaporation rate specified, including the RD and LAI.

The reference ET is specified for the northern and southern part of the island to  $4 \frac{\text{mm}}{\text{day}}$  and  $4.7 \frac{\text{mm}}{\text{day}}$  respectively. This is higher than what have been measured, but for calibration reason this was found.

The unsaturated zone is the zone above the water table. The processes taking place is soil moisture from rainfall, removal from evapotranspiration, and recharge to the groundwater table. In the present groundwater model the unsaturated flow is calculated vertically by the full Richards equation (non-linear partial differential equation). When applying the Richards equation information about the soil moisture retention curve and the hydraulic conductivity function is required. Because of strong non-

linearity of the soil moisture retention curve and the hydraulic conductivity function the Richards equation cannot be solved analytical, therefore the finite difference method is used to approximate the continuous differential equation. The numerical grid applied is very fine at the top to take into account the rapid changes in saturation in response to precipitation and becomes increasingly coarse with depth se table 6.3.

From depth	To depth	Cell height	Number of cells
0	0.3	0.1	3
0.3	1.2	0.15	6
1.2	10	0.2	44

**Table 6.3:** Definition of the numerical grid used in the unsaturated zone. Total depth is 10 m.

A soil moisture retention curve for fine sand has been applied since the upper layer of Bribie Island is sandy. The retention curve has been calculated from 12 tabulated values and a spline interpolation method. In table 6.4 the essential values of the curve can be seen.

Parameter	Value
Effective saturation, $\theta_{eff}$	0.385
The suction pressure at field capacity, $pF_{fc}$	2
The suction pressure at wilting point, $pF_w$	4.2

**Table 6.4:** The values from which the retention curve has been estimated.

Since the hydraulic conductivity is a function of the moisture content a function for this is needed. The function is calculated from hydraulic conductivity function model proposed by Genuchten [1980]. From the saturated hydraulic conductivity and three empirical constants the hydraulic conductivity curve is obtained. 100 values are calculated and again a spline interpolation method is applied. In figure 6.8 the hydraulic conductivity function and the soil moisture retention curve can be seen.

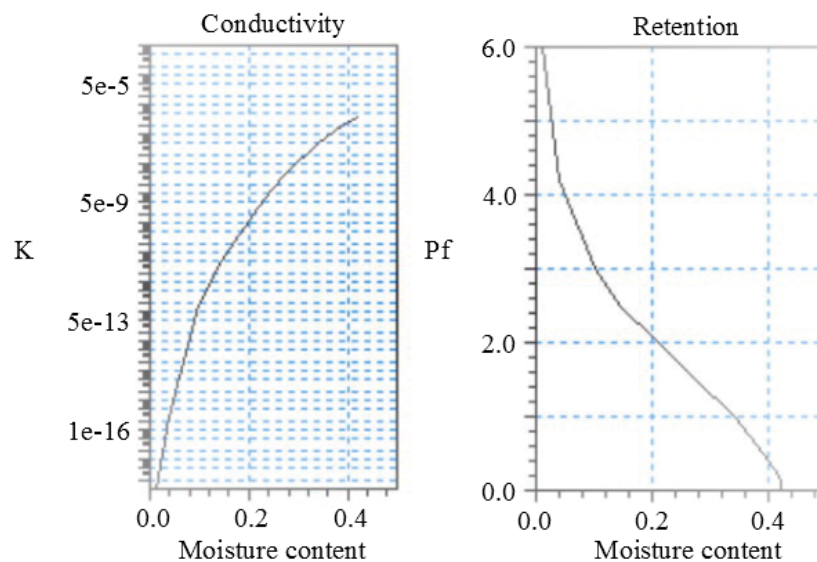


**Figure 6.8:** The hydraulic conductivity function and soil moisture retention curve of fine sand.

The saturated zone model calculates the saturated subsurface flow. The 3D Darcy equation for flow

in saturated porous media is mathematically used to describe the spatial and temporal variations in the hydraulic head and is solved numerically by an iterative implicit finite difference method. In this case the preconditioned conjugate gradient with no under-relaxations is used as solver. The saturated model requires; geological layers, initial and boundary conditions, extraction of water, and drainage. The boundaries of the layers can be seen from the preceding description of the geological model. The calibrated hydraulic parameters of the soil layers can be seen from table 6.5.

Layer	Vertical hydraulic conductivity [ $\frac{m}{s}$ ]	Horisontal hydraulic conductivity [ $\frac{m}{s}$ ]	Specific yield [-]	Specific storage [ $\frac{1}{m}$ ]	Boundary condition
Upper sands	1.0e-5	1.81e-5	30	1e-4	Fixed head 0.2 m above ADH
Indurated sands	1.074e-8	9.375e-6	15	1e-4	Fixed head 0.2 m above ADH
Lower sands (main aquifer)	1e-5	1.81e-4	25	2.13e-4	Fixed head 0.2 m above ADH
Sandy silts	1.074e-8	9.375e-6	15	1e-4	Fixed head 0.2 m above ADH

*Table 6.5: Calibrated hydraulic parameters of the four geological layers.*

Calibration of the hydraulic parameters is based on a average from investigations of the hydraulic conductivity conducted by Harbison [1998], Armstrong [2006], Lumsden [1964], Ishaq [1980], and EHA PTY LTD [2007]. The investigations is conducted using different methods such as falling head, grain size analysis, bailer test, pump test, and slug test. There are large discrepancies within the different methods and locations on the Island for the hydraulic conductivity ranging from  $0.25 \frac{m}{day}$  to  $25 \frac{m}{day}$  for sand and from  $0.07 \frac{m}{day}$  to  $2.5 \frac{m}{day}$  for indurated sand. The calibrated values is found realistic compared to actual measurements of the soil types found in Bribie Island.

Included in the model is Banksia Beach WTP production bores locations which can be seen in figure 6.2 on page 73. Data for inflow volumes at the WTP in the period from 2008-2011 is used to estimate an average pumping rate for each production bore. The average pumping rate was found to  $1.4126 \cdot 10^{-4} \frac{m^3}{s}$ . The surface drainage system is modelled as a drain level. In the catchment area of creeks the drain level is set to -0.5 m, in high topography areas -0.2 m, and in low lands below sea surface +0.4 m. The drains are not routing the water but removing it from the model.

## 6.4 Validation

The simulated and observed head along with the residual head are presented in table 6.6.

Group	Name of observation	Average observed head [m]	Simulated head (31-12-1980)	Residual head [m]
A	080	0.32	-0.163	0.478
A	121	7.13	6.816	0.311
A	123	-0.33	0.031	-0.365
A	124	-0.53	-0.041	-0.488
A	127	0.27	0.031	0.241
B	084	1.43	1.715	-0.284
B	086	3.73	3.524	0.211
B	119	4.17	3.907	0.261
B	120	7.70	6.986	0.184
B	128	0.86	1.182	-0.317
C	087	0.70	0.382	0.314
C	090	-1.17	-0.813	-0.353
C	101	0.14	0.915	-0.777
C	111	-1.10	-0.982	-0.119
C	114	-0.55	-0.403	-0.146
C	115	-0.02	0.267	-0.288
C	122	-0.26	0.260	-0.519
C	126	-0.12	0.260	-0.383
C	129	0.35	0.070	0.285
C	130	0.94	0.592	0.349
D	092	-1.51	-0.859	-0.656
D	095	-1.53	-1.100	-0.431
D	096	-1.59	-1.445	-0.149
D	099	-1.73	-1.633	-0.098
D	106	-1.12	-1.313	0.192
D	108	-1.23	-1.461	0.236
D	109	-1.26	-1.297	0.034
D	110	-1.13	-1.126	-0.007
D	113	-1.23	-1.432	0.200
D	116	-0.82	-0.795	-0.029
D	117	-1.12	-0.970	-0.145
D	118	-1.21	-1.472	0.260

**Table 6.6:** The residual head between the average observed head and the simulated head at 31-12-1980 in AHD.

Values marked with red have a difference in residual head and observed head over 0.5 m, those marked with green are within the span of  $-0.15$  m to  $0.15$  m.

It can be seen that 3 of the 5 values within group A are close to the criteria of a difference no larger than 0.5 m. The area of group A, see Figure 4 is the area where the geological model is highly uncertain because of lacking geological information.

Observation 101 in group C is having a large residual of 0.777 m. The location of the observation is

very close to the abstraction field from Banksia Beach WTP. Since the pumping rates for each bore is unknown an average calculated from the inflow at the WTP is used. Abstraction rates for each bore could be different which induces differences in the water table in its near surroundings.

Observation 122 in group C is located in an area with few geological bore and close to the beach which gives some uncertainties.

Observation 092 in group D is also poorly fitted, this could be due to the location in the built up area of Banksia Beach. The simulated value is 0.656 m higher than the observation which could indicate that a private owned residential spear could be very close and thereby lower the water table in the surroundings.

The average difference between the observed and simulated head is 0.275 m which is acceptable according to the purpose of the model being a reference for spatial variation of rain input.

In figure 6.9, three plots of the simulated head can be seen.

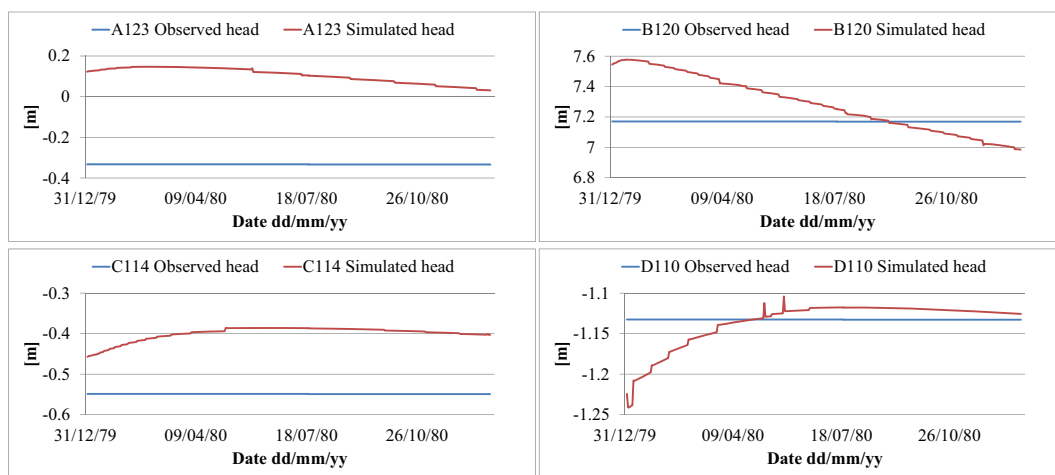


*Figure 6.9: Four plots of simulated head and constant observed value.*

From the four graphs it can be seen that the transient model is compared with steady observations so only the value at the end of December has been used for the comparison. The model needs to be transient since the spatial - and temporal variation of the rain is to be examined. The aim of the calibration was therefore to make the transient model simulated head converge towards the constant observation. This was possible for most of the observations. In observation B120, see figure 6.9, this was not possible. This could be due to wrong initial conditions.

The overall flow pattern can be seen in figure 6.10.

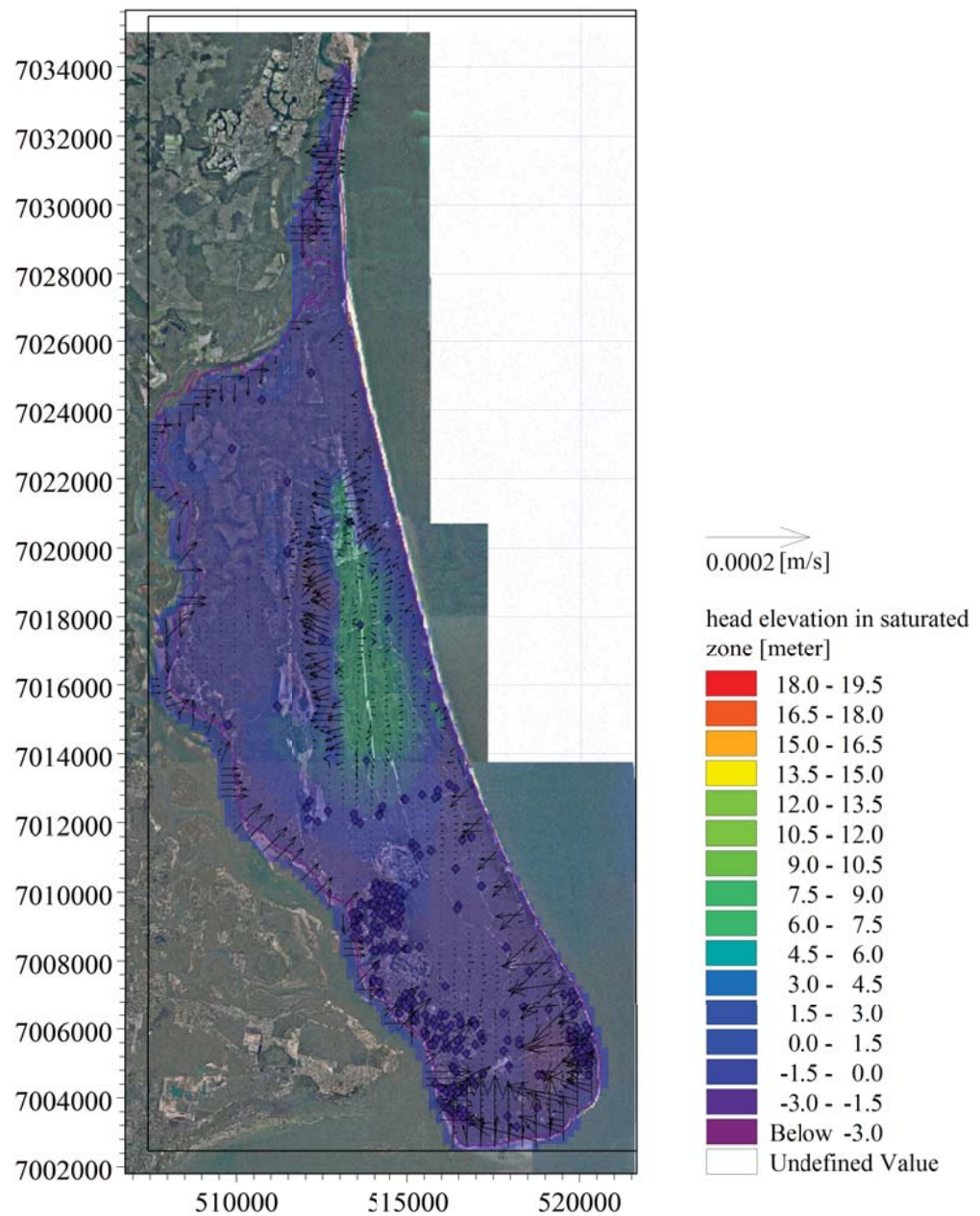


*Figure 6.10: Overall flow pattern of Bribie Island.*

As seen from the flow pattern there is an inflow along the boundary. This is due to the slightly elevated fixed head at 0.2 m.

In the middle of the island there is a flow from higher grounds to lower lying surroundings. The abstraction has little effect on the overall flow pattern, which could be due to averaged pumping rate. The model is constructed with constant inputs regarding rain fall and evapotranspiration, so the flow pattern was to be expected.

## 6.5 Discussion - Difficulties making a groundwater model of Bribie Island

Building a more accurate groundwater model and conceptual understanding of Bribie Island requires a better understanding of the hydrological system and the geological environment based on measurements.

Collecting data of all source, sinks, and abstraction data is not easy to achieve. The abstraction data from the two WTP's, located on the Island, is possible to get, but the golf clubs private spears as well as the spears used for irrigation on private property is not. This is due to no formal control and registration of abstracted amounts since it is not compulsory. If not included this could lead to an overestimation of the hydraulic conductivity and an underestimation of recharge values. In the present groundwater model only the abstraction from Banksia Beach WTP is included. Furthermore the effluent from the STP is treated in sedimentation ponds in the south of the Island. Depending on the geology this would percolate to either the unconfined or the deeper confined aquifer. This could give elevated head observations in the area and would give a different flow pattern close to the costal line. It could be included by adding a constant rain rate at the given area with a high percentage of percolation.

To understand the complexity of the geology, comprehensive field measurements would be required. The geological drillings to date conducted at the Island are very shallow and both number and depth should be increased to describe the geology more accurately. The number of geological observations used in this present study is not sufficient. From figure 6.5 on page 77 it can be seen that especially the layers of the northern part of the Island is flat and without variations which is not the case. Furthermore for example, the investigations of the hydraulic conductivity are with large discrepancies varying in result from the main aquifer (confined) within the range of 0.1 to 75 m/day. All these uncertainties make the model less trustworthy even if it validated through point measurements of observed heads. With increasing numbers of field measurements the equal-finality of the parameter set could be minimised.

The boundary condition is modelled as a fixed head boundary in level 0.2 m AHD (Australian Height Datum). The extra 0.2 m above level 0 AHD is to account for the differences in density of salt- and freshwater. This is a crude simplification of the real situation. In a real situation changes in tide would influence the boundary condition. Water level measurements would be needed to represent the boundary condition more accurate. Furthermore there would properly be a difference between the west and eastern side of the Island. This is a combination of delay in the tide on the western side of the Island, wind-setup on the eastern side, and wave action as well on the eastern side. This could properly induce a net flow from the east to west of the Island but should be examined in more detail.

Peter Nielsen investigated in 1992 the groundwater table on the two sides of the Palm Beach Isthmus, North of Sydney. Both sides are influenced by the same tide which has time mean zero. Both sides are above mean sea level (MSL) but the eastern side is approx. 0.5 m higher than the western side, and with a delay of approx. 1 day the groundwater table follows the RMS (root-mean-square) wave height [Nielsen, 1992].

The same situation could be the case at Bribie Island and it would therefore give a big difference for the boundary conditions if this is the case. If a pressure difference is present from the western side to the eastern side of the island an overall flow would run from high - to low pressure. This would change the general flow pattern of the model. Since the purpose of the model is to translate the uncertainties expressed as the ensemble time series it is accepted.

**PART**  
**IV**

**ENSEMBLES AS RAIN INPUT IN  
GROUNDWATER MODEL**



# Analysis of ground-<sup>7</sup>water model results

In this chapter the uncertainties from the radar QPE expressed as the variability of the ensembles is translated through the groundwater model. The groundwater model is calibrated using annual average precipitation in a northern and southern polygon as described in the previous chapter. The parameter set found from calibration is used onwards together with the ensembles. The purpose of this study is to investigate if radar QPE can be used in groundwater modelling and also to investigate how sensitive the groundwater model is to the uncertainties of radar QPE. In appendix G can the flow diagram of the program converting the ensemble time series into native Mike SHE formats and the flow diagram of the batch script for the stochastic modelling be seen.

In contrast to storm flooding and urban drainage models the groundwater model is a more damped environment in the sense that the system response time is much higher than the other two systems. This induce that the amount of rain is of higher importance to the groundwater level than the peak intensities. With this in mind the investigation translates the spatial distributed ensembles through the groundwater model to see how sensitive it is to radar QPE uncertainties.

For each of the 55 pixels (2000x2000 m) overlaying Bribie Island 100 time series have been created which induce that 100 groundwater model simulations has to be conducted. The 55 overlaying pixels can be seen in figure 7.1.

The result from the 100 simulations is being evaluated at the monitoring wells seen in figure 7.2. The results files are analysed in Matlab using DHI Matlab Toolbox. In figure 7.2 the simulated groundwater levels with the 100 ensembles in 8 eight monitoring wells can be seen.

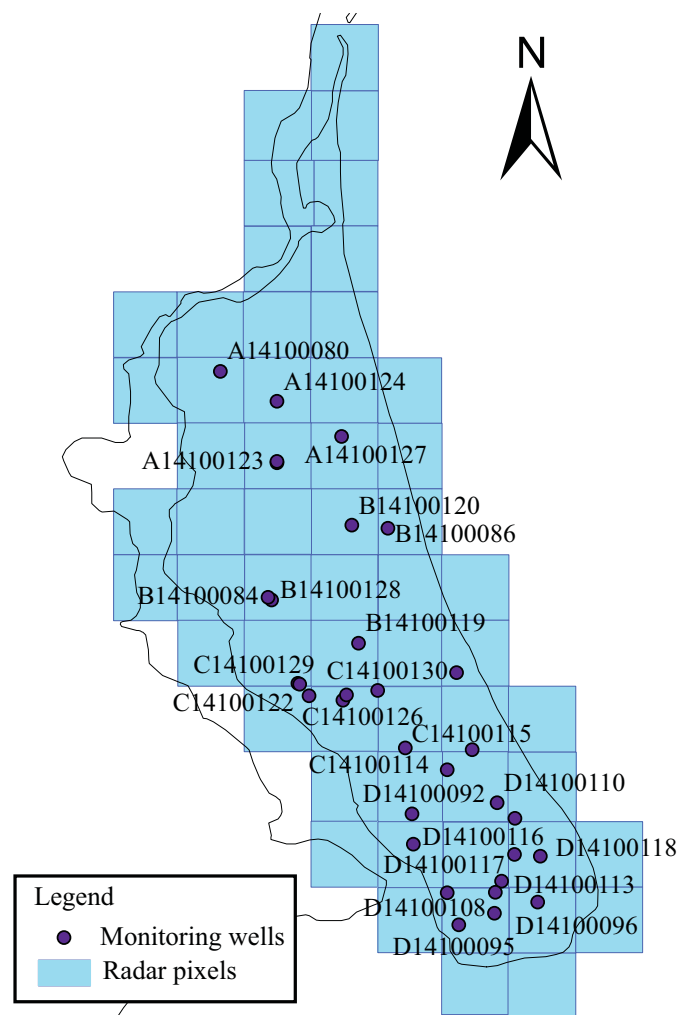


**Figure 7.1:** The spatial distribution of the 55 pixels overlaying Bribie Island and the location of the groundwater model monitoring wells.

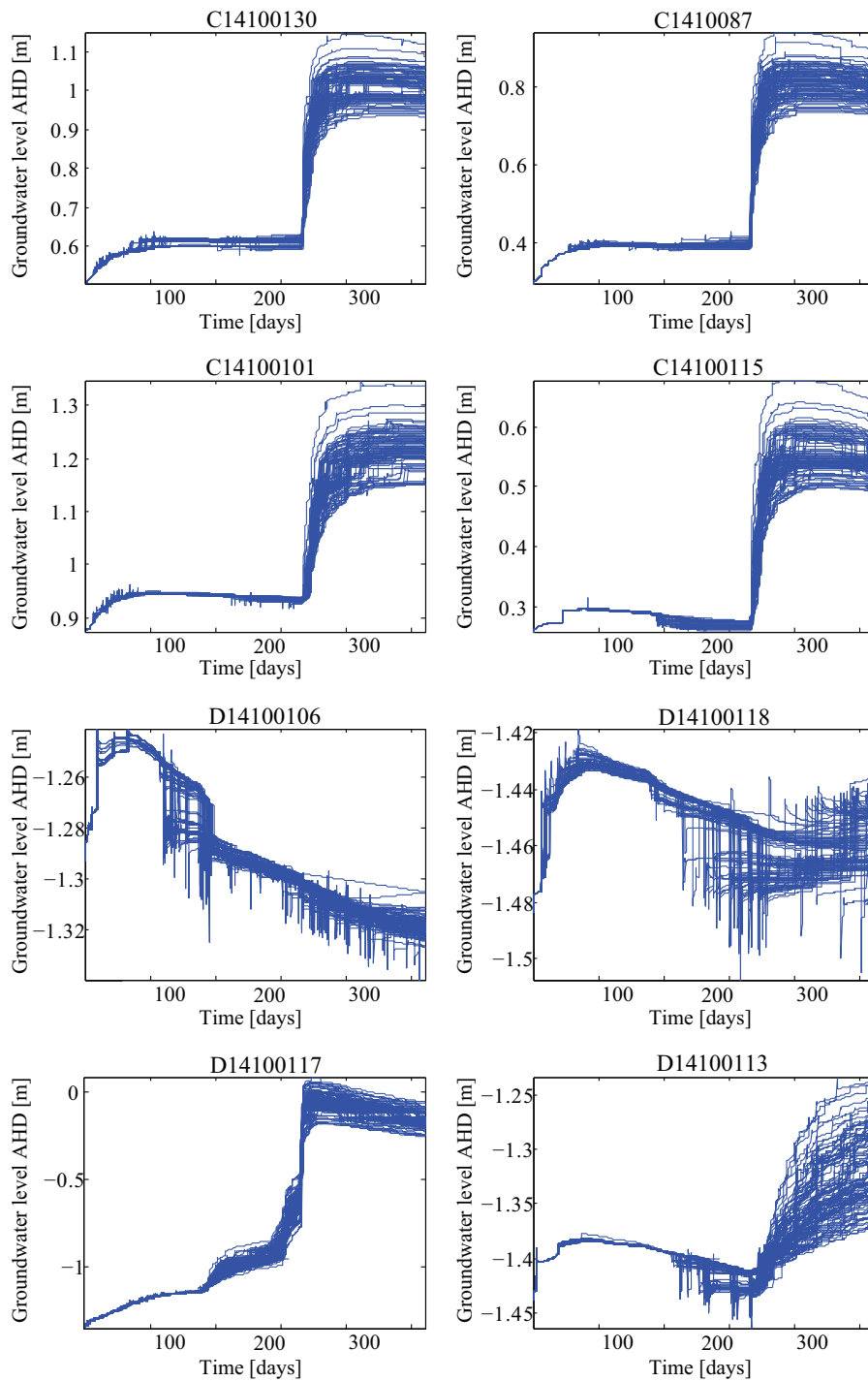


**Figure 7.2:** Example of groundwater levels for 8 monitoring wells. The blue graphs are simulated groundwater levels using ensembles as rain input.

From the graphs it can also be observed that the variability of the groundwater levels is bigger in the wet season than in the dry season. This is confirmed by plotting the standard deviation in figure 7.3.

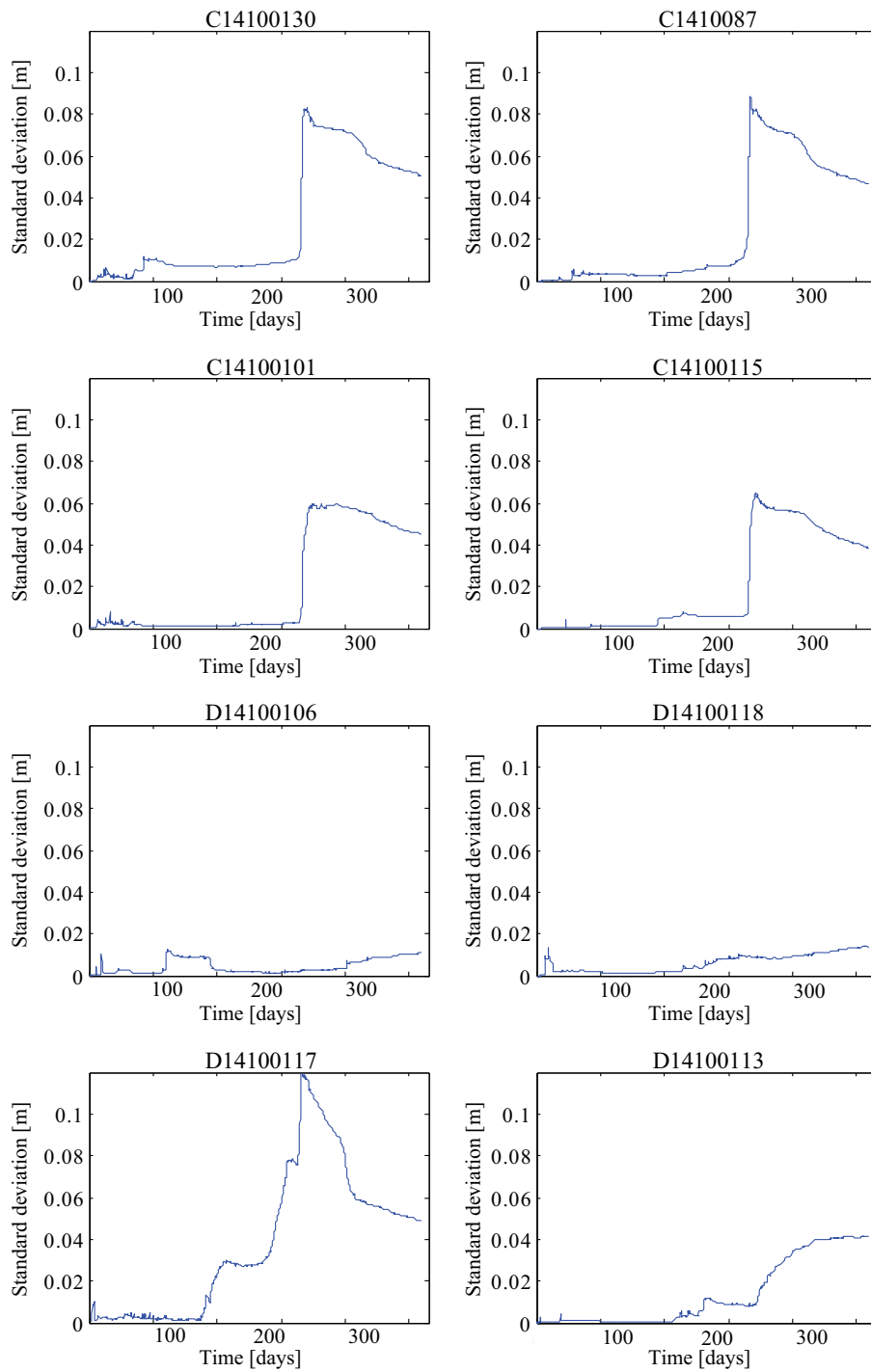


**Figure 7.3:** Standard deviation for the groundwater levels in the selected monitoring wells for 100 ensembles.

The tendency is that the standard deviation peaks in the beginning of the rain season, this is also the period with most rain. This can be observed in all the plots in figure 7.3. This is expected since when there is no rain or rain under  $0.5 \frac{\text{mm}}{\text{hr}}$  no ensembles is generated hence the ensemble time series are the same. With rain intensities over  $0.5 \frac{\text{mm}}{\text{hr}}$  ensembles are produced which gives different rain inputs for the groundwater model. With more rain (over a period of time) a bigger difference in the in the results, which is the case in the beginning of the rain season. Another factor is that with low

---

intensities even over the threshold of  $0.5 \frac{\text{mm}}{\text{hr}}$  a smaller fraction actually reaches the groundwater due to evapotranspiration.

In figure 7.4 is the mean of the 55 pixels standard deviations from the ensembles. The mean of the standard deviations have been sorted and only values above 0.1 mm are shown in the graph. It can be seen that the variability in the input goes up to a mean of 16 mm precipitation. When looking at the standard deviation of the ensembles (rain input) and the groundwater levels (output) it can be seen that it is larger on the input side than on the output. This is because the groundwater model is a system that dampens out the difference since the response time is in the range of hours compared to the rain which are in the range of minutes.

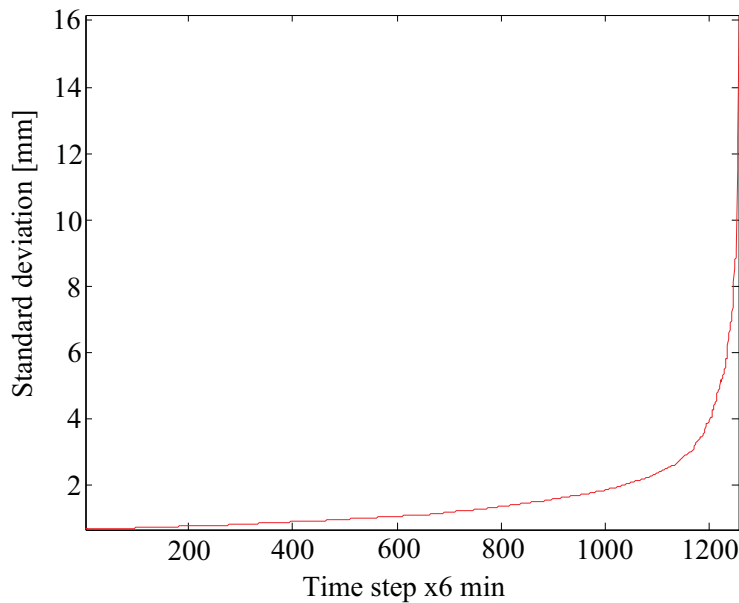


**Figure 7.4:** Sorted mean of standard deviation from ensembles in 55 pixels. (Only mean standard deviations values over 0.1 can be seen in the graph.)

The variability in simulated groundwater levels using the ensembles as rain input varies from less than 0.01 m to approximately 0.2 m with a tendency of having the largest variability in the southern monitoring wells. In general the sensitivity of the groundwater model, due to the uncertainty in radar QPE, is small which is because the long response time of the groundwater model. If a larger number of ensembles would have been used to generate the ensemble time series a larger variability in some time steps is to be expected. When that's said the variability would only vary with a small margin and it is assessed that this would not have made a difference in the output from the groundwater levels. As mentioned before the error covariance matrix can be sufficiently reproduced from 100 ensembles and therefore assessed to cover the variability of the uncertainty in radar QPE.

Compared to the many other uncertainties of the groundwater model the variability in simulated groundwater levels from the uncertainty of the rain input is considered small. For example the uncertainties contained in the geological model exceed the uncertainties in the radar QPE. Also the boundary conditions, the evapotranspiration, grid size, parameters, choice of model parameters and solvers can have a big influence on the results of the groundwater model. This current study is a relative study that delimits itself from the uncertainties of the groundwater model and therefore does not look at the other sources of uncertainties.

# Discussion

The ensemble generator is developed for the specific radar, Mt. Stapylton, and site, Bribie Island. If the generator was to be setup elsewhere, some work as to be done in order to make it useable since many area specific choices have been made in this current development. When that is said it is definitely possible and relatively easy to set it up for other radars and sites if both the radar data and rain gauge data are available. The ensemble generator works as intended and seems capable of describing the uncertainties of radar QPE as the variability of the ensembles under the given assumptions. Obviously it is difficult to determine if the all of the previously described uncertainties, in *Part II: Probabilistic uncertainty estimation*, have been covered in the variability of the ensembles. The constantly changing condition and the indirect way of measuring the precipitation makes it difficult to predict and not one estimate will apply in all situations. For these reasons the probabilistic approach is a smart way to describe the uncertainties.

Building the ensemble generator for Bribie Island proved to give some challenges because of sparse precipitation information in the surroundings of the island (which would apply to all island catchments and catchments near the coast line). Because of this, assumptions have been made that have an influence on the results. One assumption is that the chosen covariance matrix was assumed to be applicable onto Bribie Island. In areas with small orographic variations it is assessed that this assumption is not critical. On the other hand in mountainous areas this would have been critical. When looking at figure 5.5 on page 63 it can be seen that the spatial structure of the ensemble is close to the deterministic one. This is due to the relative small spatial differences in the covariance matrix. If the covariance matrix had big structural variations it would influence the structure of the ensembles more. This also vindicates that a general covariance matrix in areas with small orographic variations is applicable to produce ensembles within the precipitation range of the radar.

Using the ensembles in groundwater modelling is possible but the sensitivity measured in the variability of the groundwater model output is modest. Therefore considering the time it takes to set up the ensemble generator and producing the ensembles time series the work is not in proportion with the results in a groundwater modelling context. In urban drainage modelling and rainfall-runoff modelling this is not the case. Such systems are much more sensitive and have a low response time. Germann et al. [2009] also developed the concept of the ensemble generator for usage in the Swiss mountains as input to a rainfall-runoff model (PREVAH) used for water resources, natural hazards, and hydropower. Germann et al. [2009] finds the sensitivity of such systems to be much higher than those found in this study. Other factors that plays a role for the PREVAH model is the orographic variations, beam blockage and so on. In a Danish context usage for urban drainage modelling would be the most obvious.

Even though the results of estimating the uncertainty in radar QPE using ensembles in a groundwater context is not in proportion to the amount of work needed this study also shows that radar QPE can be used as input in groundwater modelling. This is an important result since there are many remote areas with sparse precipitation information especially in a vast continent as Australia. If the radar QPE is applicable in groundwater modelling it can also be used other hydrological modelling such as urban drainage and storm flood modelling. In these kinds of modelling with lower response times than in the groundwater model, the advantage of high spatial and temporal resolution of the radar QPE can be utilised to an higher extend than in groundwater modelling. The very high temporal resolution of precipitation input is not that important in groundwater modelling but the spatial distribution of the precipitation is an advantage in some aspects of groundwater modelling. The much more complex flow pattern can be used to better estimate spreading of contaminants and help within soil

---

remediation purposes, water extraction strategies, etc.

## Reflections

In this study the ensemble generator has been used to produce ensembles based on historical precipitation measurements data and used in a groundwater modelling context. Other application areas of the ensemble generator can be thought of.

Since the algorithm of producing the ensembles itself is very little computational there is no practical obstacles for running this part of the ensemble generator in real time. If used in real time an online estimation of the uncertainty could be obtained e.g. in form of a confidence interval on the radar QPE. This off cause is based on the assumption that an error covariance matrix can be obtained from historical data hence computed offline. However with increasing computational power and optimization of the interpolation methods to obtain the error covariance matrix this could also be achieved online. A question that rises with an online computation of the covariance matrix is how many time steps are needed to produce a meaningful error covariance matrix. This area needs further investigation if it was to be implemented.

Another and more pragmatic approach, if assumed that there is a big difference in the error structure for instance between stratiform events and convective events, is a library of error covariance matrices built up from historical data. When the radar measures rain a detection algorithm of the precipitation type could invoke the matching error covariance matrix from the archive and produce ensembles with the assumed correct error structure. Since correctly detecting the precipitation type is difficult, especially in the beginning of an event, a standard error covariance matrix could be used until detection is possible. Another way could also be distinction of rain fall intensities instead of precipitation types. The error covariance matrix could be computed from historical data and divided in a number of intervals by own choice. This way it is easy to detect which error covariance matrix is needed and the error between radar and rain gauges are likely to be intensity sensitive. Of course this also applies for the mean error matrix.

The probabilistic way of thinking is also applicable to precipitation forecasting. For numerical weather predictions (NWP) models this have been given attention by Applequist et al. [2002] and Molteni et al. [1996] in the form of output statistics and ensemble prediction systems. For nowcast predictions less attention have been given but still extensive work have been done by Bowler et al. [2006] among others. At Aalborg University a radar based nowcasting scheme based on Co-TREC Horne [2003] is held operational. For a nowcasting scheme as Co-TREC the developed ensemble generator could be added and a probabilistic nowcasting system would be obtained. This would make statistical operations possible on the nowcast output and give a more confident forecast. The Co-TREC nowcast generates radar images with lead-times up to 2 hours (depended on the radar sample time) from the last 4 obtained radar images. The idea is then to use the ensemble generator to perturb the nowcast radar images and adding a factor to the error covariance matrix increasing with lead-time (other options of increasing the variability of the ensembles with increasing lead-time could be implemented). How to obtain the factor could be as a function of time, time and intensity, time and type of precipitation, etc. Which error structure in form of the covariance matrix that should be used could, as described earlier, is taken from an archive of error covariance matrices as a function of type, intensity etc. The ensemble nowcast would yield directly applicable inputs for runoff models, hydrological modelling etc.

When the ensemble generator is so little computational in actually perturbing the radar images it could also be implemented in radar volume scans or in other words in 3D. Again the vertical and horizontal error covariance's should be computed beforehand in order to do this. The vertical error covariance matrix could be obtained by comparing with a vertical radar. The method (the LU Decomposition algorithm) would have to be modified and a higher uncertainty of the perturbations

---

incorporated. If this were to be developed applications such as storm tracking models could benefit from the statistical probability of where the storm centre and track of the storm are. Another application could be as initial conditions for larger scale models as NWP models. A 3D probabilistic nowcast could also be used as a warning system for air traffic since it is possible to predict if the storm is rising in altitude and intensity.

The next logical step is to couple the Co-TREC nowcast with the ensemble generator and in the future to create probabilistic radar based 3D nowcast.

# Conclusion

In this study processing raw radar reflectivity data into usable CAPPI images, using a probabilistic method to determine uncertainties of radar QPE, and translating these uncertainties through a groundwater model has been assessed.

Remapping the radar observations from polar to cartesian was done using the vertical and horizontal remapping method and it was achieved to program a very little computational script executing the method. A probabilistic method to describe the uncertainties having rain gauges as reference was programmed by creating perturbations of the radar precipitation field based on a known temporal correlation and spatial error structure. The uncertainty was expressed as realisations of the deterministic radar precipitation field directly applicable for runoff - or hydrological modelling. The generated ensembles had a mean less than the radar QPE since the method was applied on non-bias corrected data. The accumulated amounts of the ensembles only had a standard deviation of 0.78% to 1.67%. It was found that the method could be implemented in real time if the error covariance matrix is found offline. Furthermore it is found that the method can be used on no bias calibrated radar data and still create ensembles that lies within the expected bias calibrated area.

In order to evaluate the sensitivity in groundwater modelling due to the uncertainties in radar QPE a groundwater model was constructed in Mike SHE covering the study location of Bribie Island. The model was built with three sub models; evapotranspiration model, unsaturated zone model, and saturated zone model. The model was calibrated with a standard rain input in a northern and southern part of the island and to fit average water levels from monitoring wells. This parameter set was used with the ensemble time series as rain input.

In 55 pixels overlaying Bribie Island time series of the 100 ensembles was created and applied. The groundwater levels in monitoring wells were examined. It was found that the standard deviation on the rain inputs was bigger than the standard deviation of the groundwater levels which indicates that the groundwater model is not sensitive to the uncertainties in radar QPE. This of course also shows the applicability of radar QPE in groundwater modelling which is very relevant in vast continents as Australia where it is practical impossible to have enough rain gauges.

# Bibliography

- Abbott, M. B., Bathurst, J. C., Cunge, J. A., O'Connell, P. E. and Rasmussen, J.: 1986, *An introduction to the European Hydrological System - Système Hydrologique Européen, SHE, 2: Structure of a physically-based, distributed modelling system.*
- Anagnostou, E. N.: 2004, *A convective/stratiform precipitation classification algorithm for volume scanning weather radar observations.*
- Andrieu, H. and Creutin, J. D.: 1994, *Identification of vertical profiles of radar reflectivity for hydrological applications using an inverse method. Part I: Formulation.*
- Andrieu, H., Creutin, J. D., Delrieu, G. and Faure, D.: 1996, *Use of a weather radar for the hydrology of a mountainous area. Part I: Radar measurement interpretation.*
- Appelquist, S., Gahrs, G. E., Pfeffer, R. L. and Niu, X.-F.: 2002, *Comparison of Methodologies for Probabilistic Quantitative Precipitation Forecasting*, Geophysical Fluid Dynamics Institute and Meteorology Department, The Florida State University, Tallahassee, Florida. 789-799.
- Armstrong, T. J.: 2006, *Determination of aquifer properties and heterogeneity in a large coastal sand mass: Bribie Island, Southeast Queensland.*, Queensland University of technology (QUT). In: International Association of Hydrogeologists.
- Aydin, K., Zhao, Y. and Seliga, T. A.: 1989, *Rain induced attenuation effects on C-band dual-polarization meteorological radars.*
- Battan, L. J.: 1973, *Radar observation of the atmosphere.*
- Bellon, A., Lee, G. W., Kilambi, A. and Zawadzki, I.: 2006, *Real-Time Comparisons of VPR-Corrected Daily Rainfall Estimates with a Gauge Mesonet*, J. S. Marshall Radar Observatory, Department of Atmospheric and Oceanic Sciences, McGill University, Montreal, Quebec, Canada.
- Berenguer, M., Corral, C., Sánchez-diezma, R. and Sempere-Torres, D.: 2005, *Hydrological Validation of a Radar-Based Nowcasting Technique*, Grup de Recerca Aplicada en Hidrometeorologia, Universitat Politècnica de Catalunya, Barcelona, Spain.
- BoM: 2006, *New Doppler Radar In Queensland*, Australian Government Bureau of Meteorology, [http://www.bom.gov.au/australia/radar/about/mt\\_stapylton\\_news.shtml](http://www.bom.gov.au/australia/radar/about/mt_stapylton_news.shtml).
- BoM: 2012a, *Australian Rainfall and Surface Temperature Data*, Australian Government Bureau of Meteorology, [http://www.bom.gov.au/cgi-bin/silo/cli\\_var/area\\_timeseries.pl](http://www.bom.gov.au/cgi-bin/silo/cli_var/area_timeseries.pl).
- BoM: 2012b, *Queensland Radar Site Information*, Australian Government Bureau of Meteorology, <http://www.bom.gov.au/australia/radar/>.
- BoM: 2012c, *Tide Predictions for Queensland*, Australian Government Bureau of Meteorology, [http://www.bom.gov.au/cgi-bin/oceanography/tides/tide\\_predictions.cgi](http://www.bom.gov.au/cgi-bin/oceanography/tides/tide_predictions.cgi).

- Bowler, N. E., Pierce, C. E. and Seed, A.: 2006, *STEPS - A probabilistic precipitation forecasting scheme which merges an extrapolation nowcast with downscaled NWP*.
- Bringi, V. N., Keenan, T. D. and Chandasekar, V.: 2001, *Correcting C-Band radar reflectivity and differential reflectivity data for rain attenuation: A self consistent method with constraints*.
- Ciach, G. J.: 2002, *Local random errors in tipping-bucket rain gauge measurements*.
- Clemens, M., Peters, G., Seltmann, J. and Winkler, P.: 2006, *Time-height evolution of measured raindrop size distributions*.
- Collier, C. G.: 1999, *The impact of wind drift on the utility of very high spatial resolution radar data over urban areas*.
- Delrieu, G., Andrieu, H. and Creutin, J.-D.: 1999, *Quantification of path-integrated attenuation for X- and C-band weather radar systems operating in mediterranean heavy rain fall*.
- DHI: 2011, *MIKE SHE USER MANUAL 2011. Volume 2: Reference guide.*, DHI.
- Doelling, I. G., Joss, J. and Riedl, J.: 1997, *Systematic variations of Z-R relationships from drop size distributions measured in northern Germany during seven years*.
- Doviak, R. J. and Zrnich, D. S.: 1993, *Doppler radar and weather observations*, second edn. ISBN 0-12-221422-6.
- EHA PTY LTD: 2007, *Bribie Island North -Central Borefield*, CabWater.
- Einfalt, T., Maul-Kötter, B. and Spies, S.: 2000, *A radar data quality control scheme used in hydrology*.
- Fulton, R. A.: 1998, *WSR-88D Polar-to-HRAP Mapping*.
- Genuchten, V.: 1980, *A closed-form equation for predicting the hydraulic conductivity of unsaturated soils.* Soil Science of America Journal, vol. 44, 892-898.
- Germann, U.: 1999, *Radome attenuation – A serious limiting factor for quantitative radar measurements?*
- Germann, U., Berenguer, M., Sempere-Torres, D. and Zappa, M.: 2009, *REAL - Ensemble radar precipitation estimation for hydrology in a mountainous region*. Quarterly Journal of the Royal Meteorological Society 135: 445-456.
- Germann, U., Galli, G., Boscacci, M. and Bolliger, M.: 2006, *Radar precipitation measurement in a mountainous region*.
- Goovaerts, P.: 1997, *Geostatistics for natural resources evaluation*, Oxford university press. ISBN: 0-19-511538-4.
- Gray, W. R., Uddstrom, M. J. and Larsen, H. R.: 2001, *Radar surface rainfall estimates using a typical shape function approach to correct for the variations in the vertical profile of reflectivity*.
- Habib, E., Ciach, G. J. and Krajewski, W. F.: 2004, *Filtering-out area-point errors from radar raingauge verification samples*.
- Habib, E., Krajewski, W. F. and Kruger, A.: 2001, *Sampling errors of tipping-bucket rain gauge measurements*.
- Harbison, J. E.: 1998, *The occurrence and chemistry of groundwater on Bribie Island, a large barrier island in Moreton bay, southeast Queensland.*, Queensland University of Technology (QUT).

- Harrison, D. L., Driscoll, S. J. and Kitchen, M.: 2000, *Improving precipitation estimates from weather radar using quality control and correction techniques*.
- Holleman, I. and Beekhuis, H.: 2004, *Weather radar monitoring using the*.
- Horne, M. P. V.: 2003, *Short-Term Precipitation Nowcasting for Composite Radar Rainfall Fields*, Massachusetts Institute of Technology.
- Isaacs, L. and Walker, F.: 1983, *Groundwater model for an island aquifer: Bribie Island groundwater study*, University of Queensland.
- Ishaq, S.: 1980, *Hydrogeological reconnaissance of the southern part of Bribie Island*, Bribie Island water supply. Brisbane: Geological survey of Queensland.
- Jackson, J. M.: 2007, *Hydrogeology and groundwater flow model, central catchment of Bribie Island, South-east Queensland*, Queensland University of Technology (QUT).
- Jensen, J. B.: 2009, *Calibration and uncertainty estimation*, Aalborg University. Slideshow from lecture.
- Jorgensen, D. P., Hildebrand, P. H. and Frush, C. L.: 1983, *Feasibility test of an airborne pulse-Doppler meteorological radar*.
- Joss, J. and Waldvogel, A.: 1990, *Precipitation measurement and hydrology*. Radar in meteorology (A90-39376 17-47). Boston, MA, American Meteorological Society, 1990, p. 577-606.
- Kitchen, M. and Blackall, R. M.: 1991, *Representativeness errors in comparisons between radar and gauge measurements of rainfall*.
- Krajewski, W. F. and Gerorgakakos, K. P.: 1985, *Synthesis of radar rainfall data*. Water Resources Research, Vol. 21, No. 5, Pages 764-768.
- Kristensen, K. J. and Jensen, S. E.: 1975, *A model for estimating actual evapotranspiration from potential evapotranspiration*, Royal Veterinary and Agricultural University. Nordic Hydrology 6, pp. 170-188.
- Lack, S. A. and Fox, N. I.: 2004, *Errors in surface rainfall rates retrieved from radar due to wind drift*.
- Lee, G. W. and Zawadzki, I.: 2004a, *Variability of drop size distributions: Time-Scale dependence of the variability and its effects on rain estimation*.
- Lee, G. W. and Zawadzki, I.: 2004b, *Variability of drop size distributions: Time-scale dependence of the variability and its effects on rain estimation*.
- Lumsden, A. C.: 1964, *Brisbane: Geological Survey of Queensland*, Bribie Island water supply.
- Lyn: n.d., *Conventional radar lecture notes*.
- Marshall, J. S. and Palmer, W. M.: 1948, *The distribution of raindrops with size*, McGill University, Montreal.
- McVan: 2012, *RIMCO meteorology*, <http://www.mcvan.com/images/stories/acrobat/rim8300.pdf>.
- Mittermaier, M. P., Hogan, R. J. and Illingworth, A. J.: 2004, *Using mesoscale model winds for correcting wind drift errors in radar estimates of surface rainfall*.
- Mittermaier, M. P., Hogan, R. J. and Illingworth, A. J.: 2006, *Using mesoscale model winds for correcting wind-drift errors in radar estimates of surface rainfall*.

- Molteni, F., Buizza, R., Palmer, T. N. and Petroliagis, T.: 1996, *The ECMWF ensemble prediction system: methodology and validation*. Quarterly Journal of the Royal Meteorological Society 73-119.
- Nielsen, P.: 1992, *Groundwater Dynamics and Salinity in Coastal Barriers*, journal of coastal research p. 732-740 edn. ISBN 0749-0208.
- Pachauri, R. K. and Reisinger, A.: 2007, *Climate change 2007: Synthesis report*, Intergovernmental panel on climate change (IPCC).
- Pegram, G., Lloret, X. and Sempere-Torres, D.: 2011, *Radar rainfall: Separating signal and noise fields to generate meaningful ensembles*, Civil Engineering, University of KwaZulu-Natal, Durban, South Africa and Grup de Recerca Aplicada en Hidrometeorologia, Universitat Politècnica de Catalunya, Barcelona, Spain. Atmospheric research 100 (2011) 226-236.
- Pellarin, T., Delrieu, G., Saulnier, G.-M., Andrieu, H., Vignal, B. and Creutin, J.-D.: 2001, *Hydrologic Visibility of Weather Radar Systems Operating in Mountainous Regions: Case Study for the Ardèche Catchment (France)*, Laboratoire d'étude des Transferts en Hydrologie et Environnement, Grenoble, France.
- Peters, G., Fischer, B., Münster, H., Clemens, M. and Wagner, A.: 2005, *Profiles of raindrop size distributions as retrieved by microrain radars*.
- Peura, M., Koistinen, J. and Hohti, H.: 2006, *Quality information in processing weather radar data for varying user models*.
- Priestly, M.: 1981, *Spectral analysis and time series*, Academic Press.
- Rinehart, R. E.: 1997, *Radar for meteorologists*. Fourth Edition. ISBN: 0-9658002-1-0.
- RMI: 2012, *VPR correction*, <http://www.meteo.be/meteo/view/en/65239-Home.html>.
- Rosenfeld, D., Amitai, E. and Wolff, D. B.: 1995, *Classification of rain regimes by the three-dimensional properties of reflectivity fields*.
- Scheffer, L. R.: 2010, *Modification of negative eigenvalues to create positive definite matrices and approximation of standard errors of correlation estimates*, Centre for Genetic Improvement of Livestock Department of Animal & Poultry Science University of Guelph, Canada.
- SEACI: 2011, *The Millennium Drought and 2010/11 Floods*, South Eastern Australian Climate Initiative, [http://www.seaci.org/publications/documents/SEACI-2Reports/SEACI2\\_Factsheet2of4\\_WEB\\_110714.pdf](http://www.seaci.org/publications/documents/SEACI-2Reports/SEACI2_Factsheet2of4_WEB_110714.pdf). Factsheet 2 of 4.
- Seed, A.: 2002, *A Dynamic and Spatial Scaling Approach to Advection Forecasting*, Cooperative research centre for catchment hydrology, Bureau of Meteorology, Melbourne, Victoria, Australia.
- Seo, D. J., Breidenbach, J., Fulton, R. and Miller, D.: 2000, *Real-Time adjustment of range-dependent biases in WSR-88D rainfall estimates due to nonuniform vertical profile of reflectivity*.
- Sevruk, B.: 1995, *Adjustment of tipping-bucket precipitation gauge measurements*.
- Shahrbab, M., Walker, J. P., Wang, Q. J., Seed, A. and Steinle, P.: 2011, *Comparison of weather radar, numerical prediction and gauge-based rainfall estimates*.
- Shapiro, A., Robinson, P., Wurman, J. and Gao, J.: 2003, *Single-Doppler Velocity Retrieval with Rapid-Scan Radar Data*.

- Skolnik, M.: 1990, *Radar Handbook*, 2nd edn, <http://www.davi.ws/index.php?link=skolnik&link2=>. ISBN 0-07-057913-X.
- Soderholm, J.: 2011, *Volumetric radar scan*, The University of Queensland.
- Spring, K.: 2006, *Groundwater flow model for a large sand mass with heterogeneous media, Bribie Island, southeast Queensland.*, Queensland University of Technology (QUT).
- Steiner, M. and Smith, J. A.: 2001, *Use of three-dimensional reflectivity structure for automated detection and removal of nonprecipitation echoes in radar data.*
- Straka, J. M., Zrnic, D. S. and Ryzhkov, A. V.: 1999, *Bulk hydrometeor classification and quantification using polarimetric radar data: Synthesis of relations.*
- Strauss, R. E.: 2003, *Alternating-projections method*, Biological Sciences, Texas Tech University. Matlab-script.
- Sugier, J., du Chatelet, J. P., Roquain, P. and Smith, A.: 2002, *Detection and removal of clutter and anaprop in radar data using a statistical scheme based on echo fluctuations.*
- Tao, T. and Journel, A. G.: 1997, *Automatic Modeling of (Cross) Covariance Tables Using Fast Fourier Transform*, Department of Geological & Environmental Sciences, Stanford University, Stanford, California.
- Thorndahl, S. and Rasmussen, M. R.: 2009, *Challenges in X-band weather radar data calibration*, Aalborg University, Department of Civil Engineering.
- Tibbetts, I. R., Hall, N. J. and Dennison, W. C.: 1998, *Moreton Bay and Catchment. School of Marine Science*, The University of Queensland, Brisbane.
- Uijlenhoet, R.: 2001, *Raindrop size distributions and radar reflectivity-rain rate relationships for radar hydrology.*
- van der Heijde, P. K. M., El-Kadi, A. I. and Williams, S. A.: 1988, *Groundwater modelling: An overview and status rapport*, U.S. Environmental Protection Agency.
- Vejen, F.: 2005, *Pilotprojekt: Beregning af dynamisk korrektion af nedbør på Samsø, 1989-2003*, Danish Meteorological Institute.
- Vejen, F., Allerup, P. and Madsen, H.: 1998, *Korrektion for fejlkilder af daglige nedbørsmålinger i Danmark*, Danish Meteorological Institute.
- Velasco-Forero, C. A., Sempere-Torres, D., Cassiraga, E. F. and Gomes-hernandez, J. J.: 2008, *A non-parametric automatic blending methodology to estimate rainfall fields from rain gauge and radar data*, Grup de Recerca Aplicada en Hidrometeorologica, ETSECCPB, Universitat Politecnica de Catalunya Departamento de Ingenieria Hidraulica y Medio Ambiente, Universidad Politecnica de Valencia.
- Vignal, B., Andrieu, H. and Creutin, J. D.: 1998, *Identification of vertical profiles of reflectivity from volume scan radar data.*
- Werner, A.: 1998, *A groundwater flow model for Bribie Island Queensland.*
- Wesson, S. M. and Pegram, G. G. S.: 2004, *Radar rainfall image repair techniques.*
- Weygandt, S. S., Shapiro, A. and Droegemeier, K. K.: 2001, *Retrieval of Model Initial Fields from Single-Doppler Observations of a Supercell.*
- Zhang, J., Howard, K. and Gourley, J.: 2004, *Constructing three-dimensional multiple-radar reflectivity mosaics: Examples of convective storms and stratiform rain echoes.* Journal of Atmospheric and oceanic technology.



**PART**  
**V**  
**APPENDIX**



# Background information of A meteorological radar use

This appendix describes how a radar works and how the measured reflectivity is estimated into a precipitation intensity. It is meant as background information for the reader to understand the basic principles of how a weather radar operates and as background to understanding the description of the uncertainties related to radar QPE.

## A.1 How a radar sends and receives signals

Following section is based on [Skolnik, 1990].

Radar (Radio Detection And Ranging) is an electronic device used for multiple purposes. It was first constructed for military purposes especially for detecting echoes from airplanes. After WWII the radar proliferated and was used for a variety of purposes. The first weather radar tracked a shower on February the 20th 1941 in England [Lyn, n.d.].

Most common radars are pulsed radar systems including the radars used for meteorological purposes. It works by a transmitter sends a pulse of energy through the antenna of the radar. When the pulse hits a target some of the energy will be reflected which is being picked up by the antenna and processed through the receiver, see figure A.1.

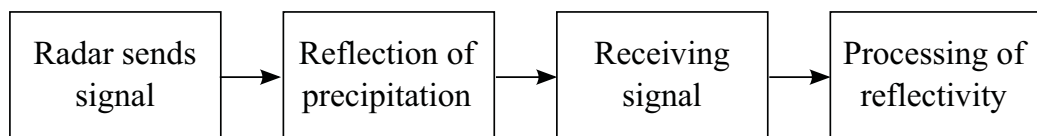


*Figure A.1: The basic principle of a pulse radar system [Skolnik, 1990, modified].*

The nature of the receiving signal provides information about the target. The distance to the target found from the time the radiated energy uses to travel to and from the target with a constant velocity. The angular location of the target from the direction of the antenna and if the target are moving its trajectory can be found from Doppler effects. Typical S-Band radar has the following overall block diagram see figure A.2.

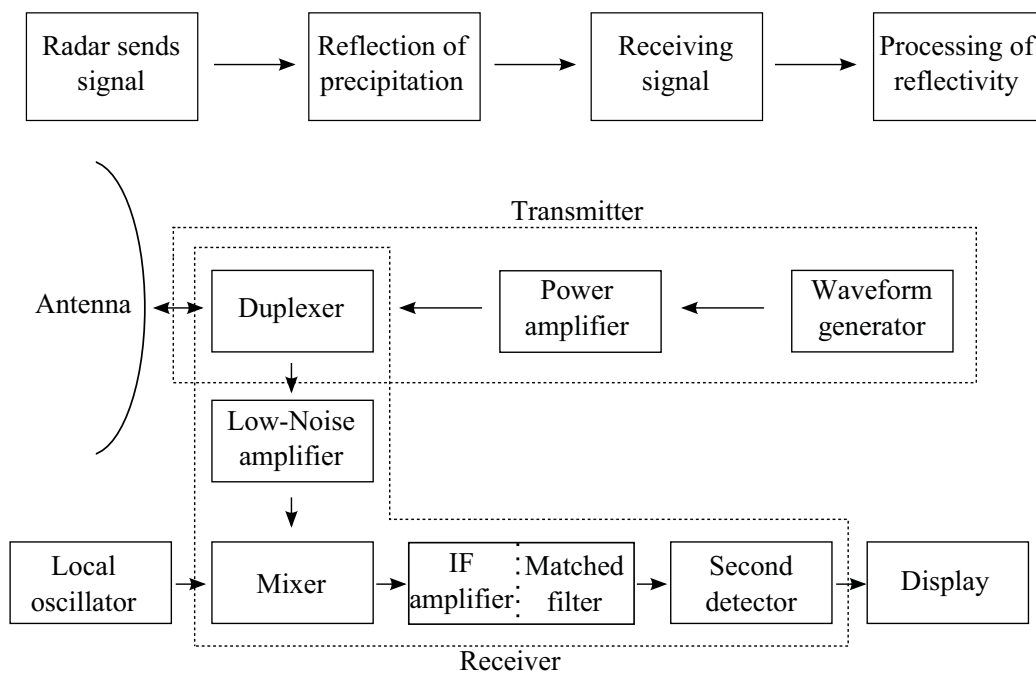


Figure A.2: Simplified block diagram of a radar [Skolnik, 1990, modified].

**The transmitter:**

The waveform generator delivers a low power input for the power amplifier. The low power input can be in a form of a repetitive "train" of short pulses or as a continuous wave (CW). The timing of the "train" principal can be seen in figure A.3.

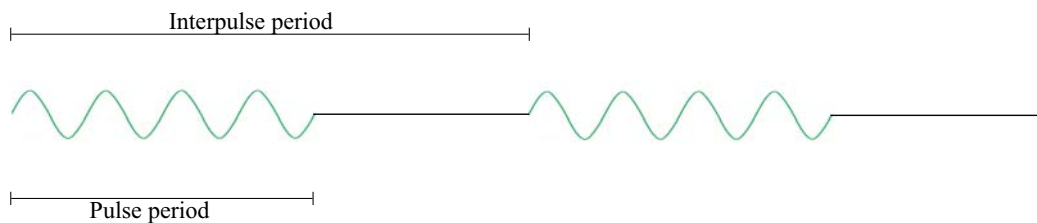


Figure A.3: Timing for sending signals.

In the pulse period a power input from the wave generator is being delivered to the power amplifier. In the interval with no input the radar is receiving signals. The frequency for how many inter-pulse periods per second is called the pulse repetition frequency (PRF).

The power amplifier of the radar is amplifying the power input from the wave generator. This can be done with different electronically equipment such as a klystron, traveling wave tube, crossed-field amplifier or solid state device. Furthermore a power oscillator as a magnetron can be used.

The duplexer is a rapid switch between transmitting and receiving signals. It works both ways it protects the receiver from the high power output from the transmitter and on reception directs the weak signal to the receiver with the transmitter turned off.

The antenna has the purpose of radiating the transmitter's power into space through a directive antenna which concentrates the energy into a narrow beam. The size of the antenna depends in part of the frequency, location, and which environment it must operate. Besides radiate the signals is also works as a receiver of the reflected signal.

**The receiver:**

The receiver gets the reflected signal from the antenna. The main purpose of the receiver is to separate the desired signal from the ever-present noise and other interfering signals and to amplify the signal sufficiently.

*The low-noise amplifier* as the front end of the receiver has the purpose to amplify the weak reflected signal. As the name implies it can only be used in areas of low background noise. For military purposes this front end receiver is omitted since it is too vulnerable to hostile jamming. In general these electronic devices are called RF amplifiers (radio frequency amplifiers).

*The mixer* translates the receiver RF signal to an intermediate frequency.

*The IF amplifier/Matched filter* has the purpose of maximising the signal to noise ratio. This is done in two steps. One is the intermediate-frequency (IF) amplifier increases the receiver signal level. Two the matched filter maximizes the output signal-to-noise ratio.

*The second detector* is a phase detector when Doppler processing is deployed otherwise an envelope detector is used. The phase detector extracts the Doppler frequency by comparison with a reference signal at the transmitted frequency. Furthermore a filter for ground clutter is included and a filter for only passing the Doppler shifted signals and hereby eliminate the signals with the same frequency as the transmitted is included.

When the reflected energy is received it has to be converted into precipitation intensities for instance if it has to be applicable in hydrology modelling.

## A.2 The radar equation in relation to meteorological radar use

This section describes the theoretical background of converting reflectivity into precipitation intensities.

The general formula to describe the returning signal when reflected from an object is the radar equation as seen in equation A.1.

$$P_r = \frac{P_t G_t}{4\pi R^2} \frac{\sigma}{4\pi R^2} A_e \quad (\text{A.1})$$

Where:

Symbol	Unit	Description
$P_r$	$W$	The received effect
$P_t$	$W$	The radar transmitted output
$G_t$	–	Radar gain
$R$	$m$	Distance to object
$\sigma$	$m^2$	The effective cross section area of object
$A_e$	$m^2$	Antenna effective aperture area

On the right hand side of the radar equation three factors is present. The first factor describes how much energy (or the power density) that hits the object when the radar radiates a power of  $P_t$  with an antenna of gain  $G_t$ . Since there is no direct correlation between a drops actual cross section area and the reflected signal (depends on the drop size and the radars wavelength) it is represented by the effective cross section area. The effective cross section area is numerator of the second factor and the denominator accounts for the divergence on the return path. The denominator in the first factor is hereby the divergence on outward path. When the signal has been returned from the object the

antennas effective aperture area  $A_e$  only intercepts a portion of the signal. The product of the three factors gives the actual received effect. Since the radar gain can be express in terms of the effective area of the antenna and the wavelength of the radar then the effective aperture area is as seen in equation A.2.

$$G_t = \frac{4\pi A_e}{\lambda^2} \Leftrightarrow A_e = \frac{G_t \lambda^2}{4\pi} \quad (\text{A.2})$$

Where:

Symbol	Unit	Description
$\lambda$	$m$	Wavelength

If equation A.2 is inserted into equation A.1 yields the normally used radar equation A.3.

$$P_r = \frac{P_t G_t^2 \lambda^2 \sigma}{(4\pi)^3 R^4} \quad (\text{A.3})$$

The only unknown in the radar equation is the effective cross section area,  $\sigma$ .

The radar equation is derived under the assumption of Rayleigh scattering. Rayleigh scatter is the change of the electromagnetic radiation direction by particles much smaller than the electromagnetic wavelength without the loss of kinetic energy (elastic scattering). For S-band radars this assumption is fulfilled, but for X-band radars with a smaller wavelength this could be unfulfilled. See table A.1 for different frequencies and wavelengths depending on the type of radar. If the assumption is not fulfilled Mie scattering would be applied.

Band	Frequency [GHz]	Wavelength [cm]	Use
L	1-2	15-20	Mobile phones, GPS, and communication satellites
S	2-4	7.5-15	Weather radars, and communication satellites
C	4-8	3.75-7.5	Weather radars, military use, and TV
X	8-12	2.5-3.75	Short range weather radar, air traffic control, and military use
K	12-18	0.5-2.5	Radar and satellite communication

*Table A.1: Frequencies and wavelengths for different types of radars.*

Under the assumption of Rayleigh scattering the Rayleigh approximation can be used ( $\alpha \ll 1$ , where  $\alpha$  is the relation between the perimeter of the object and the wavelength). The Rayleigh approximation says that a particle effective cross section area is proportional with the particle diameter powered to sixth see equation A.4.

$$\sigma = \frac{\pi^5}{\lambda^4} |K|^2 D_i^6 \quad (\text{A.4})$$

Where:

Symbol	Unit	Description
$K$	—	Refractive index
$D_i$	$m$	The diameter of the $i$ 'th drop

The refractive index is of importance since there is big difference between the states of the precipitation (for water 0.93 and ice 0.197). For weather radars the purpose it is not to measure the single raindrop but the effective cross section area of the entire volume of precipitation. So by summation

of all the drops gives equation A.5.

$$\sigma = V_m \frac{\pi^5}{\lambda^4} |K|^2 \sum_{Vol} D_i^6 = V_m \frac{\pi^5}{\lambda^4} |K|^2 Z \quad (A.5)$$

Where:

Symbol	Unit	Description
$V_m$	$m^3$	Unit volume
$Z$	$m$	Reflectivity factor (sum of all drop diameters in power of 6 in the unit volume)

Substituting equation A.5 in equation A.3 and contracting all the radar specific constants into  $C$  gives equation A.6.

$$P_r = \frac{C |K|^2 Z}{R^2} \quad (A.6)$$

The reflectivity factor depends on the drop size distribution within the unit volume. [Marshall and Palmer, 1948] found that the drop size distribution could be described by an exponential function.

$$N_D = N_0 \exp(-\Lambda D) \quad (A.7)$$

Where:

Symbol	Unit	Description
$N_D$	$cm^{-3}$	Number of raindrops with diameter $D$ in a unit volume
$N_0$	$cm^{-4}$	Empirical constant depended on the type of precipitation
$\Lambda$	$cm^{-1}$	The slope of $\log(N_D)$
$D$	$cm$	Diameter of rain drop

For a strati form precipitation [Marshall and Palmer, 1948] found that

$$N_0 = 0.08 cm^{-4}$$

for any intensity of rainfall, and that

$$\Lambda = 41 R^{-0.21} cm^{-1}$$

as a function of the rain rate,  $R[hr^{-1}]$ . For diameters less than 1.5 mm the distribution function overestimates the number of rain drops with size  $D$  in a unit volume of rain. This can be seen from figure A.4.

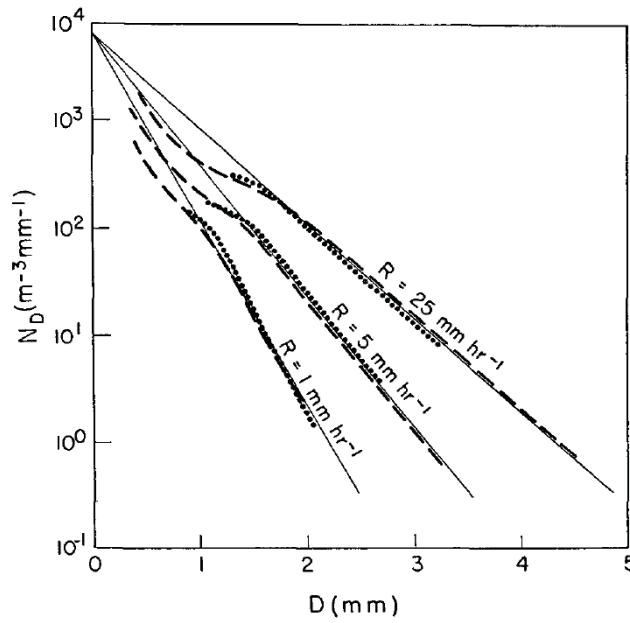


**Figure A.4:** Distribution function (solid straight lines) compared with results of Laws and Parsons (broken lines) and Ottawa observations (dotted lines). [Marshall and Palmer, 1948]

From the drop size distribution it can be seen that it is a function of the rain rate,  $R$ , and because the reflectivity,  $Z$ , is given by sum of all the rain drops diameters in power of sixth the reflectivity can be found as the sum of the drop size distribution multiplied with the drop diameter in power of sixth:

$$Z = \sum_{D_{min}}^{D_{max}} N_D(D) D^6 dD$$

Hereby is there a relation between the rain rate,  $R$ , and the reflectivity,  $Z$ . With the known reflectivity inserted in the radar equation the only unknown is the rain rate.

Many different empirical Z-R relations have been determined. These are depended on the form of precipitation, if it is stratiform or convective, as well as the geographic location. The common Z-R relation is:

$$Z = aR^b$$

Where:

Symbol	Unit	Description
a,b	–	Rain type and location dependent coefficients

The many different Z-R relationships are normal based on the above-mentioned formula with different coefficients.

# Overall flow diagram of radar data

In figure B.1 the processing of the data is shown with a flow diagram from unpacked raw radar data to ensemble time series.

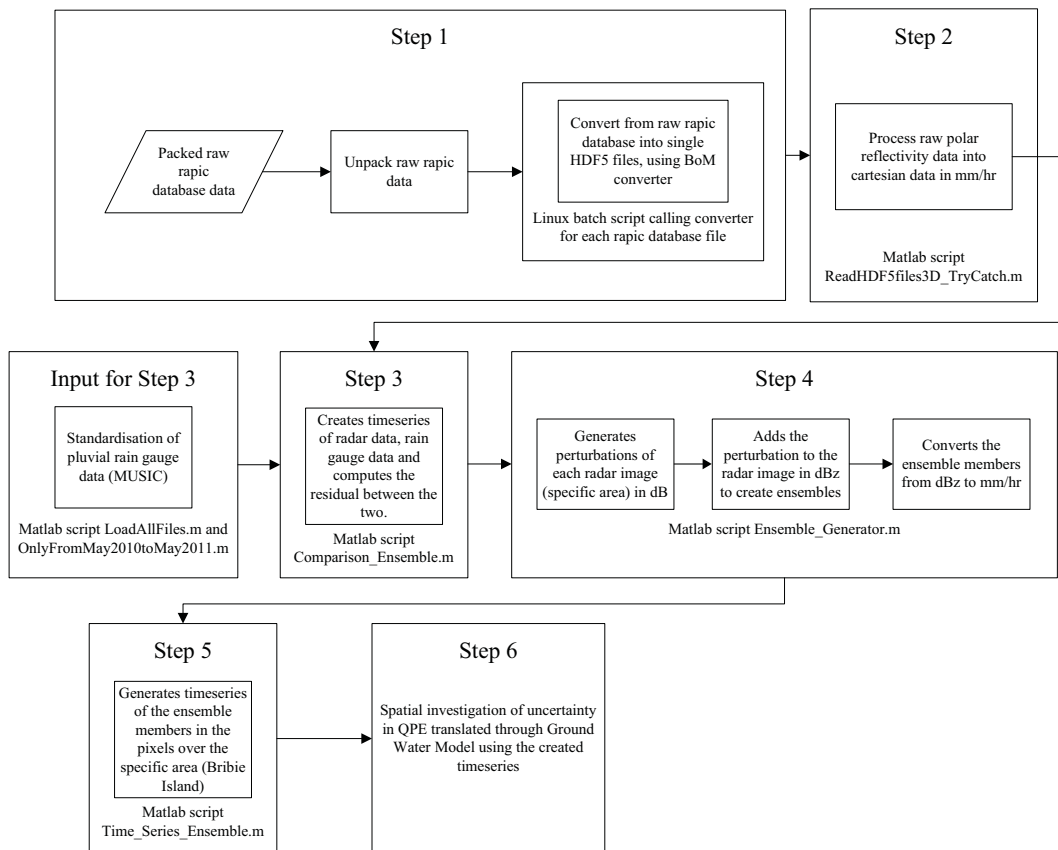


Figure B.1: Overall flow diagram.

# Flow diagram from polar to cartesian

In see figure C.1, a flow diagram from converting the raw radar data into CAPPI images can be seen.

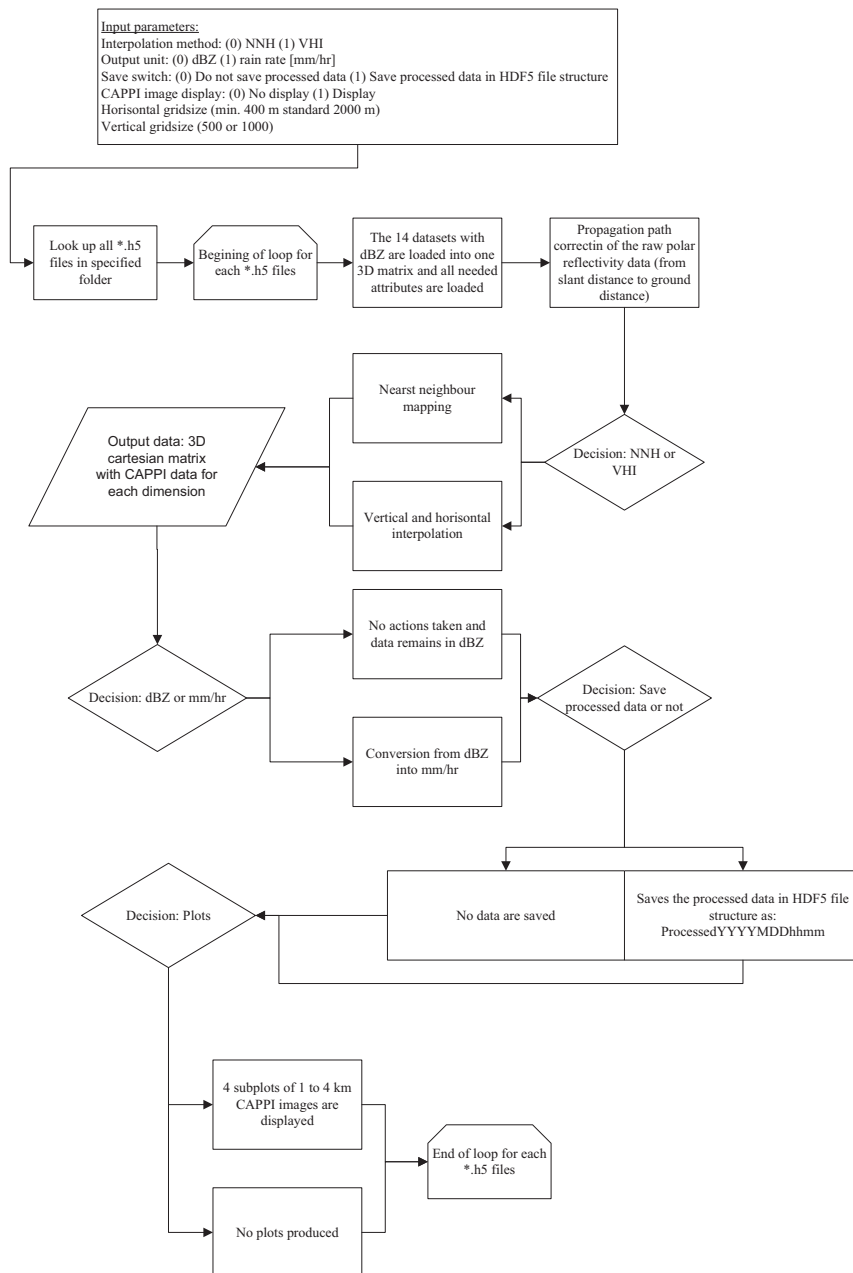
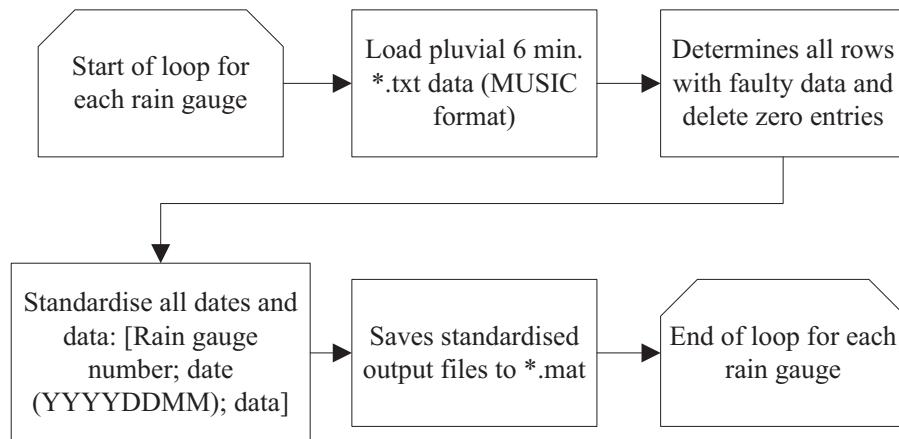


Figure C.1: Program flow diagram for converting raw polar radar data into cartesian CAPPI images.

# Processing rain gauge data

As a request to BoM all 6 min pluvial rain gauge data within the Mt. Stapylton radar was acquired. The data was formatted for the urban storm water software, MUSIC v5 by eWater in tabulated .txt file formats. Processing the data for usages in uncertainty estimation of radar QPE as ground reference, included a standardised setup of the data. A program with this purpose was programmed in Matlab.

The data format of MUSIC has a date structure which falls into four different categories depending on how many digits in the date. This was to be standardised and all data with wrong faulty rain registration deleted. Matlab script *Standardisation.m* was written for this purpose and its flow diagram can be seen in figure D.1.



**Figure D.1:** Flow diagram for pre-processing of the data files.

In figure D.2 examples of the measurement by rain gauge 40014 are seen. The top two plots are daily accumulated [mm/day] rain from year 2007 -2008 and 2008 - 2009. The bottom two plots are intensity plots in [mm/min] from 2008-06-02 and 2008-07-08.

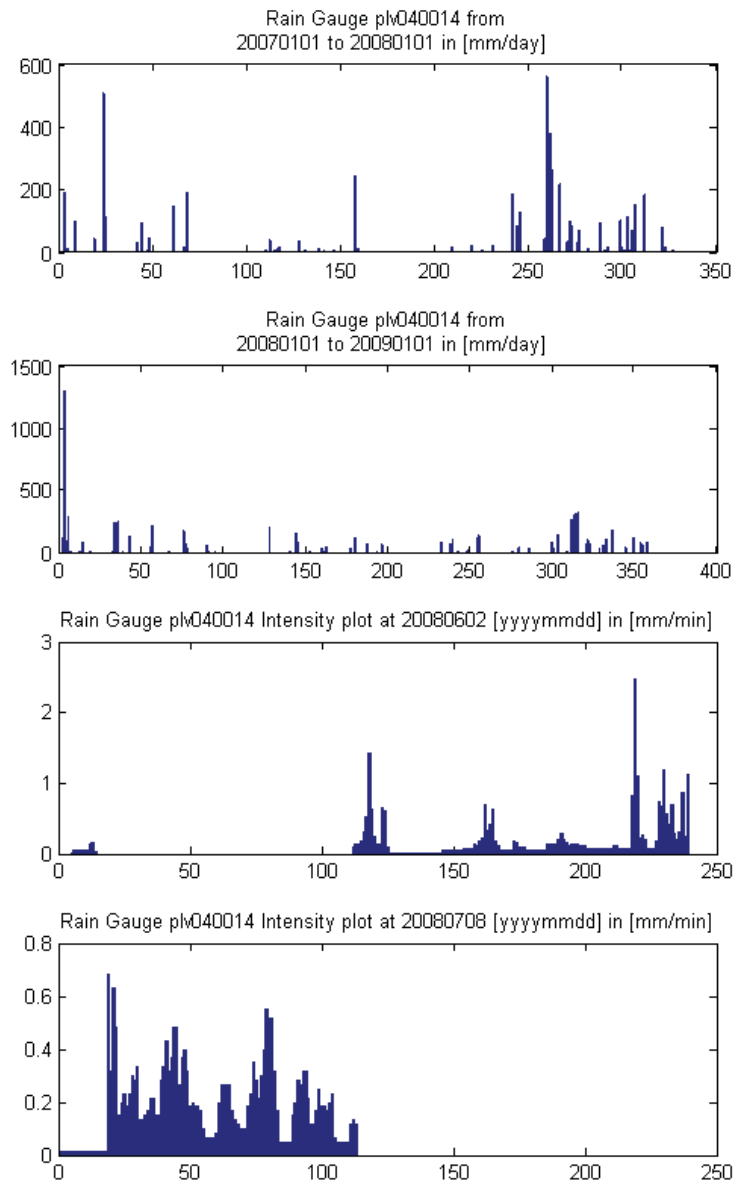


**Figure D.2:** Example of accumulated - and intensity plots of rainfall measured with rain gauge plv040014. The x-axis is days from 1st of January and min x 6 respectively.

As a last step the time period from May 2010 to May 2011 is extracted. This ensures that the comparison between radar and rain gauges can be done quickly since less data has to be searched.

# Flow diagram of residuals between radar and rain gauge

In figure E.1 can the flow diagram from producing comparison time series between radar and rain gauges be seen.

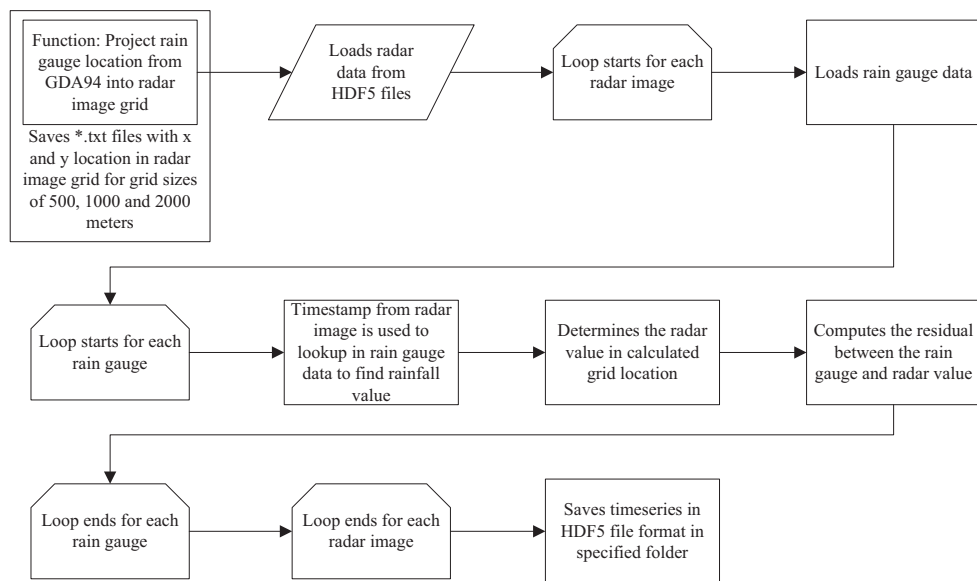


*Figure E.1: Flow diagram for comparison between radar and rain gauge values.*

# Flow diagrams **F** of ensemble generator

The Ensemble Generators (EG) methodology is implemented with the EG script which are divided into three main functions. Function 1 computes the mean error matrix, the parameters used for AR(2) modelling, and the error covariance matrix. Function 2 manipulates the error covariance matrix into a symmetric positive definite matrix and produces the lower triangular matrix by Cholesky factorization. Function 3 computes the perturbations and ensembles. The overall flow diagram for the EG script can be seen in figure F.1.

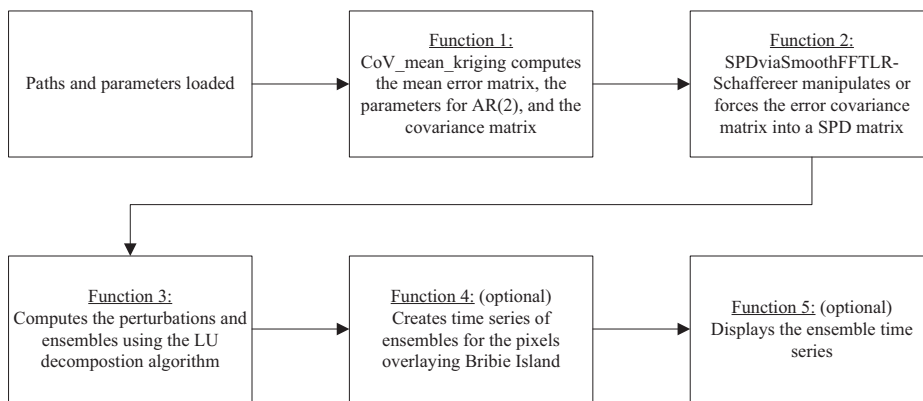


**Figure F.1:** Overall flow diagram of the EG script.

## EG script function 1

Function 1 is the preliminary computations for the LU decomposition algorithm. The flow of the function can be seen in figure F.2.

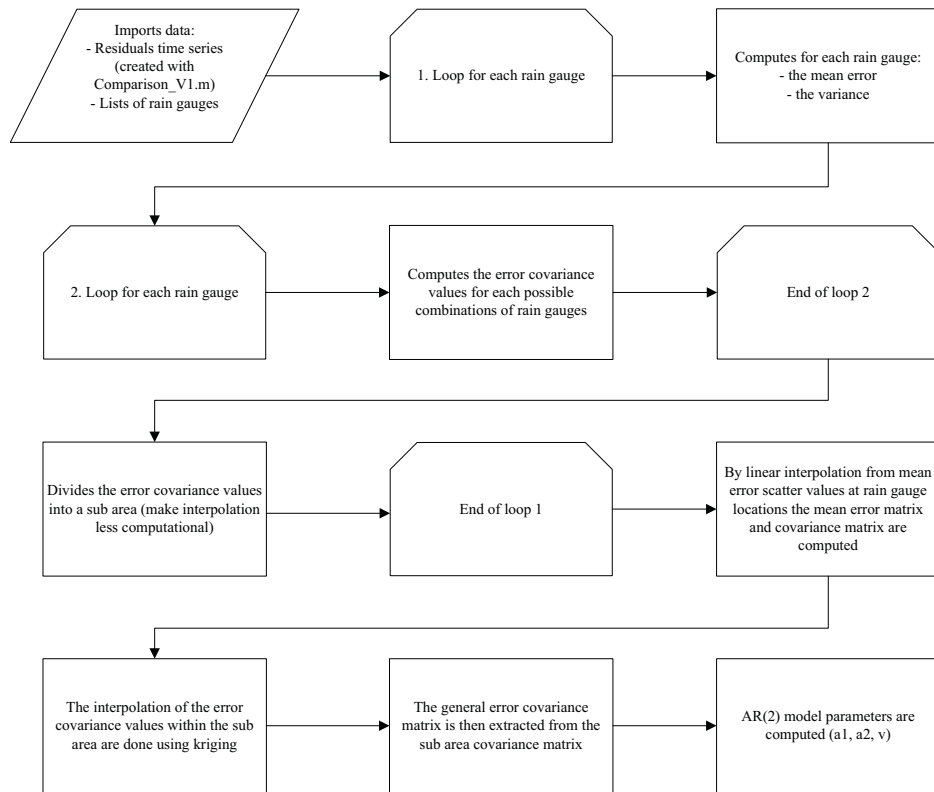


Figure F.2: Flow diagram of function 1 in EG script.

## EG script function 2

Function 2 ensures the symmetry and positive definite properties of the covariance matrix. The flow diagram can be seen in figure F.3.

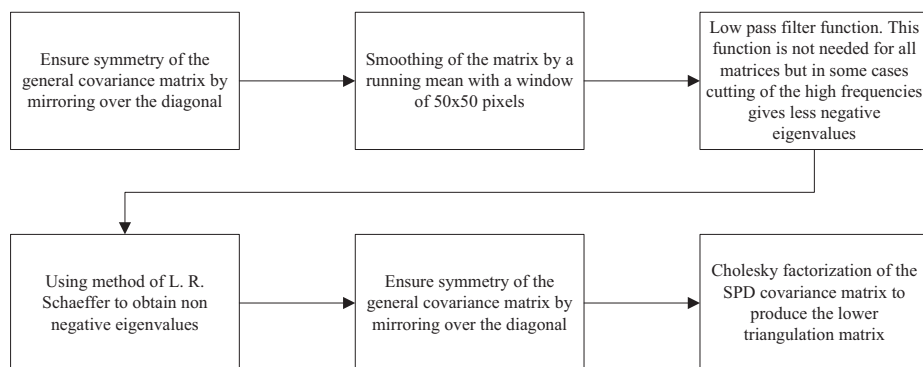


Figure F.3: Flow diagram of function 2 in EG script.

### EG script function 3

The last function of the program is the actual ensemble generator. This function runs the LU decomposition algorithm. In figure F.4 the flow diagram of the function can be seen.

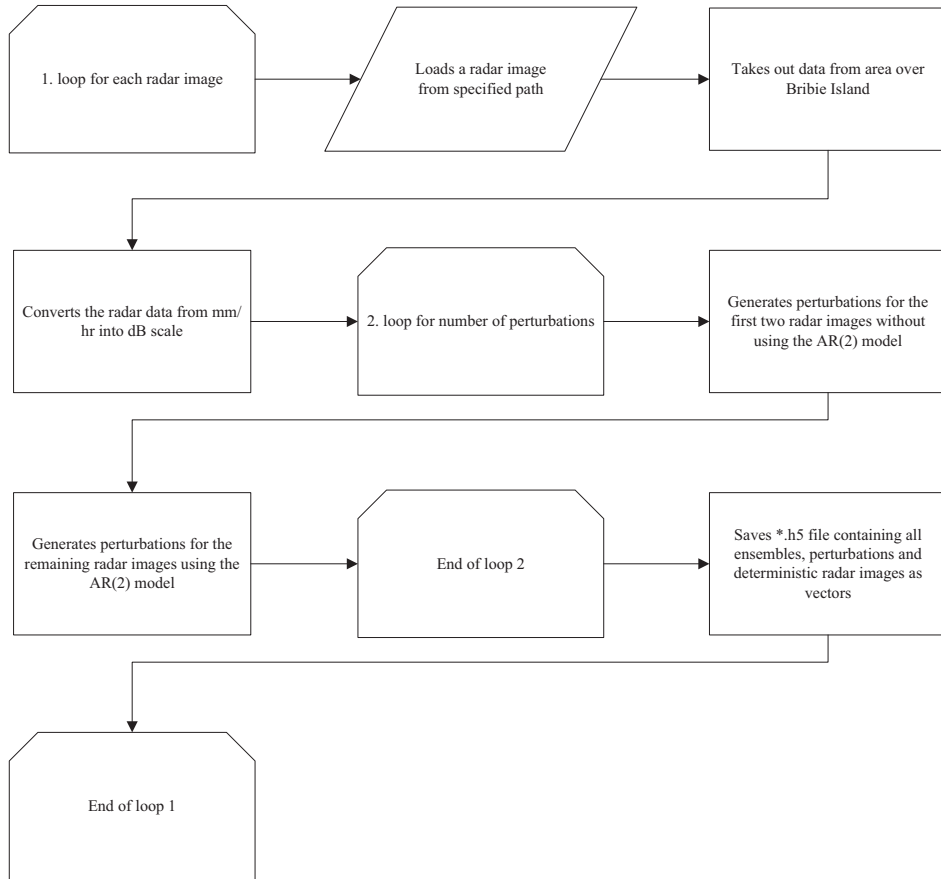


Figure F.4: Flow diagram of function 3 in EG script.

### TS generator

In figure F.5 the flow diagram for the program that generates the time series from the perturbations can be seen.

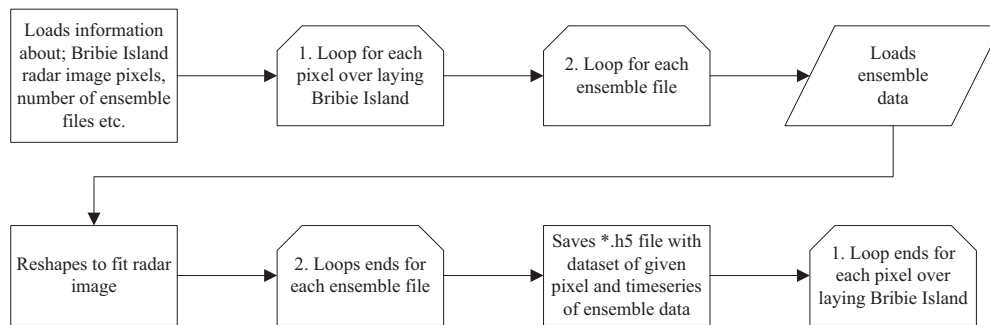
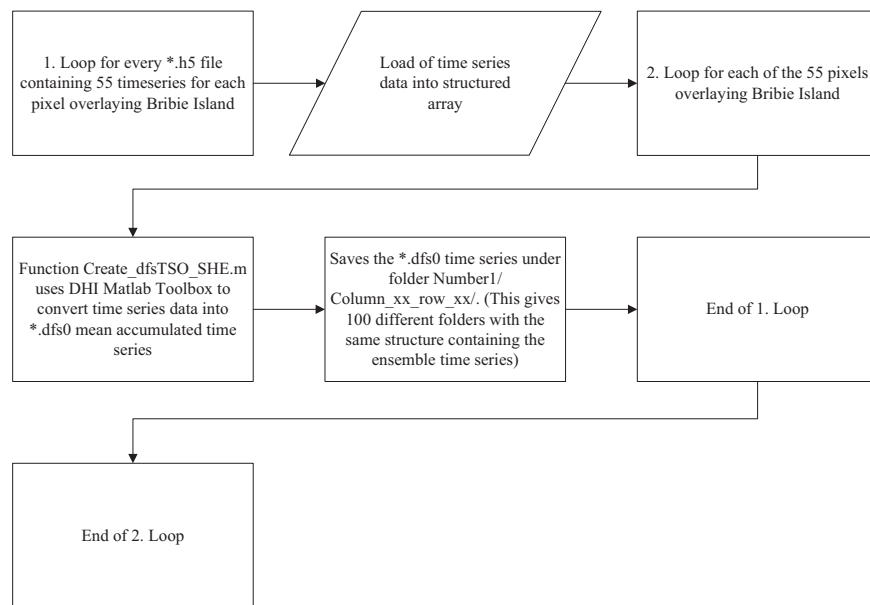


Figure F.5: Flow diagram of Time\_series\_Ensembles.m.

# Batch script for Mike SHE groundwater model

The following shows the flow diagram of converting the ensemble time series from \*.h5 file format into \*.dfs0, see figure G.1, and the flow diagram of the batch script calling the Mike SHE groundwater model, see figure G.2.



*Figure G.1: Flow diagram for program Create\_dfsTSO\_SHE.m.*

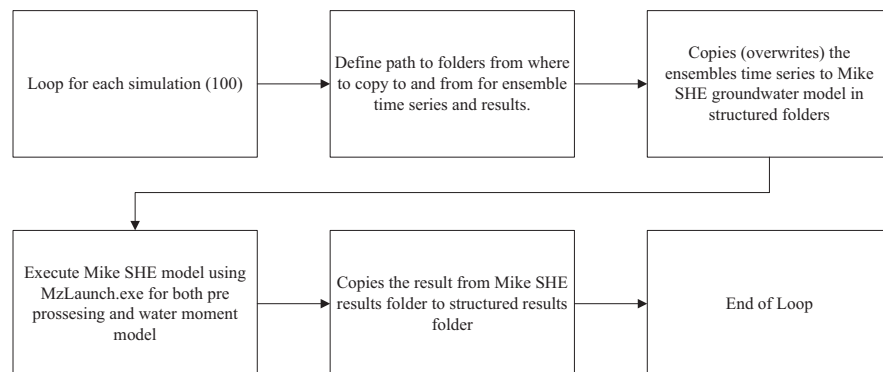


*Figure G.2: Flow diagram for program Execute\_SHE\_Copy.*